EXCITONS AT HIGH DENSITY IN CUPROUS OXIDE AND COUPLED QUANTUM WELLS

by

Yingmei Liu

B. S., JiLin University, 1996

M. S., JiLin University, 1999

M. S., University of Pittsburgh, 2000

Submitted to the Graduate Faculty of

the Faculty and college of Arts and Sciences in partial fulfillment

of the requirements for the degree of

Doctor of Philosophy

University of Pittsburgh

2004

UNIVERSITY OF PITTSBURGH

FACULTY AND COLLEGE OF ARTS AND SCIENCES

This dissertation was presented

by

Yingmei Liu

It was defended on

July 22th 2004

and approved by

David W. Snoke, Department of Physics and Astronomy

Daniel Boyanovsky, Department of Physics and Astronomy

Robert P. Devaty, Department of Physics and Astronomy

Gilbert Walker, Department of Chemistry

Xiao-lun Wu, Department of Physics and Astronomy

Dissertation Director: David W. Snoke, Department of Physics and Astronomy

Advisor: David Wayne Snoke

EXCITONS AT HIGH DENSITY IN CUPROUS OXIDE AND COUPLED QUANTUM WELLS

Yingmei Liu, PhD

University of Pittsburgh, 2004

There is a 40-year long history in the search for Bose-Einstein condensation (BEC) of excitons in semiconductors. This thesis presents research directed toward this goal in bulk crystal Cu_2O in three dimensions and in GaAs-based coupled quantum wells (CQW) in two dimensions.

The Auger recombination process in Cu_2O plays a major role in limiting the density of the excitons. We find that the rate for this process increases with applied stress and lattice temperature. We create paraexcitons in Cu_2O through a resonant two-photon excitation in a harmonic potential trap with the Auger recombination process as small as possible (at low temperature and low stress), and find that the exciton creation efficiency in the resonant two-photon excitation is greater for one-beam excitation than for two colliding pulses, but the colliding pulse method may be useful for direct creation of a condensate in the ground state. The paraexciton density in this work is about thirty times less than the required density for BEC of paraexcitons. One promising direction for BEC of excitons in Cu_2O is that with higher laser power from stronger IR laser sources, or at lower temperature, the critical density can be approached under one-beam two-photon excitation resonant with the paraexciton state.

In two dimensions, the CQW structure has been modified with four design strategies: highest possible barriers, introducing into the barriers a superlattice of 60 ÅGaAs wells, p-i-n doping, and wider quantum wells, which provides indirect excitons low disorder and high mobility. With a cold near-resonant excitation, we conclude that the excitons act as

a free gas, travelling distances of hundreds of microns. We also present observations of a narrow beam of emitted light, when the indirect excitons are confined in a two-dimensional harmonic potential trap, in a way quite similar to the first observations of BEC in alkali atoms. A beam-like emission has been suggested as a telltale for BEC of excitons. This opens the door to a whole range of investigations, including attempts to observe coherence of the emitted light, proof of superfluidity of the excitons, and other fascinating effects.

TABLE OF CONTENTS

LIST OF TABLES

LIST OF FIGURES

PREFACE

I would like to give my deepest gratitude to my Ph.D. research advisor, Prof. David W. Snoke, for his guidance and support during my graduate study. His optimism and unbounded enthusiasm in doing research greatly motivated me at some hard times when the experiments didn't seem to go well.

All my colleagues, Sava Denev, Viorel Negoita, Zoltan Voros, Ryan Balili, Vincent Hartwell and Rene Hurka, helped me a lot in many research challenges and made my Ph.D. study joyful. I appreciate Dr. Loren Pfeiffer and Ken West for the high quality coupled quantum well sample produced by molecular beam epitaxy in Bell labs of Lucent Technologies. I thank Profs. Daniel Boyanovsky, Robert P. Devaty, Gilbert Walker, Xiao-lun Wu and Albert Heberle for many insightful discussions. I wish to thank P. J. Dunn of the Smithsonian Institute for the high quality Cu_2O sample.

I greatly appreciate my husband and my parents. Their everyday moral support and encouragement has been essential.

This work has been supported by CRDF-MRDA Award No. MP2-3026 and NSF Award No. DMR-0102457, and one-year support from University of Pittsburgh through Andrew-Mellon pre-doctoral fellowship.

1.0 INTRODUCTION

There are seven chapters and one appendix in this thesis. This chapter gives a short introduction to excitons, BEC of excitons in two systems, Cu_2O in three dimensions and the coupled quantum well structure in two dimensions. Chapter 2 explains all experimental techniques used in this work. Chapter 3 lists selection rules in Cu_2O derived using group theory, and Chapter 4 explains our experimental and theoretical results about the exciton relaxation processes, which are important for the search for BEC of excitons in Cu_2O. Chapter 5 discusses our promising search for BEC of excitons in Cu_2O under resonant two-photon excitations. Chapter 6 presents evidence that we have observed BEC of excitons in the two-dimensional harmonic potential trap in the coupled quantum well structure. Chapter 7 gives conclusions and some possible directions for future study. The derivation of the electric quadrupole operator is listed in Appendix.

1.1 EXCITONS

An exciton, a fundamental quantum of excitation in solids, is a positively-charged hole and a negatively-charged electron bound together by Coulomb attraction. Excitons are classified into two types: "Frenkel" excitons with a stronger Coulomb attraction and "Wannier-Mott" excitons with a weaker Coulomb attraction. Frenkel excitons are most commonly found in molecular crystals, polymers, and biological molecules. Wannier-Mott excitons, found in most semiconductors, are the main subject of my research.

The Wannier-Mott exciton can be easily understood with a hydrogen-like model, because "the underlying lattice of atoms is treated as a background field in which the electrons and

the holes exist as free particles, and an exciton consists of an electron and a hole orbiting each other in this medium" [1.1]. That is to say, in the hydrogen-like model of the Wannier exciton, the entire effect of the underlying lattice is represented by two parameters, m_r and ϵ_r, the exciton reduced mass and the relative dielectric permittivity of the solid, respectively. Therefore,

$$E_n = \frac{R_{ex}}{n^2} + \frac{\hbar^2 k^2}{2(m_e + m_h)} \quad \text{(n = 1, 2, 3...)} \tag{1.1}$$

$$R_{ex} = \frac{-e^2}{4\pi\epsilon_r\epsilon_0 a} \quad , \tag{1.2}$$

$$a = \frac{\hbar^2\epsilon_r\epsilon_0}{e^2 m_r} \quad , \tag{1.3}$$

$$m_r = \frac{1}{1/m_e + 1/m_h} \quad . \tag{1.4}$$

where E_n is the excitonic energy level, R_{ex} is the excitonic Rydberg, a is the exciton Bohr radius, ϵ_0 is permittivity of free space, $\mathbf{k}$ is exciton wave vector and $m_{e,h}$ is the mass of an electron or a hole.

The Wannier-Mott exciton is a real particle with a typical life-cycle which can be described as follows: (1) The exciton is created by any external sources that can excite electrons and holes, such as absorbing a photon, applying an electric field, etc. (2) The exciton, carrying not mass or charge but energy and momentum, moves through the crystal freely until it scatters with another particle or impurity. (3) The exciton decays in different ways, for example, the electron and hole recombine, emitting a photon. So the exciton will have a finite lifetime. For our Cu_2O and the coupled quantum well structures, the lifetimes range from a few nanoseconds to microseconds depending on the quality of the samples and the amount of the applied stress and the applied electric field, which will be explained in detail in Chapters 4, 5 and 6.

Exciton physics has many interesting applications. For example, because the exciton can have a very short wavelength of tens of angstroms, it can pass through a very small aperture without any diffraction, which can be applied into the modern communication. Moreover, because excitons will act as bosons as long as the inter-particle spacing is larger than the correlation length [1.1], another important effect of excitons is Bose-Einstein Condensation (BEC) of excitons.

1.2 BOSE-EINSTEIN CONDENSATION OF EXCITONS

As Einstein predicted in 1925, in thermodynamic equilibrium, when the density of bosons is above a critical density, the extra particles must all "condense" into the ground state and Bose-Einstein condensation (BEC) occurs. Expressions of the critical density under different conditions, in three dimensions, in two dimensions and in a harmonic potential trap, are derived in this section.

1.2.1 The critical density for an ideal gas of bosons in three dimensions

For an ideal Bose gas at a certain temperature T, f_k, the occupation number of the state with wave vector $\mathbf{k}$, is given by the Bose-Einstein statistics [1.1, 1.2],

$$f_k = f(E) = \frac{1}{e^{(E-\mu)/k_BT} - 1}, \quad \text{and} \quad \sum_k f_k = N. \tag{1.5}$$

where $E = \hbar^2 k^2/2m$ is the kinetic energy of a boson, m is the effective mass of the boson and μ is the chemical potential, and N is the total number of bosons.

Because the density of states has the form $D(E) \sim E^{\frac{d}{2}-1}$ in d dimensions, for a macroscopic volume V in three dimensions, $D(E)$ and n, the density of states and the density of bosons can be expressed as,

$$D(E) = \frac{g \cdot V}{4\pi^2}(\frac{2m}{\hbar^2})^{3/2} E^{\frac{3}{2}-1} = \frac{g \cdot V}{4\pi^2}(\frac{2m}{\hbar^2})^{3/2} E^{1/2}, \tag{1.6}$$

$$N = \int_0^\infty N(E)dE = \int_0^\infty D(E)f(E)dE \quad , \tag{1.7}$$

$$n = \lim_{V\to\infty} \frac{N}{V} = \frac{g}{4\pi^2}(\frac{2m}{\hbar^2})^{3/2} \int_0^\infty \frac{E^{1/2}}{e^{(E-\mu)/k_BT} - 1} dE \quad , \tag{1.8}$$

$$\text{and} \quad n = n(\mathbf{k} = 0) + n(\mathbf{k} \neq 0) = n_0 + n_c. \tag{1.9}$$

where g is the spin degeneracy of the bosons and n_c is the BEC critical density of an ideal Bose gas at a given temperature T. Because zero is the upper bound of μ, the chemical potential, for the distribution function to remain defined at all energies, the BEC critical density is calculated at $\mu = 0$,

$$\Rightarrow \quad n_c^{3D-free-gas} = 2.612g(\frac{mk_BT}{2\pi\hbar^2})^{\frac{3}{2}}. \tag{1.10}$$

However, because most of our experiments confine excitons in a potential well of the form $V(\mathbf{r}) = \frac{1}{2}kr^2$, where r is the distance from the center of the well and k is a constant, it is important to derive the expression of the critical density of bosons in the potential trap. In a 3D harmonic trap, the total number of bosons is N,

$$N = \sum_{n_x,n_y,n_z=0}^{\infty} \frac{1}{e^{(\hbar\omega(n_x+n_y+n_z+\frac{3}{2})-\mu)/k_BT}-1} = \sum_{n=0}^{\infty} \frac{(n+1)(n+2)/2}{e^{(\hbar\omega(n+\frac{3}{2})-\mu)/k_BT}-1} \tag{1.11}$$

$$\text{where,} \quad n = n_x + n_y + n_z (n = 0, 1, ...) \quad \text{and} \quad \omega = \sqrt{\frac{k}{m}} \tag{1.12}$$

In the Stringari-Pitavskii limit [1.3], $\omega \to \infty$ and N$\to \infty$, therefore,

$$N = (\frac{k_BT}{\hbar\omega})^3 \frac{1}{2} g \int_0^{\infty} \frac{t^2}{e^{t-\mu/k_BT}-1} dt, \quad \text{where,} \quad t = \hbar\omega(n+\frac{3}{2})/k_BT \tag{1.13}$$

Again, the critical condition for BEC of bosons in the harmonic potential well is calculated at zero chemical potential, $\mu = 0$,

$$\Rightarrow \quad N_c^{3D-well} \quad = \quad 1.202g(\frac{k_BT}{\hbar\sqrt{k/m}})^3. \tag{1.14}$$

The effective spring constant k for our Cu_2O sample is 65 eV/cm^2 fit from Figure 7.

1.2.2 The critical density for an ideal gas of bosons in two dimensions

In two dimensions, because the density of states is independent of the kinetic energy of bosons, $D(E) \sim E^{\frac{d}{2}-1} = E^{\frac{2}{2}-1}$ =Constant, the integral (1.8) diverges and BEC can't occur. However, there is a Kosterlitz-Thouless phase transition since "superfluidity can occur without Bose-Einstein condensation" [1.4]. On the other hand, when bosons are confined in a harmonic potential well, BEC can appear in two dimensions with a critical total number $N_c^{2D-well}$, which is calculated in the similar way to the three dimensional system. The total number of bosons is N,

$$N = \sum_{n_x,n_y=0}^{\infty} \frac{1}{e^{(\hbar\omega(n_x+n_y+1)-\mu)/k_BT}-1} = \sum_{n=0}^{\infty} \frac{n+1}{e^{(\hbar\omega(n+1)-\mu)/k_BT}-1} \tag{1.15}$$

$$\text{where,} \quad n = n_x + n_y (n = 0, 1, ...) \quad \text{and} \quad \omega = \sqrt{\frac{k}{m}}.$$

In the Stringari-Pitavskii limit [1.3, 1.5], $\omega \to \infty$ and N$\to \infty$, therefore,

$$N = (\frac{k_B T}{\hbar\omega})^2 g \int_0^\infty \frac{t}{e^{t-\mu/k_B T}-1} dt, \quad \text{where,} \quad t = \hbar\omega(n+1)/k_B T \tag{1.16}$$

when $\mu = 0$,

$$\Rightarrow N_c^{2D-well} \quad = \quad 1.645 g(\frac{k_B T}{\hbar\sqrt{k/m}})^2. \tag{1.17}$$

For our experiments in Chapter 6, the effective spring constant k is equal to 31 eV/cm^2, which is fit from a CCD image of the harmonic potential trap.

1.2.3 Spatial condensation in a harmonic potential trap

In the condensate state, the density distribution is $n^c(\mathbf{r}) = N|\phi_0(\mathbf{r})|^2$ [1.3], where $\phi_0(\mathbf{r})$ is the ground state wave-function of N noninteracting bosons confined in the harmonic potential trap. Because $n_x = n_y = n_z = 0$ in the ground state, $\phi_0(\mathbf{r})$ is expressed as [1.3],

$$\phi_0(\vec{r}) = (\frac{m\omega}{\pi\hbar})^{3/4} e^{\frac{-m}{2\hbar}\omega\cdot\mathbf{r}^2}, \quad \Rightarrow \quad n^c(\mathbf{r}) = n^c(0) e^{-\frac{m\omega}{\hbar}r^2}. \tag{1.18}$$

That is to say, the spatial distribution of the density for the condensate state has a Gaussian profile with a width A^c,

$$A^c = \sqrt{\frac{\hbar}{m\omega}}. \tag{1.19}$$

In the low density limit, the non-condensate state has an internal chemical potential,

$$\mu_{int}^{non-c} = -k_B T \ln(n_Q/n), \quad \text{where} \quad n_Q = g(\frac{m k_B T}{2\pi\hbar^2})^{3/2}. \tag{1.20}$$

In the trap, the total chemical potential, the sum of internal and external chemical potentials, is a constant in equilibrium, $\mu = \mu_{int} + \mu_{ext}$ =constant, where μ_{ext} is equal to $\frac{1}{2}kr^2$ for the harmonic potential trap. The spatial distribution of the density for the non-condensate state can be expressed as [1.1],

$$n^{non-c}(\mathbf{r}) = n^{non-c}(0) e^{-\frac{1}{2}kr^2/k_B T}, \tag{1.21}$$

so the density profile for the non-condensate state is still a Gaussian shape but with a different width A^{non-c},

$$A^{non-c} = \sqrt{\frac{2k_B T}{k}} = A^c \sqrt{\frac{k_B T}{\hbar\omega}}. \tag{1.22}$$

Trauernicht [1.6] pointed out that the spatial distribution of the non-condensate particles in a condensed Bose gas is not very different from this Gaussian distribution.

In our experimental conditions, $k_B T \gg \hbar\omega$, therefore,

$$\Rightarrow A^{non-c} \gg A^{c}. \tag{1.23}$$

which indicates that the spatial profile of the density has a sharp peak in the central region for the condensate state. Therefore, BEC in the harmonic potential well corresponds to a spatial condensation.

On the other hand, for the weakly interacting boson gas, the density profile of the condensate is different. When a significant fraction of the excitons condense into the ground state, $\frac{N}{V}a^3$ approaches 1, where N excitons are condensed, the size of each exciton is in the order of the Bohr radius a, and V is the volume of the ground state Gaussian for the non-interacting boson gas, $V = \frac{\pi}{6}(A^c)^3 = \frac{\pi}{6}(\sqrt{\frac{\hbar}{\sqrt{mk}}})^3$. However, for the excitons to remain individual bosons, the condition $\frac{N}{V}a^3 \ll 1$ must be satisfied [1.1], therefore the condensate wave-function must get larger, because all the available space is filled. The maximum number of excitons which can occupy the ground state is $N_{max} \ll \frac{V}{a^3} \approx 10^8$ for our experiments in Cu_2O, while the critical number of BEC in the 3D trap is equal to $2.5 * 10^8$ at 2 Kelvin from Eq. (1.14), which is comparable to this limit. In this case, we have to take into account the effect of interactions among the particles. In the limit of weak interaction, when the condensate density is much greater than the non-condensate density near the center of the well, the internal chemical potential is [1.7],

$$\mu_{int}^{cwi} = n * U_{ex-ex}, \quad \text{where} \quad U_{ex-ex} = \frac{\hbar^2}{\pi m}a. \tag{1.24}$$

a in the above equation is the scattering length, which is in the order of 1 Å. The superscript "cwi" stands for the condensate with weak interaction, and index "ex-ex" means the exciton-exciton interaction. Again, because the total chemical potential is a constant, the spatial distribution of the density for the condensate state is,

$$n(\mathbf{r})^{cwi} = \frac{\mu - \frac{1}{2}kr^2}{U_{ex-ex}} \sim (constant - \frac{k}{2U_{ex-ex}}r^2). \tag{1.25}$$

If the interaction is very weak, $\frac{k}{2U_{ex-ex}}$ is very big, and therefore the density spatial distribution for the weak-interacting condensate, $(constant - \frac{k}{2U_{ex-ex}}r^2)$, is much narrower than the wide Gaussian profile for the non-condensate state. In other words, there is still an appearance of a sharp central peak in the spatial distribution of the density when the condensation occurs in the trap.

However, when the interaction is strong for the interacting gas at high density, $\frac{k}{2U_{ex-ex}}$ is very small, and the condensate spatial size can in principle be comparable to the non-condensate part for high enough density. Therefore, there will not be a spatial condensate, but an angular peak [1.8], because of an uncertainty relation between spatial coherence size and momentum space (k-space) coherence size, which will be explored in Chapter 6.

In short, only for the weakly interacting and non-interacting boson gas, the spatial condensate is a clear telltale for BEC in the harmonic potential trap. While for the interacting gas at high density, BEC in the trap corresponds to not the spatial condensation but the k-space condensation.

1.2.4 BEC of excitons

BEC can occur in different systems, such as liquid helium, alkali atoms, superconductors, and excitons in semiconductors. The critical density and critical temperature in each system are calculated from equations (1.11) and (1.14), as listed in Table 1.

System	Effective mass	Critical density	Cirtical temperature
Helium-4	$4m_p$	$10^{22}cm^{-3}$	2 Kelvin
Alkali atoms	$100m_p$	$10^{18}cm^{-3}$	0.0000001 Kelvin
Exciton	$2m_e$	$10^{17}cm^{-3}$	tens of Kelvin to room temperature

Table 1: The critical particle density and critical temperature for three different systems in Bose-Einstein condensation.

The discoveries of superfluidity in Helium-4 in 1938 and of BEC in alkali atoms in 1995 have been major advances and awarded with two Nobel prizes in Physics [1.9, 1.10, 1.11]. However, the critical temperature of BEC in alkali atoms is as low as 100 nanokelvin which

leads to a lot of experimental challenges, while BEC of excitons can occur in a standard cryostat which is one of our biggest motivations, because the critical temperature for BEC is inversely proportional to $(m_{eff})^{\frac{3}{2}}$ in three dimensions at a fixed critical density and the effective mass of an exciton is much less than that of an alkali atom.

Two essential requirements for BEC of excitons are that the exciton must have a lifetime which is longer than the exciton thermalization time of hundreds of picoseconds, and that the excitons have overall repulsive interactions, so that a fermionic electron-hole liquid (EHL) state does not occur [1.1]. Our searches for BEC of excitons have been focused on two good systems, paraexcitons of Cu_2O in three dimensions and indirect excitons of coupled quantum wells in two dimensions. One advantage of the two-dimensional system is that the required critical density for the condensation of excitons at a given temperature in a 2-D trap is lower than that in a 3-D trap, as shown in equations (1.14) and (1.17).

1.3 EXCITONS IN A THREE-DIMENSIONAL SYSTEM - CUPROUS OXIDE

1.3.1 Band structure in Cu_2O

Naturally-grown high-quality Cu_2O is a good candidate for studying excitonic Bose-Einstein condensation, because an inversion symmetry in Cu_2O forbids any direct dipole recombination of excitons, which gives the exciton a long lifetime up to microseconds; because Cu_2O is a direct-gap semiconductor with repulsive exciton-exciton interactions, which means the EHL is not stable [1.1]; and because the large binding energy of the excitons (150 meV) is equivalent to a temperature of 1740 Kelvin, which allows excitons to exist at room temperature [1.12].

An unstressed Cu_2O crystal is described by the O_h symmetry point group, in which the 4s-oxygen-orbital forms a ${}^1\Gamma_1^+$ level of the conduction band and the 3d-copper-orbital forms ${}^3\Gamma_5^+$ and ${}^2\Gamma_3^+$ levels of the valence band. Multiplying by the ${}^2\Gamma_6^+$ spin, in the unstressed Cu_2O crystal, the conduction band level is ${}^2\Gamma_6^+$, because ${}^1\Gamma_1^+ \otimes {}^2\Gamma_6^+ = {}^2\Gamma_6^+$. The highest levels of the valence band are Γ_7^+ and Γ_8^+, because ${}^2\Gamma_3^+ \otimes {}^2\Gamma_6^+ = {}^4\Gamma_8^+$ and ${}^3\Gamma_5^+ \otimes {}^2\Gamma_6^+ = {}^2\Gamma_7^+ \oplus {}^4\Gamma_8^+$.

As shown in Fig. 1 [1.13], there are several series of excitons, "yellow" excitons consisting

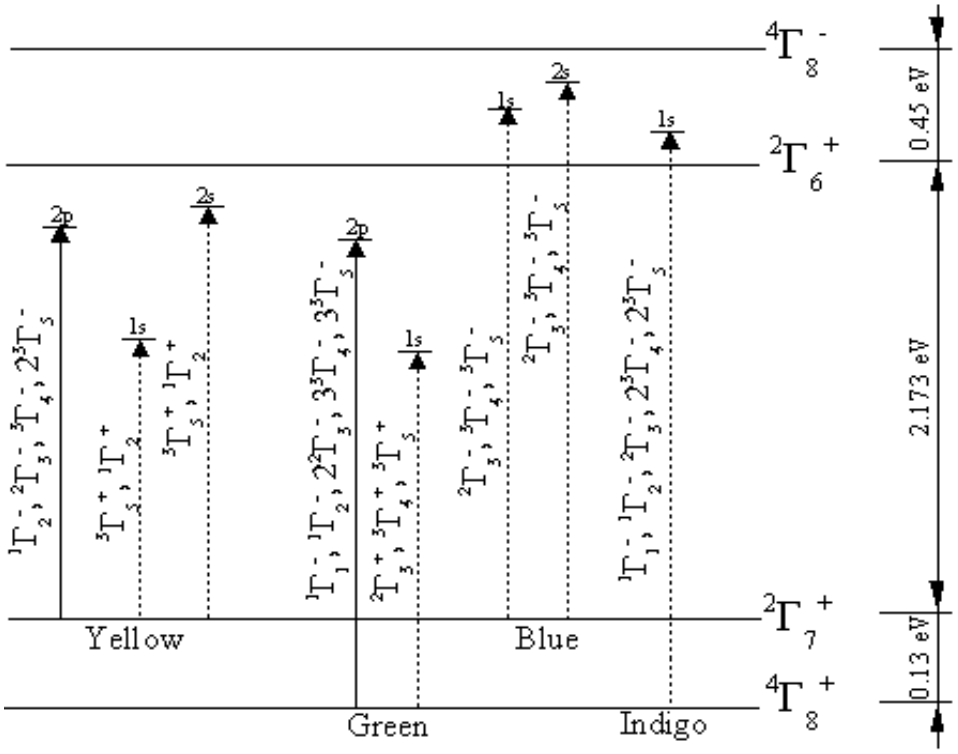

Figure 1: Cu_2O band structure.

of electrons in the Γ_6^+ level of the conduction band and holes in the Γ_7^+ level of the valence band with 2.173 eV gap energy, "green" excitons consisting of electrons in the Γ_6^+ level of the conduction band and holes in the Γ_8^+ level of the valence band with 2.3 eV, and "blue" and "violet" excitons consisting of electrons in the upper conduction bands with higher gap energy. Our interest is in the lowest excitonic states, "yellow" excitons, which can be expressed as the following [1.14],

$$E_n^{Yellow-exciton} = (2.173 - \frac{R^*}{n^2}) \quad eV. \tag{1.26}$$

where, R^*, the effective Rydberg constant for the yellow series excitons, is independent of "n". "n" is any integer between 1 and 12.

By electron-hole exchange, the 1s - "yellow" excitons will split into the spin-triplet orthoexciton and the spin-singlet paraexciton, which lies 12 meV lower in an unstressed crystal,

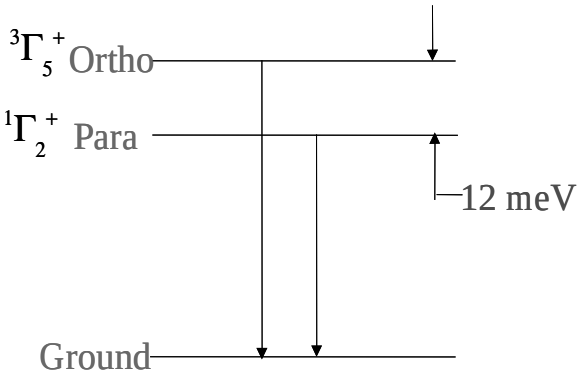

Figure 2: Schematic of 1s "yellow" exciton states in Cu_2O.

as shown in Figure 2. In Cu_2O, there are two possible single-photon transitions, a direct transition by emitting a photon, which is allowed only when the linear momentum of the exciton is negligible, and a phonon-assisted transition by emitting a photon and a phonon, in which the photon takes most the energy and the phonon takes almost all the linear momentum and a fixed energy. Energies of zone-center optical phonons and the relative radiative efficiency of the corresponding phonon-assisted luminescence process are listed in Table 2 [1.1]. Because the indirect transition is allowed for all exciton states, the indirect phonon-assisted luminescence spectrum will give an accurate replica of the energy distribution of the excitons [1.15]. This process is only weakly allowed for the paraexcitons, however.

1.3.2 Reported signatures of BEC of excitons in Cu_2O

In the past decades, there have been a few reports on signatures of Bose condensation of 1s-"yellow" excitons in Cu_2O at high exciton densities:

1. A direct evidence of the condensation of excitons in Cu_2O is Bose narrowing in phonon-assisted luminescence of excitons, because the phonon-assisted luminescence gives the exciton kinetic energy distribution function which should exhibit a δ-like spectral peak near the condensation from Bose statistics. Two famous reports of the spectral narrowing are: "an extremely narrow energy distribution ($\Delta E \ll k_B T$) of paraexcitons in the ground state observed under conditions of $n > n_c$" under a single-photon excitation in a lightly

Phonon	Energy	Relative Radiative Efficiency	
		Orthoexciton	Paraexciton
$^3\Gamma_{25}^-$	11.0 meV	17	1
$^2\Gamma_{12}^-$	13.8 meV	500	≈0
$^3\Gamma_{15}^-$	18.7 meV	17	≈0
$^1\Gamma_2^-$	43 meV	3	
$^3\Gamma_{25}^+$	64 meV	3	
$^3\Gamma_{15}^-$	79 meV	8	

Table 2: Zone-center optical phonons in Cu_2O [1.1].

stressed Cu_2O by Lin and Wolfe [1.16], and a report from Goto and Shen under a two-photon excitation which reports the δ-peak with a width equal to the experimental spectral resolution and "The δ-peak persists to late times after the laser excitation has ceased and persists longer when the excitation density is higher" [1.17, 1.18].

However, the spectral narrowing alone is not a good signature of the condensation of excitons, because there are other effects that give the spectral narrowing, for example the spectral δ-peak can be mimicked by the region of cold exciton gas, which is possibly true for the above two experiments. In Lin and Wolfe's experiment, one of the reasons for the narrow spectral peak only in the paraexciton luminescence could be that the paraexciton was cooler because of the longer lifetime. And in Goto and Shen's experiment, the exciton was created cold through a resonant two-photon experiment, which could give a narrow spectral peak. Also the spectral δ-peak can be easily lost in spectra taken from spectrometers with finite experimentally spectral resolution, if the condensation fraction is small.

2. Another reported indication of BEC of excitons is quantum saturation, "the effect of exciton gas to remain close to BEC phase boundary over a wide range of exciton densities and temperatures" [1.1], in other words, the fit exciton density closely follows a dependence on temperature T, $n_{fit} = CT_{fit}^{3/2}$. The first reported "quantum saturation" effect of orthoexcitons was obtained by Snoke *et at.* [1.20] from a high density surface excitation which gave a highly non-equilibrium exciton gas. Lin and Wolfe [1.16] made an improvement by using

stress to lift the orthoexciton degeneracy, which not only reproduced quantum saturation of excitons, but also convinced them that BEC of paraexcitons occurred, since the fit paraexciton density exceeded the BEC critical density under certain conditions. However, exciton densities in the two experiments were not from a direct measurement but fit from the spectra of the exciton photoluminescence. K. O'Hara *et al.* [1.21] addressed this problem and introduced a direct measurement of exciton density by calibrating a relationship between the number of excitons and the photon count rate after taking into account the efficiency of the whole image collecting and analyzing system, which gave a surprisingly inconsistent result: under the same condition as that in Lin and Wolfe's experiment, the re-calibrated paraexciton density is only about 1 % of the critical density for BEC.

Although the inconsistency seriously shakes Lin and Wolfe's claim of the condensation of paraexcitons, quantum saturation itself, or in other words, fit of the spectra to a Bose degenerate line shape over a wide range of the exciton densities and temperatures, still requires explanation. O'Hara and Wolfe [1.21] provided a possible explanation in terms of non-equilibrium kinetic rate equations, but there are many uncertain parameters in this theory, and the fits to the data were not outstanding. Moreover, the density estimate from O'Hara could be off by an order of magnitude, because it involves too many parameters which give a big error, such as the reflection of optical components, liquid Helium, the quantum efficiency of photomultiplier and discriminators, and so on. I will give our thinking on the calibration of exciton density in Chapter 4.

3. Because in principle, excitonic condensates should be superfluid, "i.e. decoupled from the phonon field of the crystal, and therefore may move ballistically" [1.19], a fast expansion of excitons was treated as a signature of the condensation. Mysyrowicz, Snoke and Wolfe [1.22] first reported the observation of a fast expansion of excitons over unusually large distances out of the excitation region at low lattice temperature and an initial exciton density close to the critical density for BEC; and later on, by using the photovoltaic detection of excitons, Fortin, Fafard, Benson and Mysyrowicz [1.23, 1.24, 1.25] reported "exciton transport over large distances in Cu_2O as a function of temperature and particle density" and "evidence for a phase transition at low temperature and high density" [1.25], which was attributed to the excitonic superfluidity. However, a detailed investigation from Bulatov and

Tikhodeev [1.26] showed that the speed of the exciton packet was $3.9 \times 10^5 cm/s$ which is comparable to the speed of phonons in Cu_2O, and the fast expansion can be explained with the well-known "phonon wind" mechanism, in which hot phonons created by a high power laser with photon energy above the band gap can "blow" excitons away from the excitation region at the speed of phonons (speed of sound).

Therefore, ballistic expansion of excitons could be a good signature of the condensation if the speed of the exciton is much faster than the speed of phonons, and the transport can not be explained by other effects, for example the pressure among excitons.

4. A low energy tail in the phonon-assisted orthoexciton luminescence line was reported as a signature of BEC of excitons, because the low energy tail persists when the lattice temperature is below the critical temperature T_c for the condensation and disappears once the temperature above T_c, according to the predictions from Haug [1.27] and Shi [1.28]. Theoretically, the low energy tail is a better signature than the δ-function spectral narrowing, because the spectral peak can be lost in the spectrum if the condensation fraction is small. However, there are other reasons besides BEC which can lead to the low energy tail, for example normal collisions of excitons. Therefore, the low energy tail alone is not a signature of Bose condensation of excitons.

In short, up to now, none of the reported signatures of Bose condensation of excitons has been accepted as unambiguous evidence of the condensation, which is one of my motivations in this research. For a claim of Bose condensation of excitons, I believe at least four questions should have positive answers: Is there a critical density of excitons? Does the critical density have the same temperature dependence as predicted by Bose statistics, for example $N_{critical} \sim T^2_{critical}$ in two dimensions and $n_{critical} = CT^{3/2}_{critical}$ in three dimensions? Is there a k-space condensation, or a spatial condensation for weak interacting exciton gas confined in a harmonic trap? Can the coherence of the exciton state be demonstrated, such as through an interference experiment or through the observation of superradiant states?

1.3.3 Controversial processes in Cu_2O

As mentioned above, Cu_2O has attracted lots of attention as a good three-dimensional system for BEC of excitons in the last decades. The interpretation of these experiments has been the

subject of debate, however, because many of the basic relaxation processes of the excitons in Cu_2O have remained unknown.

Two processes in particular have remained controversial. The first is the Auger non-radiative recombination process for excitons. In the Auger process, two excitons collide, and one exciton ionizes, taking the energy of the other exciton which recombined. Some groups believe that the density-dependent Auger process is a barrier for Bose condensation of excitons, since it not only gives a severe limit in exciton density, but also heats up the exciton gas [1.12, 1.29, 1.30, 1.31], while others claim that the process is negligible [1.32]. Trauernicht *et al.* [1.1] first gave strong evidences of an Auger process by trapping the excitons with an external stress, however, theoretical estimates [1.33, 1.34] of the rate for Auger recombination are orders of magnitude different from experimental values [1.35, 1.36].

The second process under debate is the conversion mechanism from orthoexcitons to paraexcitons. The lowest-energy exciton state of Cu_2O is split into a triplet "orthoexciton" state and a singlet "paraexciton" state, with energy splitting 12 meV. Converting from one state to the other requires flipping an electronic spin. Recent theoretical work has argued for a collisional conversion mechanism [1.37, 1.38], while earlier work invoked a phonon emission mechanism [1.39, 1.40].

Therefore, my work on BEC of excitons in Cu_2O has been separated into two steps: First, Chapters 3 and 4 establish a good experimental system for BEC of excitons, after taking a close look at the Auger effect and inter-conversion mechanism between orthoexcitons and paraexcitons which may be big barriers for the condensation at high exciton densities. Then the search for BEC of excitons in the good system is explored in Chapter 5.

1.4 EXCITONS IN A TWO-DIMENSIONAL SYSTEM - COUPLED QUANTUM WELLS

Besides Cu_2O, I also did experiments on GaAs-based coupled quantum wells, which were produced by Dr. Loren Pfeiffer and Ken West using molecular beam epitaxy (MBE) at Bell labs of Lucent Technologies in New Jersey. A schematic of a typical coupled quantum well structure is shown in Fig. 3. When an electric field is applied perpendicular to the wells,

electrons are confined in one well, and holes are confined in the adjacent well. Excitons created from an electron and a hole in different quantum wells are called spatially "indirect" excitons, in contrast to direct excitons comprised of an electron and a hole in the same well, as shown in Fig. 4.

The system of indirect excitons in coupled quantum wells is in many ways an optimal system for observing BEC of excitons. First, the spatial separation of the electron and hole implies that the indirect excitons will have long radiative lifetime up to 10 microsecond, since the recombination rate is proportional to the wave-function overlap of the electron and hole in an exciton. Second, the spatial separation of the electron and hole implies that the indirect excitons will have overall repulsive interaction, as aligned dipoles [1.1]. Moreover, as shown in Fig. 3, the exciton gas in the coupled quantum wells is two-dimensional since there is a quantum confinement in one direction, which means that the necessary number of excitons for BEC of indirect excitons at a given temperature is much lower than that in three-dimensional systems, as shown on Section (1.2).

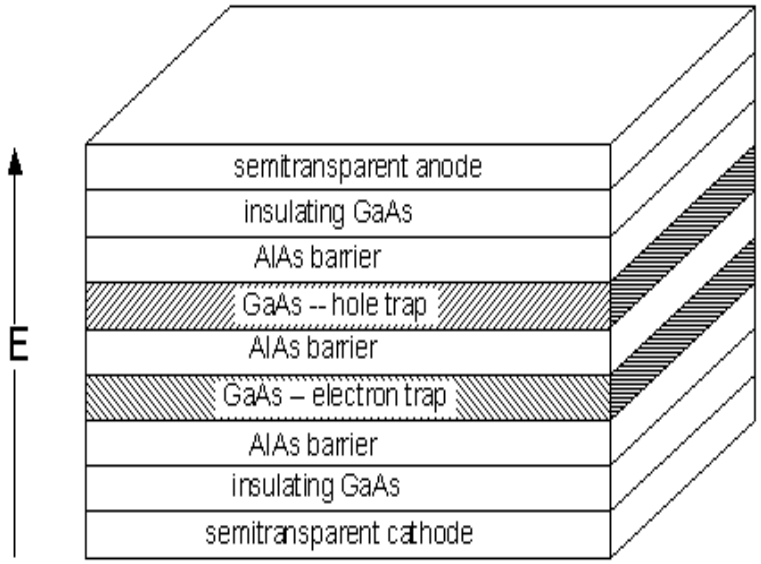

Figure 3: The layered structure of coupled quantum wells produced by MBE.

But the greatest problem with coupled quantum well structures has been the presence of disorder [1.1], which arises during the growth process through a number of mechanisms, such as well width variation, disorder in the alloys used for some of the epitaxial layers, and

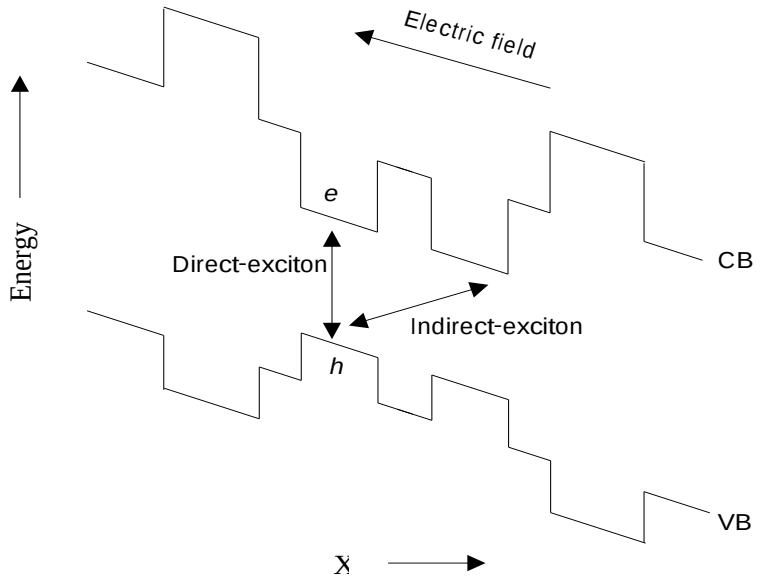

Figure 4: Illustration of the energy bands of the double quantum well structure, in the presence of electric field perpendicular to the wells.

impurities. I will explain problems of disorder and tunnelling of free charge carriers through the barriers in Chapter 6.

In the last few decades, as with the research on Cu_2O discussed in Section (1.3.2), there have been several claims of observation of BEC of indirect excitons [1.42, 1.43, 1.44, 1.45, 1.46]:

1. The earliest claim of BEC of indirect excitons was made by Fukuzawa *et al.* [1.42] based on a signature of "a sharp reduction in the linewidth of the PL spectra, taking place below a critical temperature $T_c \simeq 10K$" [1.42]. Timofeev *et.al* [1.46] made a similar claim based on the observation of the narrowing of the exciton luminescence line at below-critical temperature under a resonant excitation by circularly polarized light. However, as mentioned in the last section, the sharp δ-function spectra peak is not a good signature of the condensation, because a lot of effects besides BEC can give the sharp peak. In this experiment, the possible reason is the localization in random potential fluctuations [1.43]. The other problem pointed out by the authors is that "the temperature for the onset of the linewidth reduction is not very sensitive to power-density variations" [1.42], although theoretically the critical temperature should be proportional to the exciton density in two dimensions.

2. L. V. Butov has made a lot of contributions in this field, among which there are at least two claims of the observation of BEC of excitons. First, in 1994, Butov *et al.* [1.44] reported the appearance of huge broad band noise in the exciton photoluminescence under certain conditions, only at low temperatures, only in the long-lifetime indirect exciton regime, only at high perpendicular magnetic field which increases the exciton binding energy. The huge broad band noise was attributed to the condensation of the indirect excitons, because "The noise amplitude is known to be inversely proportional to the number of statistically independent entities, and therefore large noise amplitudes denote that only a small number of entities exists in the macroscopically large photoexcited region" [1.44]. The huge broad band noise could be related to BEC of excitons. However, the authors didn't explain whether other important signatures of the condensation appeared in their system, for example, the relationship between the critical temperature and the exciton density.

3. The other claim from Butov *et al.* [1.45] was made in 2002 by reporting "fragmentation of the ring-shaped emission pattern into circular structures that form periodic arrays over length up to 1 mm" at low temperature with a non-resonant excitation. The ring structure is due to not BEC but the charge separation [1.47], however, the fragmentation may relate to the condensation. One problem is that the ring fragmentation seems very hard to reproduce, even in the same research group [1.48].

Therefore, none of the claims has been accepted as unambiguous evidence for BEC of the indirect excitons, because all the experiments can be interpreted by other effects besides BEC. Based on the criteria given in Section (1.3.2), our observation of a possible Bose condensation of the indirect excitons in the coupled quantum wells is elaborated in Chapter 6.

2.0 EXPERIMENTAL TECHNIQUES

In this chapter, all the experimental techniques involved in this work, experimental set-up, imaging techniques, time-correlated single photon detection, how to create a harmonic potential trap in two and three dimensions and the operation theory of our home-built OPG-OPA laser source, are presented.

2.1 EXPERIMENTAL SET-UP

In all the experiments, a sample, either Cu_2O or the coupled quantum wells, is immersed in a Janis optical cryostat at a temperature in the range of 1.6 Kelvin to 350 Kelvin controlled by a homemade PID temperature controller with an accuracy of ± 2 Kelvin at high temperatures. The naturally grown Cu_2O sample was obtained from P. J. Dunn of the Smithsonian Institute and polished by me, and the high-quality couple quantum wells were produced by Dr. Loren Pfeiffer and Ken West at Bell labs. As shown in Fig. 5, the sample is illuminated by a laser beam with a specified polarization and the exciton luminescence is collected by an imaging lens which focuses the light onto the entrance slit of the Oriel MS257, a $\frac{1}{4}$-meter imaging spectrometer, with a choice of a CCD camera and a photo-multiplier tube (PMT) as detectors.

Comparing to a conventional spectrometer, the imaging spectrometer has one special feature: preserving spatial information in a direction horizontal to the input slit. That is to say, when the luminescence intensity distribution is transferred from the input slit to the output slit of the spectrometer, the spectral dispersion only occurs along a direction perpendicular to the input slit and the spatial information along the direction horizontal to

the input slit is preserved, as shown in Figure 35. Therefore, the CCD camera connected with the spectrometer gives us both spectral and spatial information of the photoluminescence, and a CCD camera gated by a high voltage pulse provides the spectral, spatial and temporal information of the exciton luminescence with a time resolution of 10 ns [2.1]. However, in

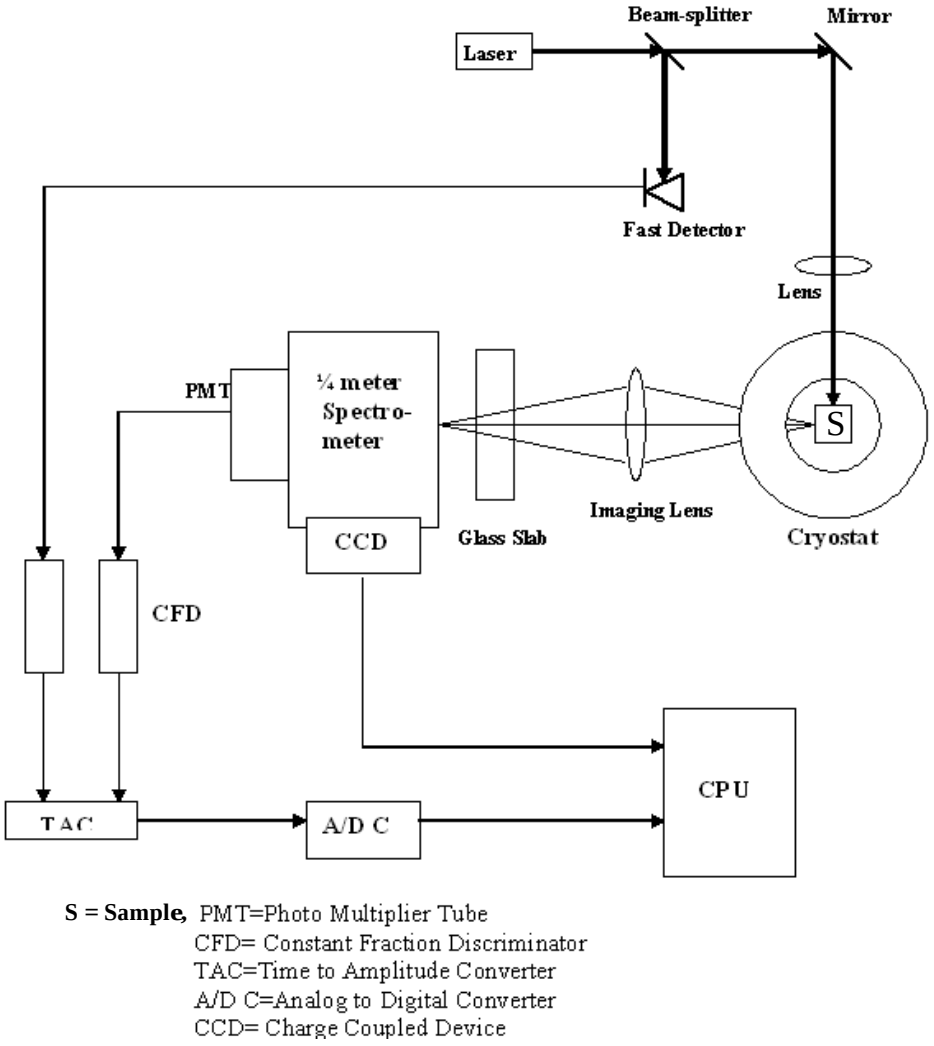

Figure 5: Schematic of the experimental set-up.

most of our experiments the exciton population dynamics are examined by means of time-correlated single photon detection from the combination of photomultiplier (PMT), Time-Amplitude-Converter (TAC) and a computer controlled Multi-channel Analyzer (MCA). The TAC takes the output of the PMT and converts it to an analog voltage pulse which is

proportional to the time elapsed between the trigger signal and the detected photon from the PMT. A histogram of the TAC output pulse heights by the MCA is called a "time trace" and shows the number of photons versus arrival time. Because the number of emitted photons is proportional to the number of excitons for constant radiative recombination rate, a time trace will give us a measurement of the number of excitons versus arrival time. After fitting the time trace with an exponential function, the inverse of the exponential factor will be the lifetime of excitons. We can scan the sample spectrally by rotating a diffraction grating in the spectrometer. By recording a time trace for each wavelength, we get a time resolved spectrum (TRS) from which we can get a two dimensional set of data, the exciton intensity versus the wavelength and arrival time. We can scan the sample spatially by rotating a thick glass slab before the spectrometer. By recording a time trace at each spatial position in the sample, we get a time resolved spatial profile (TRP) from which we can get another two dimensional set of data, the exciton intensity versus the spatial position of the sample and the arrival time[2.2].

2.2 CREATING HARMONIC POTENTIAL TRAPS

As elaborated in Chapters 1 and 3, creating harmonic potential traps is very important in our search for the condensation of excitons. First, Bose-condensation can't occur in two dimensions without harmonic potential traps. Second, there is no way to determine the exact excitation volume and the distribution of the exciton density for an unstressed crystal since the photons of lasers are absorbed near the surface, creating a highly non-equilibrium exciton gas. Moreover, some types of excitons, for example paraexcitons in Cu_2O, can not be observed without the harmonic traps. In this section, I explain how to confine excitons in a harmonic potential trap via a hertzian contact geometry in the three dimensional system and via a sharp pin in the two dimensional system. The created excitons will have a defined volume which is determined by the size of the harmonic potential trap.

2.2.1 Harmonic potential traps in Cu_2O

In the three-dimensional system, Cu_2O, harmonic potential traps are created with a stress by pushing a 6 mm radius curved glass lens down from the top [001] surface of the sample, as shown in Figure 6. Following Trauernicht and Waters *et al.* [2.3], I calculate the energy shift

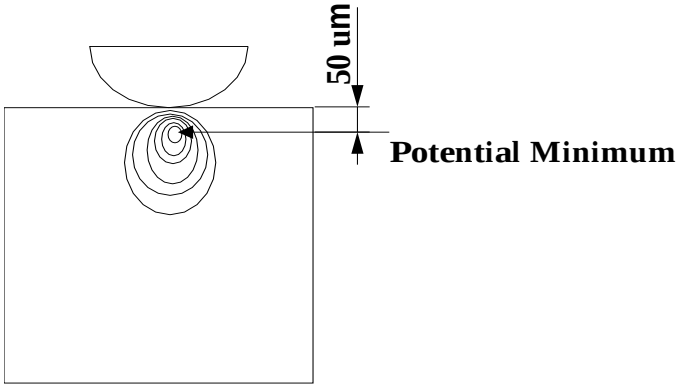

Figure 6: Schematic of creating harmonic potential traps under a stress along the [001] axis in Cu_2O with a 6mm radius curved glass stressor.

of paraexcitons and orthoexcitons, E_p and E_o respectively, as a function of z, the depth of the trap made by the 6 mm radius curved glass stressor from the second-order perturbation theory,

$$E_o(z) = a\ (S_{11}+2S_{12})\ \sigma(z) - \frac{4\ b\ (S_{11}-S_{12})J}{\Delta}\ \tau(z) - \frac{18\ b^2\ (S_{11}-S_{12})^2}{\Delta}\ \tau(z)^2, \quad (2.1)$$

$$E_p(z) = a\ (S_{11}+2S_{12})\ \sigma(z) - \frac{18\ b^2\ (S_{11}-S_{12})^2}{\Delta}\ \tau(z)^2, \quad (2.2)$$

where, σ is the hydrostatic stress which can be expressed as,

$$\sigma(z) = \sigma_{zz}(z) + \sigma_{xx}(z) + \sigma_{yy}(z), \quad (2.3)$$

$$\sigma_{xx}(z) = \sigma_{yy}(z) = q_0[(1+\nu_1)(1 - \frac{z}{r_0}\tan^{-1}(\frac{r_0}{z})) - \frac{1}{2(1+(z/r_0)^2)}], \quad (2.4)$$

$$\sigma_{zz}(z) = \frac{q_0}{1+(z/r_0)^2}; \quad (2.5)$$

and τ is the shear stress,

$$\tau(z) = \sigma_{zz}(z) - \frac{1}{2}\sigma_{xx}(z) - \frac{1}{2}\sigma_{yy}(z), \quad (2.6)$$

In the above equations, r_0 is the radius of the contact area and q_0 is the pressure at the center,

$$r_0 = \left(\frac{3\pi}{4} F R \left(\frac{1-\nu_1^2}{\pi E_1} + \frac{1-\nu_2^2}{\pi E_2}\right)\right)^{\frac{1}{3}}, \tag{2.7}$$

$$q_0 = \frac{3F}{2\pi r_0^2} . \tag{2.8}$$

Fig 7 shows that our theoretical calculation of energy shifts of paraexcitons and orthoexcitons

a, hydrostatic deformation potential	1.7 eV
b, shear deformation potential	0.3 eV
S_{11}, the elastic compliance constant of the Cu_2O sample	4.169×10^{-12} cm^2/dyn
S_{12}, the elastic compliance constant of the glass	-1.936×10^{-12} cm^2/dyn
E_1, the Young's modulus of the Cu_2O sample	12.3×10^{11} cm^2/dyn
E_2, the Young's modulus of the glass	7.17×10^{11} cm^2/dyn
ν_1, the Poisson's ratio of the Cu_2O sample	0.465
ν_2, the Poisson's ratio of the glass	0.16
J, the spin-exchange constant	0.0227 eV
Δ, the spin-orbit splitting of the valence band	0.074 eV
F, the applied force	8×10^5 dyn
R, the radius of the curved glass stressor	0.6 cm

Table 3: Useful parameters in the energy shift calculation of the Cu_2O sample [1.1].

under the stress along [001] axis with the applied force of 8×10^5 dyn is consistent with our experimental results captured with the CCD camera. All the useful parameters for the calculation are listed in Table 3 [1.1].

We found the amount of the applied stress not by a direct measurement of force and contacting area, but by comparing the exciton photoluminescence with Fig 8, a uniaxial stress calibration from Mysyrowicz et al. [2.5]. In our experiment the stress is not uniaxial, but in a small region near the bottom of the trap, however, we can approximate it as an uniaxial stress [2.2].

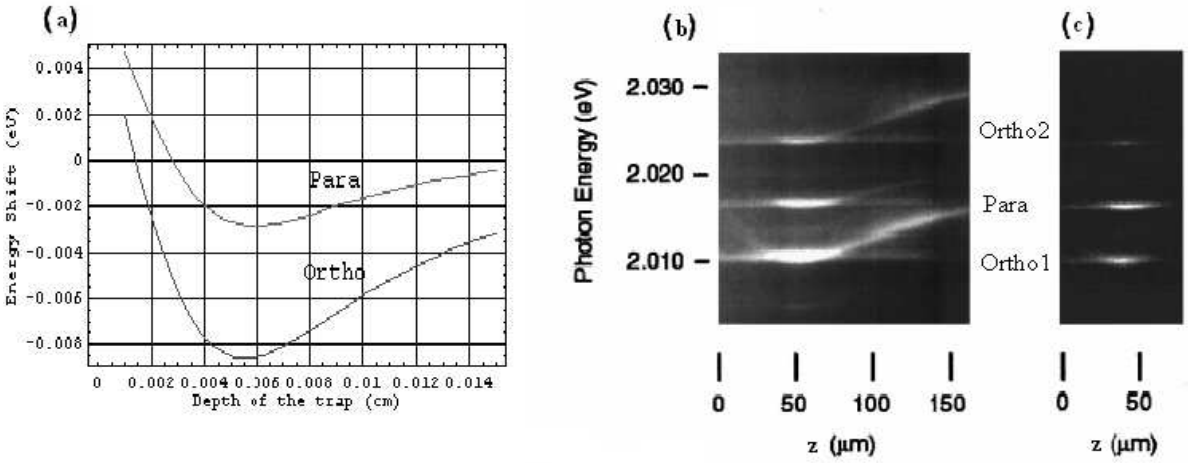

Figure 7: (a): Theoretical results for energy shifts of paraexcitons and orthoexcitons under stress along the [001] axis with the applied force of 8×10^5 dyn from the formula listed in the text. (b): The CCD image of the Cu_2O sample at 2 K under [001] stress with resonant single-photon excitations. Ortho1 and Ortho2 in the figure are phonon-assisted orthoexciton luminescence and direct orthoexciton luminescence, respectively. (c): Same as Right (b), except the laser is set at the potential minimum.

2.2.2 Harmonic potential traps in the coupled quantum wells

Excitons in the coupled quantum wells are confined by pushing a sharp pin from the top surface of the sample, which enables a transition from a two dimensional, translationally invariant system to a confined system by removing or applying the external stress. When an in-homogenous stress applied to the sample, there are two different deformation potentials, the hydrostatic deformation potential which changes the energy, and the shear deformation potential which affects not the energy but the symmetry of the sample. For the free-standing geometry, an external force via the pin leads to a hydrostatic expansion that lowers the energy of the indirect exciton, which has been confirmed both theoretically and experimentally as shown in Figure 9 [2.2]. For a bottom constrained geometry, there is a hydrostatic compression that gives the indirect exciton a blue-shift in energy, which prevents formation of a trap. Therefore, as shown in Figure 10, we choose a free-standing geometry for the 2D coupled quantum wells in all of the experiments.

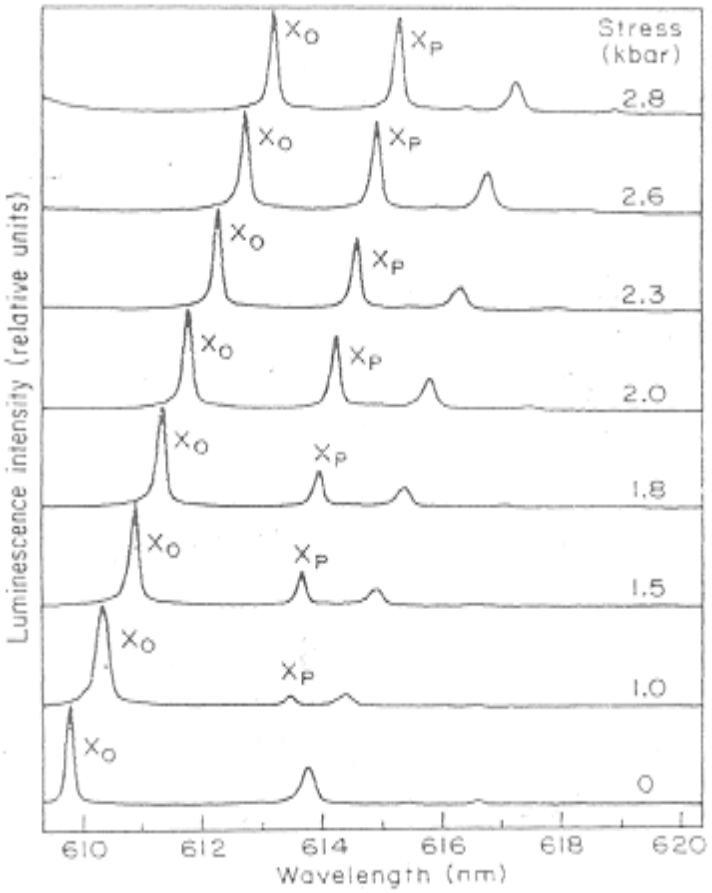

Figure 8: The exciton luminescence spectra as a function of the applied stress [2.5]. In the figure, x_o and x_p are direct orthoexciton and paraexciton luminescence, respectively, and the third unnamed peak is from the phonon-assisted orthoexciton luminescence.

2.3 OPG-OPA

In order to create excitons with resonant two-photon excitations in Cu_2O, I built an infrared Optical Parametric Generator-Amplifier (OPG-OPA).

2.3.1 What is an OPG-OPA?

The OPG-OPA is a solid-state tunable high-power laser source, which has some advantages over the dye laser, such as a much wider tuning range, not using toxic dyes, etc. The scheme

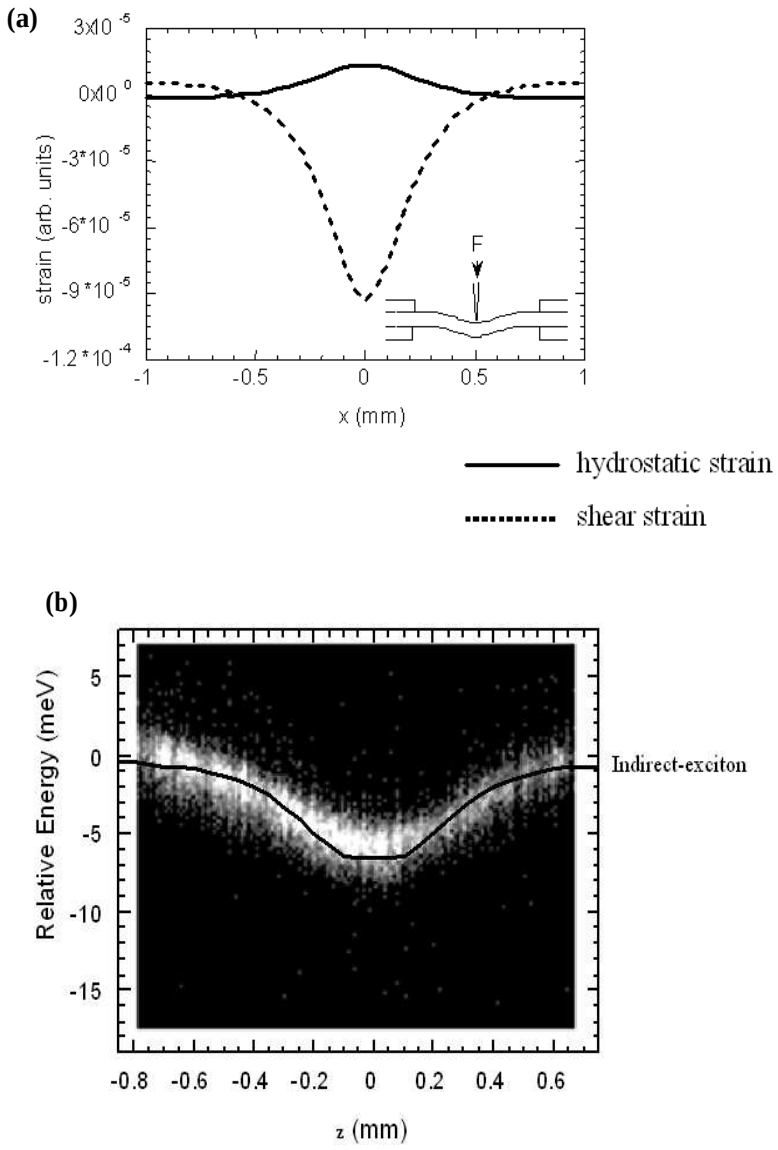

Figure 9: The finite element analysis for a free standing geometry in creating harmonic potential traps in the coupled quantum wells, (a). Theoretical solution; (b). Time-integrated image of the indirect exciton captured by the CCD camera. [2.2]

and tuning curve of OPG-OPA are shown in Fig 11 and 12 [2.6]. The main parts in the system are three $4 \times 4 \times 12$ mm type-1 nonlinear optical crystals, barium borate (BBO or β-BBO). A high-power 50Hz, 50ps, 532nm laser beam from a Regenerative Amplifier (RGA) is divided into two green beams, both of which are shrunk to 2mm diameter by two 2-to-1 telescopes. One green beam doubly passes BBO1 and BBO2 in an internal OPG-OPA system, and the

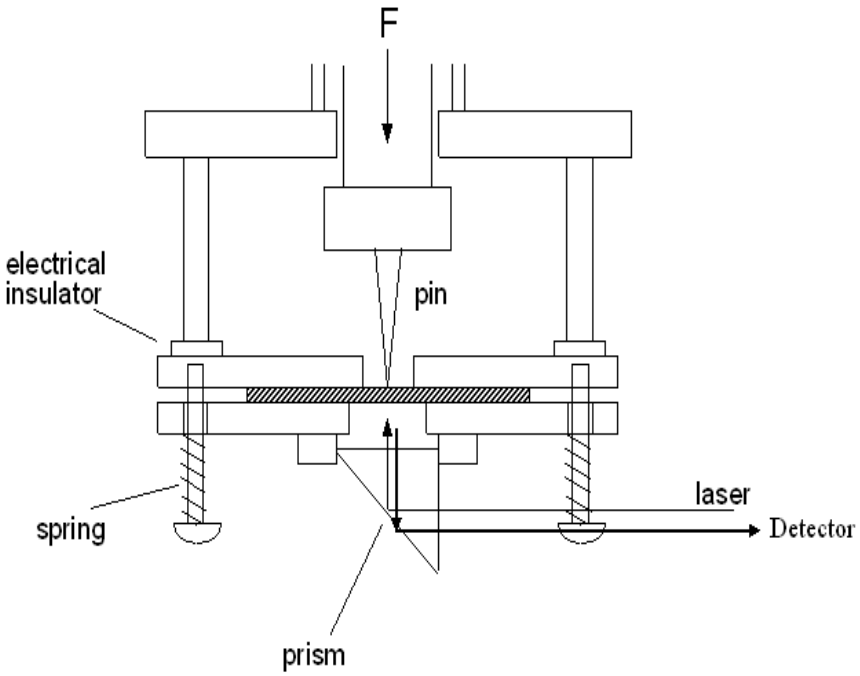

Figure 10: Schematic of the set-up for creating harmonic potential traps with a sharp pin in the coupled quantum wells structure.

second green beam after a proper time delay meets the output from the internal OPG-OPA system at BBO3 to do an additional amplification. In most of our experiments, BBO3 was removed, because the output from the internal OPG-OPA is 240 μJ/pulse-22ps at 1200nm, which is so powerful that it burnt the Cu_2O sample after a tightly focusing lens.

2.3.2 How does the OPG-OPA work?

OPG is a three-wave mixing process, in which a pump laser beam shines into a BBO crystal and divides into two parts, named the signal and idler. From energy conservation, the frequencies of the three beams will satisfy the relationship, $\omega_{pump} = \omega_{signal} + \omega_{idler}$. The phase velocity of an optical beam propagating in a nonlinear optical crystal depends on the polarization of its wave vector, and there are extra-ordinary and ordinary waves in the crystal, which is called birefringence [2.7]. For our type-1 BBO crystals, the pump is an extra-ordinary wave, while the signal and idler output are ordinary waves. When the BBO crystal is rotated, its index of refraction and three wave vectors change, so the wavelengths

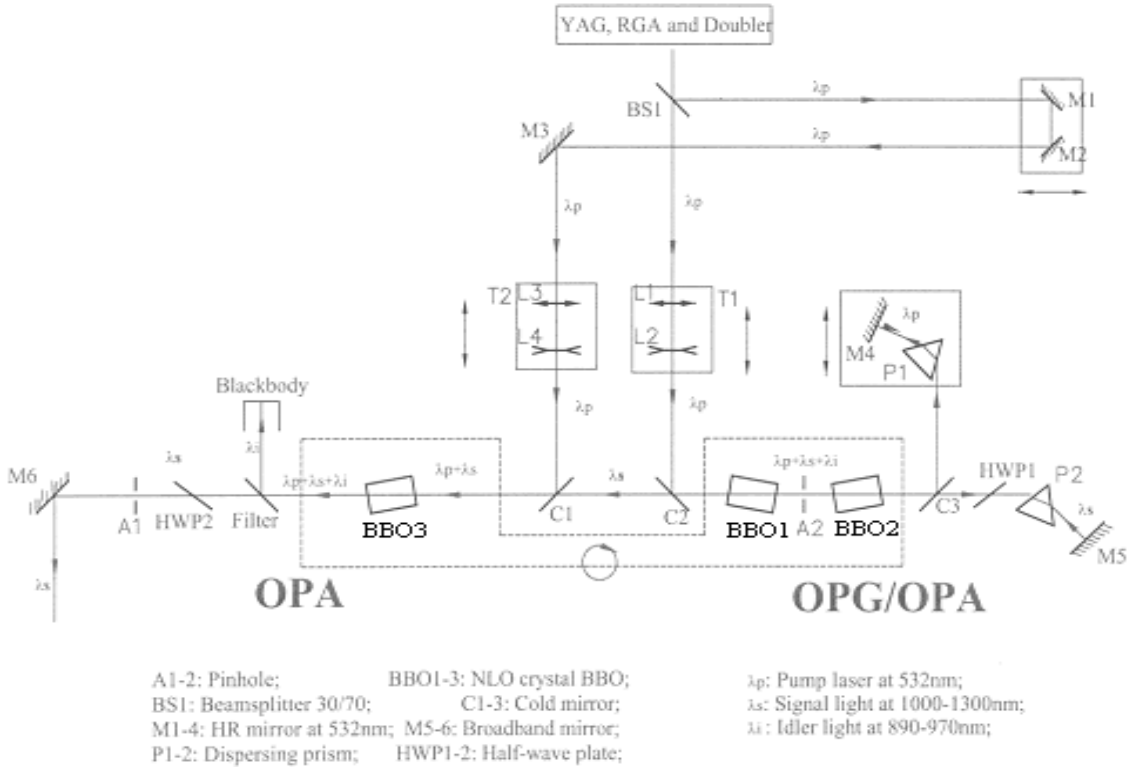

Figure 11: The Scheme of the home-built OPG-OPA.

of the signal and idler have to change to satisfy the energy and momentum conservations, as shown in Fig 12.

I can get a tunable infrared output from OPG by rotating the BBO crystal, but the output is very weak with a broad bandwidth, because a two-degree rotation covers a tuning range from 0.6 to 2.5 micrometers in wavelength for our system. To solve this problem, I put the second BBO crystal after the OPG to do an OPA process.

OPA is in fact a Difference-Frequency Generation (DFG) process, in which a weak signal wave and a strong pump wave incident on the BBO crystal at the same time produce an idler wave with frequency $\omega_{idler} = \omega_{pump} - \omega_{signal}$. Richard Sutherland's calculation from Jocobi Elliptic functions shows that the power of the signal and idler gain exponentially and the power of the pump depletes [2.8], as shown in Figure 13. For our 12 mm long BBO crystal, a one-pass OPA process with 1 mW signal input gives us 2.8 mW signal output and 1.8 mW idler output. With a reflecting mirror after BBO2, the two BBO crystals in the system

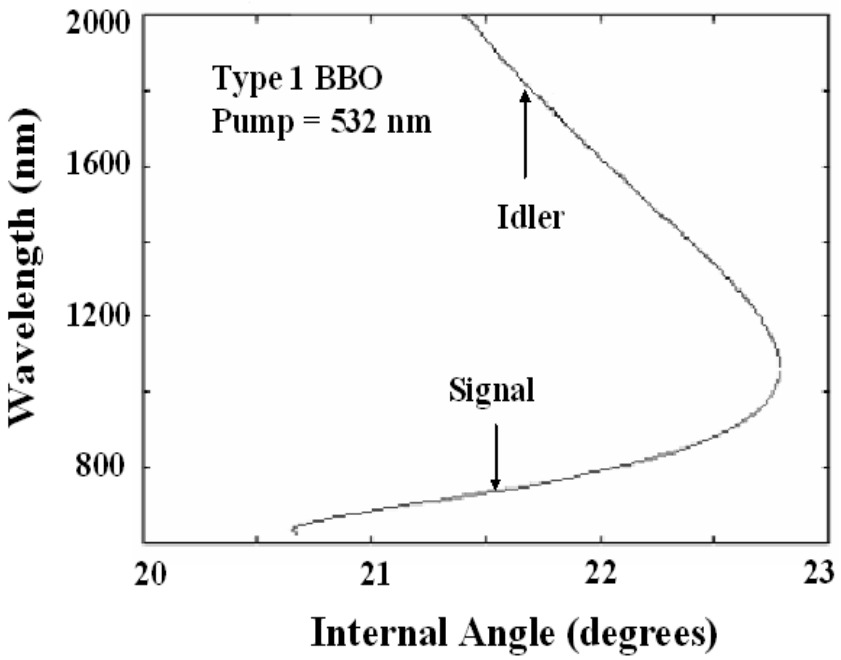

Figure 12: Tuning curve of the type-1 BBO crystal pumped by Nd:YAG laser at 532nm.

give us one OPG process and three OPA processes, which is equivalent to amplify the signal 22 times and the idler 21 times. Following J.Y. Zhang *et al.* [2.6], I narrowed the output bandwidth from hundreds of nanometers to 1.7 nanometer. First, I put the OPA system far away from the OPG system. Then BBO2 acts as a spatial and spectral filter, because only the central part of the broadband signal from the OPG overlaps with the pump wave and gets amplified in the OPA. But the power of the OPA output depends on that of the input signal. So if I put BBO2 too far away from BBO1, the power of the input signal will drop and correspondingly the power of the OPA output will drop dramatically. In our system, the trade-off distance between the two BBO crystals is 25 mm. Second, by tuning the two BBO crystals in opposite directions, the walk-off between the signal wave and pump wave is minimized. Third, I selected the pump and signal waves with a cold mirror and two prisms before reflect them back to BBO2 for the second and third OPA processes. The prisms can be replaced by two 1200-groove/mm high-resolution(90%) first-order replica diffraction gratings. Moreover, because only the signal overlapping with the pump pulse temporally is amplified, I put one of the two end mirrors on a translation stage to make sure that the

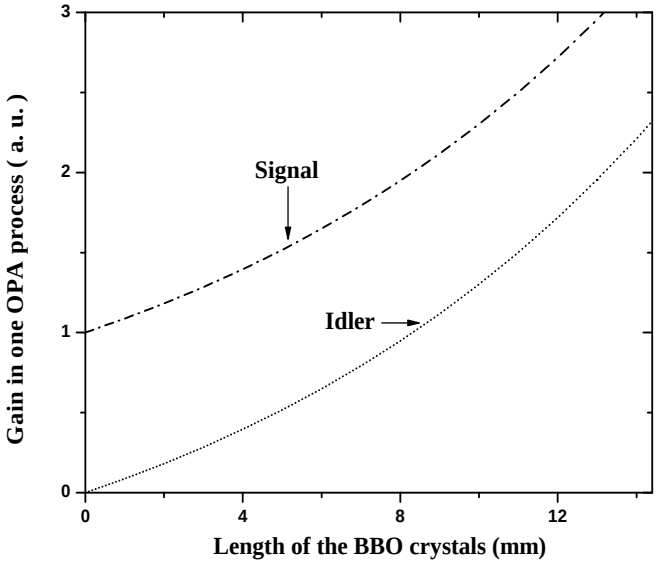

Figure 13: Power gain of the signal and idler output in OPA as a function of the length of the BBO crystal.

pump and signal meet at the same time on BBO2.

2.3.3 New OPA system

Because the PMT detects at most one photon per laser pulse and the repetition rate of the home-built OPG-OPA is too low, 50Hz, the necessary time to get a reasonable signal-to-noise ratio will be too long. Therefore most of the experiments of two-photon excitation are done with a commercial high repetition rate OPA laser system, of which the repetition rate, the duration and the spectral width are 250 KHz, 200 fs and 20 nm, respectively. The structure of the new OPA is as same as that of the home-built OPA, except that there is only one nonlinear crystal, type-2 BBO. And the high repetition rate of the new OPA is determined by the pump source, a femtosecond regenerative amplifier (REGA) which is seeded by a 76 MHz tunable Ti:Sapphire laser.

3.0 SELECTION RULES IN CUPROUS OXIDE

In order to understand the creation and detection of paraexcitons and orthoexcitons in the Cu_2O sample, I derived selection rules of excitons in Cu_2O from the group theory for both single-photon excitation (SPE) and two-photon excitation (TPE), which have been partially verified by the experiments mentioned in the next two chapters. The comprehensive selection rules for the paraexcitons and orthoexcitons under different external stresses and different exciton generation processes are listed in Table 4, and the derivation processes are shown in detail in the next two sections. Moreover, a listed "Allowed" transition in Table 4 has a strong

Conditions		**Single-photon excitation**		**Two-photon excitation**	
Transition	**Stress**	**Ortho**exciton	**Para**exciton	**Ortho**exciton	**Para**exciton
Dipole	Zero	Forbidden	Forbidden	Allowed	Forbidden
Dipole	[001]	Forbidden	Forbidden	Allowed	Allowed
Quadrupole	Zero	Allowed	Forbidden	Allowed	Forbidden
Quadrupole	[001]	Allowed	Allowed	Allowed	Allowed

Table 4: Selection rules of orthoexcitons and paraexcitons under different external stresses and different exciton generation processes. [001] in the table means that the applied stress is along the [001] crystalline axis.

polarization dependence, that is to say, the listed "Allowed" transitions can be forbidden for a certain input direction of the laser beam. The detailed polarization dependences for different conditions are discussed in Sections (3.1) and (3.2).

3.1 SELECTION RULES IN SPE

3.1.1 Without any external perturbation in SPE

Without any external perturbation, excitons in Cu_2O are in the O_h group. The symmetry properties of "yellow" excitons are shown in Table 5 [3.1].

O_h Group	Symmetry	Basis
Paraexciton	${}^1\Gamma_2^+$	$(x^2-y^2)(y^2-z^2)(z^2-x^2)$
Orthoexciton	${}^3\Gamma_5^+$	xy, yz, zx
Electric dipole operator	${}^3\Gamma_4^-$	x, y, z
Electric quadrupole operator	${}^3\Gamma_5^+; {}^2\Gamma_3^+$	$xy, yz, zx; (2z^2-x^2-y^2), \sqrt{3}(x^2-y^2)$

Table 5: The symmetry properties of "yellow" excitons and two operators in SPE without stresses.

For paraexciton Γ_2^+ in electric dipole transition:

$\Gamma_2^+ \otimes \Gamma_4^- = \Gamma_5^- \Rightarrow < \Gamma_1^+ \mid \Gamma_4^- \mid \Gamma_2^+ >= 0$, Forbidden;

For paraexciton Γ_2^+ in electric quadrupole transition:

$\Gamma_2^+ \otimes \Gamma_5^+ = \Gamma_4^+ \Rightarrow < \Gamma_1^+ \mid \Gamma_5^+ \mid \Gamma_2^+ >= 0$, Forbidden;

$\Gamma_2^+ \otimes \Gamma_3^+ = \Gamma_3^+ \Rightarrow < \Gamma_1^+ \mid \Gamma_3^+ \mid \Gamma_2^+ >= 0$, Forbidden;

For orthoexciton Γ_5^+ in electric dipole transition:

$\Gamma_5^+ \otimes \Gamma_4^- = \Gamma_2^- \oplus \Gamma_3^- \oplus \Gamma_4^- \oplus \Gamma_5^- \Rightarrow < \Gamma_1^+ \mid \Gamma_4^- \mid \Gamma_5^+ >= 0$, Forbidden;

For orthoexciton Γ_5^+ in electric quadrupole transition:

$\Gamma_5^+ \otimes \Gamma_5^+ = \Gamma_1^+ \oplus \Gamma_3^+ \oplus \Gamma_4^+ \oplus \Gamma_5^+ \Rightarrow < \Gamma_1^+ \mid \Gamma_5^+ \mid \Gamma_5^+ > \neq 0$, Allowed;

$\Gamma_5^+ \otimes \Gamma_3^+ = \Gamma_4^+ \oplus \Gamma_5^+ \Rightarrow < \Gamma_1^+ \mid \Gamma_3^+ \mid \Gamma_5^+ >= 0$, Forbidden;

So the only allowed direct transition is the orthoexciton quadrupole transition.

3.1.2 Under [001] stress in SPE

Under external [001] stress, excitons of Cu_2O are in the D_{4h} group along the stress axis, and in the D_{2h} group for most of the harmonic potential well. The symmetry properties of "yellow" excitons under [001] stress are shown in Table 6 [3.1].

Group	Exciton or operator	Symmetry	Basis
D_{4h}	Para-exciton	${}^1\Gamma_3^+$	(x^2-y^2)
	orthoexciton	${}^1\Gamma_4^+; {}^2\Gamma_5^+$	$xy; yz, zx$
	Dipole operator	${}^1\Gamma_2^-; {}^2\Gamma_5^-$	$z; x, y$
	Quadrupole operator	${}^2\Gamma_5^+; {}^1\Gamma_3^+; {}^1\Gamma_4^+; {}^1\Gamma_1^+$	$yz, zx; (x^2-y^2); xy; R$
D_{2h}	Para-exciton	${}^1\Gamma_1^+$	R
	orthoexciton	${}^1\Gamma_2^+; {}^1\Gamma_3^+; {}^1\Gamma_4^+$	$xz; xy; zy$
	Dipole operator	${}^1\Gamma_3^-; {}^1\Gamma_2^-; {}^1\Gamma_4^-$	$z; y; x$
	Quadrupole operator	${}^1\Gamma_1^+; {}^1\Gamma_2^+; {}^1\Gamma_3^+; {}^1\Gamma_4^+$	$R; zx; xy; yz$

Table 6: The symmetry properties of "yellow" excitons and two operators in SPE under [001] stress. R in the table means a function going to itself under all rotations.

First, for the excitons and operators in the D_{4h} group:

For paraexciton Γ_3^+ in electric dipole transition:

$\Gamma_3^+ \otimes \Gamma_2^- = \Gamma_4^- \Rightarrow < \Gamma_1^+ \mid \Gamma_2^- \mid \Gamma_3^+ >= 0$, Forbidden;

$\Gamma_3^+ \otimes \Gamma_5^- = \Gamma_5^- \Rightarrow < \Gamma_1^+ \mid \Gamma_5^- \mid \Gamma_3^+ >= 0$, Forbidden;

For paraexciton Γ_3^+ in electric quadrupole transition:

$\Gamma_3^+ \otimes \Gamma_1^+ = \Gamma_3^+ \Rightarrow < \Gamma_1^+ \mid \Gamma_1^+ \mid \Gamma_3^+ >= 0$, Forbidden;

$\Gamma_3^+ \otimes \Gamma_3^+ = \Gamma_1^+ \Rightarrow < \Gamma_1^+ \mid \Gamma_3^+ \mid \Gamma_3^+ > \neq 0$, Allowed;

$\Gamma_3^+ \otimes \Gamma_4^+ = \Gamma_2^+ \Rightarrow < \Gamma_1^+ \mid \Gamma_4^+ \mid \Gamma_3^+ >= 0$, Forbidden;

$\Gamma_3^+ \otimes \Gamma_5^+ = \Gamma_5^+ \Rightarrow < \Gamma_1^+ \mid \Gamma_5^+ \mid \Gamma_3^+ >= 0$, Forbidden;

For orthoexciton Γ_5^+, Γ_4^+ in electric dipole transition:

$\Gamma_5^+ \otimes \Gamma_2^- = \Gamma_5^- \Rightarrow < \Gamma_1^+ \mid \Gamma_2^- \mid \Gamma_5^+ >= 0$, Forbidden;

$\Gamma_5^+ \otimes \Gamma_5^- = \Gamma_1^- \Rightarrow < \Gamma_1^+ \mid \Gamma_5^- \mid \Gamma_5^+ > = 0$, Forbidden;

$\Gamma_4^+ \otimes \Gamma_2^- = \Gamma_3^- \Rightarrow < \Gamma_1^+ \mid \Gamma_2^- \mid \Gamma_4^+ > = 0$, Forbidden;

$\Gamma_4^+ \otimes \Gamma_5^- = \Gamma_5^- \Rightarrow < \Gamma_1^+ \mid \Gamma_5^- \mid \Gamma_4^+ > = 0$, Forbidden;

For orthoexciton Γ_5^+, Γ_4^+ in electric quadrupole transition:

$\Gamma_5^+ \otimes \Gamma_5^+ = \Gamma_1^+ \oplus \Gamma_2^+ \oplus \Gamma_3^+ \oplus \Gamma_4^+ \Rightarrow < \Gamma_1^+ \mid \Gamma_5^+ \mid \Gamma_5^+ > \neq 0$, Allowed;

$\Gamma_5^+ \otimes \Gamma_4^+ = \Gamma_5^+ \Rightarrow < \Gamma_1^+ \mid \Gamma_4^+ \mid \Gamma_5^+ > = 0$, Forbidden;

$\Gamma_5^+ \otimes \Gamma_3^+ = \Gamma_5^+ \Rightarrow < \Gamma_1^+ \mid \Gamma_3^+ \mid \Gamma_5^+ > = 0$, Forbidden;

$\Gamma_5^+ \otimes \Gamma_1^+ = \Gamma_5^+ \Rightarrow < \Gamma_1^+ \mid \Gamma_1^+ \mid \Gamma_5^+ > = 0$, Forbidden;

$\Gamma_4^+ \otimes \Gamma_5^+ = \Gamma_5^+ \Rightarrow < \Gamma_1^+ \mid \Gamma_5^+ \mid \Gamma_4^+ > = 0$, Forbidden;

$\Gamma_4^+ \otimes \Gamma_4^+ = \Gamma_1^+ \Rightarrow < \Gamma_1^+ \mid \Gamma_4^+ \mid \Gamma_4^+ > \neq 0$, Allowed;

$\Gamma_4^+ \otimes \Gamma_3^+ = \Gamma_2^+ \Rightarrow < \Gamma_1^+ \mid \Gamma_3^+ \mid \Gamma_4^+ > = 0$, Forbidden;

$\Gamma_4^+ \otimes \Gamma_1^+ = \Gamma_4^+ \Rightarrow < \Gamma_1^+ \mid \Gamma_1^+ \mid \Gamma_4^+ > = 0$, Forbidden;

Second, for the excitons and operators in the D_{2h} group:

For paraexciton Γ_1^+ in electric dipole transition:

$\Gamma_1^+ \otimes \Gamma_2^- = \Gamma_2^- \Rightarrow < \Gamma_1^+ \mid \Gamma_2^- \mid \Gamma_1^+ > = 0$, Forbidden;

$\Gamma_1^+ \otimes \Gamma_3^- = \Gamma_3^- \Rightarrow < \Gamma_1^+ \mid \Gamma_3^- \mid \Gamma_1^+ > = 0$, Forbidden;

$\Gamma_1^+ \otimes \Gamma_4^- = \Gamma_4^- \Rightarrow < \Gamma_1^+ \mid \Gamma_4^- \mid \Gamma_1^+ > = 0$, Forbidden;

For paraexciton Γ_1^+ in electric quadrupole transition:

$\Gamma_1^+ \otimes \Gamma_1^+ = \Gamma_1^+ \Rightarrow < \Gamma_1^+ \mid \Gamma_1^+ \mid \Gamma_1^+ > \neq 0$, Allowed;

$\Gamma_1^+ \otimes \Gamma_2^+ = \Gamma_2^+ \Rightarrow < \Gamma_1^+ \mid \Gamma_2^+ \mid \Gamma_1^+ > = 0$, Forbidden;

$\Gamma_1^+ \otimes \Gamma_3^+ = \Gamma_3^+ \Rightarrow < \Gamma_1^+ \mid \Gamma_3^+ \mid \Gamma_1^+ > = 0$, Forbidden;

$\Gamma_1^+ \otimes \Gamma_4^+ = \Gamma_4^+ \Rightarrow < \Gamma_1^+ \mid \Gamma_4^+ \mid \Gamma_1^+ > = 0$, Forbidden;

For orthoexciton $\Gamma_2^+, \Gamma_3^+, \Gamma_4^+$ in electric dipole transition:

$\Gamma_2^+ \otimes \Gamma_2^- = \Gamma_1^- \Rightarrow < \Gamma_1^+ \mid \Gamma_2^- \mid \Gamma_2^+ > = 0$, Forbidden;

$\Gamma_2^+ \otimes \Gamma_3^- = \Gamma_4^- \Rightarrow < \Gamma_1^+ \mid \Gamma_3^- \mid \Gamma_2^+ > = 0$, Forbidden;

$\Gamma_2^+ \otimes \Gamma_4^- = \Gamma_3^- \Rightarrow < \Gamma_1^+ \mid \Gamma_4^- \mid \Gamma_2^+ > = 0$, Forbidden;

$\Gamma_3^+ \otimes \Gamma_2^- = \Gamma_4^- \Rightarrow < \Gamma_1^+ \mid \Gamma_2^- \mid \Gamma_3^+ >= 0$, Forbidden;

$\Gamma_3^+ \otimes \Gamma_3^- = \Gamma_1^- \Rightarrow < \Gamma_1^+ \mid \Gamma_3^- \mid \Gamma_3^+ >= 0$, Forbidden;

$\Gamma_3^+ \otimes \Gamma_4^- = \Gamma_2^- \Rightarrow < \Gamma_1^+ \mid \Gamma_4^- \mid \Gamma_3^+ >= 0$, Forbidden;

$\Gamma_4^+ \otimes \Gamma_2^- = \Gamma_3^- \Rightarrow < \Gamma_1^+ \mid \Gamma_2^- \mid \Gamma_4^+ >= 0$, Forbidden;

$\Gamma_4^+ \otimes \Gamma_3^- = \Gamma_2^- \Rightarrow < \Gamma_1^+ \mid \Gamma_3^- \mid \Gamma_4^+ >= 0$, Forbidden;

$\Gamma_4^+ \otimes \Gamma_4^- = \Gamma_1^- \Rightarrow < \Gamma_1^+ \mid \Gamma_4^- \mid \Gamma_4^+ >= 0$, Forbidden;

For orthoexciton $\Gamma_2^+, \Gamma_3^+, \Gamma_4^+$ in electric quadrupole transition:

$\Gamma_2^+ \otimes \Gamma_1^+ = \Gamma_2^+ \Rightarrow < \Gamma_1^+ \mid \Gamma_1^+ \mid \Gamma_2^+ >= 0$, Forbidden;

$\Gamma_2^+ \otimes \Gamma_2^+ = \Gamma_1^+ \Rightarrow < \Gamma_1^+ \mid \Gamma_2^+ \mid \Gamma_2^+ > \neq 0$, Allowed;

$\Gamma_2^+ \otimes \Gamma_3^+ = \Gamma_4^+ \Rightarrow < \Gamma_1^+ \mid \Gamma_3^+ \mid \Gamma_2^+ >= 0$, Forbidden;

$\Gamma_2^+ \otimes \Gamma_4^+ = \Gamma_3^+ \Rightarrow < \Gamma_1^+ \mid \Gamma_4^+ \mid \Gamma_2^+ >= 0$, Forbidden;

$\Gamma_3^+ \otimes \Gamma_1^+ = \Gamma_3^+ \Rightarrow < \Gamma_1^+ \mid \Gamma_1^+ \mid \Gamma_3^+ >= 0$, Forbidden;

$\Gamma_3^+ \otimes \Gamma_2^+ = \Gamma_4^+ \Rightarrow < \Gamma_1^+ \mid \Gamma_2^+ \mid \Gamma_3^+ >= 0$, Forbidden;

$\Gamma_3^+ \otimes \Gamma_3^+ = \Gamma_1^+ \Rightarrow < \Gamma_1^+ \mid \Gamma_3^+ \mid \Gamma_3^+ > \neq 0$, Allowed;

$\Gamma_3^+ \otimes \Gamma_4^+ = \Gamma_2^+ \Rightarrow < \Gamma_1^+ \mid \Gamma_4^+ \mid \Gamma_3^+ >= 0$, Forbidden;

$\Gamma_4^+ \otimes \Gamma_1^+ = \Gamma_4^+ \Rightarrow < \Gamma_1^+ \mid \Gamma_1^+ \mid \Gamma_4^+ >= 0$, Forbidden;

$\Gamma_4^+ \otimes \Gamma_2^+ = \Gamma_3^+ \Rightarrow < \Gamma_1^+ \mid \Gamma_2^+ \mid \Gamma_4^+ >= 0$, Forbidden;

$\Gamma_4^+ \otimes \Gamma_3^+ = \Gamma_2^+ \Rightarrow < \Gamma_1^+ \mid \Gamma_3^+ \mid \Gamma_4^+ >= 0$, Forbidden;

$\Gamma_4^+ \otimes \Gamma_4^+ = \Gamma_1^+ \Rightarrow < \Gamma_1^+ \mid \Gamma_4^+ \mid \Gamma_4^+ > \neq 0$, Allowed;

Both orthoexciton and paraexciton quadrupole transitions are allowed.

3.1.3 Polarization dependence of photoluminescence in SPE

Because selection rules in the detection of exciton photoluminescence are equivalent to the selection rules of excitons in a single photon transition, and because the only allowed direct transition is the quadrupole transition in SPE as shown above, we can get the orientation rules for detecting the exciton photoluminescence in the Cu_2O sample from the quadrupole

operator Q [3.2]:

$$
\begin{aligned}
Q &= \sum_{i,j} k_i \lambda_j r_i r_j \\
&\Rightarrow Q = k_x\lambda_x x^2 + k_x\lambda_y(xy) + k_x\lambda_z(xz) + k_y\lambda_x(yx) + \\
&\quad + k_y\lambda_y y^2 + k_y\lambda_z(yz) + k_z\lambda_x(zx) + \\
&\quad + k_z\lambda_y(zy) + k_z\lambda_z z^2
\end{aligned} \tag{3.1}
$$

where **k** and λ are the input beam's wave vector and polarization vector.

Because only the orthoexciton is allowed in the quadrupole transition in SPE when there is no external stress, the only observed photoluminescence is from the orthoexciton; however, both orthoexciton and paraexciton luminescence can be detected when an external stress is applied on the sample. Table 7 lists the polarization vector for three different laser incident directions, in which HP is the direction of the horizontal polarization, and θ is the angle between the direction of the input beam's polarization and that of the horizontal polarization. The detailed selection rules in the detecting process are listed in Table 8 for different laser incident directions and under different stresses.

Wave vector	**Polarization** (l, m, n)			Horizontal Polarization
k	l	m	n	(HP)
(1, 0, 0)	0	$\cos\theta$	$\sin\theta$	[010]
(1, 1, 0)	$-\frac{\sqrt{2}}{2}\cos\theta$	$\frac{\sqrt{2}}{2}\cos\theta$	$\sin\theta$	$[1\bar{1}0]$
(1, 1, 1)	$-\frac{\sqrt{2}}{2}\cos\theta - \frac{1}{\sqrt{6}}\sin\theta$	$\frac{\sqrt{2}}{2}\cos\theta - \frac{1}{\sqrt{6}}\sin\theta$	$\frac{2}{\sqrt{6}}\sin\theta$	$[1\bar{1}0]$

Table 7: Polarization vector for three different laser incident directions.

3.2 SELECTION RULES IN TPE

3.2.1 Without any external perturbation

For our one-beam two-photon excitation, the two input beams have the same energy, $\omega_1 = \omega_2 = \omega$, and the same polarization, $\lambda_1 = \lambda_2 = \lambda$. Therefore, the absorption coefficient in

Symmetry group	Single-photon transitions	Wave vector **k**	Orthoexciton	Paraexciton
O_h	Dipole	All	Forbidden	Forbidden
O_h	Quadrupole	(1, 0, 0)	1	Forbidden
		(1, 1, 0)	$\sin^2\theta$	Forbidden
		(1, 1, 1)	1	Forbidden
D_{4h}	Dipole	All	Forbidden	Forbidden
D_{4h}	Quadrupole	(1, 0, 0)	1	Forbidden
		(1, 1, 0)	$\sin^2\theta$	$\cos^2\theta$
		(1, 1, 1)	1	$\cos^2\theta$
D_{2h}	Dipole	All	Forbidden	Forbidden

Table 8: Polarization dependence of orthoexcitons and paraexcitons in the dipole and quadrupole transitions for various symmetries in single-photon excitation, where θ is the angle between the horizontal polarization and the polarization of the input IR beam.

dipole transition is proportional to:

$$\sum_j |\sum_i \frac{\langle \Gamma_{ex} \mid D_j \mid i\rangle\langle i \mid D_j \mid \Gamma_1^+\rangle}{E_i - \hbar\omega}|^2, \tag{3.2}$$

where $\mid i\rangle$ are the intermediate states, Γ_1^+ and Γ_{ex} are the vacuum state and the 1s-"yellow" exciton state respectively. $D_j = \hat{\lambda} \cdot p_j$ are possible dipole operators for a certain input polarization λ, where p_j are operators $\hat{x}$, $\hat{y}$ and $\hat{z}$ in three dimensions.

Because the dipole operator is Γ_4^- in the O_h group, all allowed internal states should have negative parity, which could be the p-states in the "yellow" exciton series, the "blue" and "indigo" exciton series [3.1]. By taking into account the energy difference between the "yellow", "blue" and "indigo" excitons, the dominant internal states are the $2p$-"yellow" excitons with Γ_2^-, Γ_3^-, Γ_4^- and Γ_5^- symmetries.

To get a general polarization dependence for excitons in the dipole transition, we substitute the three possible dipole operators and possible symmetries of the $2p$-"yellow" exciton states into equation (3.2), and find that the dipole transitions for paraexcitons are forbidden

O_h Group	Symmetry	Basis
$2p$-"yellow" excitons	${}^1\Gamma_2^-$	xyz
	${}^2\Gamma_3^-$	$\sqrt{3}(x^2-y^2)xyz, (2z^2-x^2-y^2)xyz$
	${}^3\Gamma_4^-$	x, y, z
	$2({}^3\Gamma_5^-)$	$(x^2-y^2)(y^2-z^2)(z^2-x^2)xyz(yz)$
		$(x^2-y^2)(y^2-z^2)(z^2-x^2)xyz(yx)$
		$(x^2-y^2)(y^2-z^2)(z^2-x^2)xyz(xz)$
$2s$-"yellow" excitons	${}^3\Gamma_5^+$	xy, yz, zx
	${}^1\Gamma_2^+$	$(x^2-y^2)(y^2-z^2)(z^2-x^2)$

Table 9: The symmetry properties of the intermediate states for both dipole and quadrupole transitions in TPE without stress.

and the absorption coefficient in the dipole matrix element for orthoexcitons is proportional to,

$$I_{ortho}^{no-stress} \quad \propto \quad m^2n^2 + l^2(m^2+n^2). \tag{3.3}$$

Equation (3.3), the polarization dependence for excitons in the dipole transition matrix element without stress, is explicitly listed in Table 11.

In the quadrupole transition, the absorption coefficient can be calculated in the same way, which is proportional to:

$$\sum_j |\sum_i \frac{\langle \Gamma_{ex} \mid Q_j \mid i\rangle\langle i \mid Q_j \mid \Gamma_1^+\rangle}{E_i - \hbar\omega}|^2, \tag{3.4}$$

where $\mid i\rangle$ are the intermediate states, Γ_1^+ and Γ_{ex} are the vacuum state and the 1s-"yellow" exciton state respectively. Q_j are possible quadrupole operators for a certain input polarization λ, which are given by equation (3.1).

It is not possible to have a mixed dipole-quadrupole transition because the two operators have different parities, and there is no allowed internal state for the mixed transition.

There are five possible quadrupole operators in the O_h group, three-fold Γ_5^+ and two-fold Γ_3^+, as listed in Table 9. Because the five quadrupole operators have positive parity, all

neighboring exciton states with positive parity can be the intermediate states for the two-photon quadrupole transition. However, the dominant internal states are the $2s$-"yellow" exciton states, which are the closest neighbor for paraexcitons and orthoexcitons in energy. The polarization dependence of orthoexcitons and paraexcitons are calculated from equation (3.4) with the five possible quadrupole operators and four $2s$-"yellow" exciton states, as listed in Table 11.

3.2.2 Under [001] stress

Symmetry group	Internal states	Symmetry	Basis
D_{4h}	$2p$-"yellow" excitons	${}^1\Gamma_1^-$	$(x^2-y^2)xyz$
		${}^1\Gamma_2^-$	z
		$2({}^1\Gamma_3^-)$	xyz
		$2({}^1\Gamma_4^-)$	$(x^2-y^2)z$
		$3({}^2\Gamma_5^-)$	x, y
	$2s$-"yellow" excitons	${}^2\Gamma_5^+$	yz, zx
		${}^1\Gamma_4^+$	xy
		${}^1\Gamma_3^+$	(x^2-y^2)
D_{2h}	$2p$-"yellow" excitons	$3({}^1\Gamma_1^-)$	xyz
		$3({}^1\Gamma_2^-)$	y
		$3({}^1\Gamma_3^-)$	$(x^2-y^2)z$
		$3({}^1\Gamma_4^-)$	x
	$2s$-"yellow" excitons	${}^1\Gamma_2^+$	zx
		${}^1\Gamma_3^+$	xy
		${}^1\Gamma_4^+$	yz
		${}^1\Gamma_1^+$	R

Table 10: The symmetry properties of the intermediate states for both dipole and quadrupole transitions in TPE under the stress along the [001] axis. R in the table means a function going to itself under all rotations.

When an external stress is applied along the [001] stress, the polarization dependence of paraexcitons and orthoexcitons in the dipole and quadrupole matrix elements are calculated in the same way as discussed in Section (3.2.1), from equations (3.2) and (3.4), except that the allowed intermediate states are different in the D_{4h} and D_{2h} groups. Because the dipole operators still have negative parity in D_{4h} and D_{2h} groups, the dominant intermediate states should be the closest negative parity states, the $2p$-"yellow" exciton states. And the $2s$-"yellow" exciton states still make the biggest contribution in the quadrupole transition. The calculation results from equations (3.2) and (3.4) by substituting the dominant intermediate states listed in Table 10, are explicitly shown in Table 11. The quadrupole transition in the D_{2h} group is not considered, because the direct dipole transition is already allowed in this symmetry group.

3.3 CONCLUSIONS

The real experimental set-up, or in other words, the orientation of the Cu_2O sample in our experiments explored in Chapters 4 and 5, is determined by the selection rules listed in Tables 4 to 11:

1. In order to create the 1s-"yellow" paraexcitons directly, an external perturbation is necessary, for example with a uniaxial inhomogeneous stress. For most of our experiments, we apply the external stress along the [001] axis, because it is easy to be established experimentally.

2. In order to detect the paraexciton, the lowest exciton state, via single-photon emission, the detector has to face a surface along either the [110] or [111] axis of the Cu_2O sample.

3. Our selection rules show that the direct two-photon creation is possible for orthoexcitons in both the dipole and quadrupole transitions which is confirmed by the reports from Ketterson *et al.* [3.4] and Shen *et al.* [3.5], and the polarization dependence for the orthoexcitons without stress is consistent with the experimental report from Kono *et al.* [3.6] and Kubouchi *et al.* [3.7]. Our calculations also indicate that direct two-photon creation of paraexcitons is possible under stress via both dipole and quadrupole matrix elements. Ketterson *et al.*[3.4], Kono *et al.* [3.6], Kubouchi *et al.* [3.7] and Shen *et al.*[3.5] didn't detect

Symmetry group	Two-photon transitions	Wave vector **k**	Orthoexciton	Paraexciton
O_h	Dipole	(1, 0, 0)	$\sin^2 2\theta$	Forbidden
		(1, 1, 0)	$\sin^2 2\theta + \cos^4 \theta$	Forbidden
		(1, 1, 1)	1	Forbidden
O_h	Quadrupole	(1, 0, 0)	$\sin^2 2\theta$	Forbidden
		(1, 1, 0)	$(1 + a\cos 2\theta)\sin^2 \theta$	Forbidden
		(1, 1, 1)	$(1 + a\cos 2\theta + b\cos 4\theta)$	Forbidden
D_{4h}	Dipole	(1, 0, 0)	$\sin^2 2\theta$	$\cos^4 \theta$
		(1, 1, 0)	$\sin^2 2\theta + \cos^4 \theta$	Forbidden
		(1, 1, 1)	1	$\sin^2 2\theta$
D_{4h}	Quadrupole	(1, 0, 0)	$\sin^2 2\theta$	$\sin^4 \theta$
		(1, 1, 0)	$(1 + a\cos 2\theta)\sin^2 \theta$	Forbidden
		(1, 1, 1)	$(1 + a\cos 2\theta + b\cos 4\theta)$	$\sin^2 2\theta$
D_{2h}	Dipole	(1, 0, 0)	$\sin^2 2\theta$	$(a\cos^2 \theta + b\sin^2 \theta)^2$
		(1, 1, 0)	$\sin^2 2\theta + \cos^4 \theta$	$(a\cos^2 \theta + b\sin^2 \theta)^2$
		(1, 1, 1)	1	$(1 + a\cos 2\theta + b\sin 2\theta)^2$

Table 11: Polarization dependence of orthoexcitons and paraexcitons in the dipole and quadrupole transitions for various symmetries in two-photon excitation, where a and b are constant factors which depend on the matrix elements to the internal states. θ is the angle between the horizontal polarization and the polarization of the input IR beam.

the paraexciton luminescence because they used an unstressed crystal. The observation of the paraexciton in TPE has been reported by Naka *et al.* [3.8] and by us [3.9], and the polarization dependence of the paraexcitons is consistent with our experimental results, as shown in Chapter 5.

4.0 SPIN FLIP AND EXCITONIC AUGER RELAXATION PROCESSES IN CUPROUS OXIDE

This chapter presents our experimental and theoretical results about the exciton relaxation processes in this chapter, which are important for the search for BEC of excitons in Cu_2O. The evolution of the orthoexciton and paraexciton populations has been studied, following their creation by a short laser pulse, for a range of excitation densities, temperatures, and applied stresses. Both of these states can be observed by time-resolved luminescence. Photon emission from the paraexciton state is forbidden by symmetry at zero stress, but when uniaxial stress is applied, luminescence from this state becomes allowed, as shown in detail in Chapter 3. By monitoring the intensity of the luminescence from both species as a function of time following a short laser pulse, we can deduce the rate of conversion from orthoexcitons to paraexcitons, as well as the other relaxation rates of the excitons such as radiative lifetime and non-radiative Auger recombination [4.1]. At low temperatures, any contribution of exciton diffusion to the observed decay are ruled out by confining the excitons in a harmonic potential trap inside the crystal, which is created by using slightly inhomogeneous stress [4.2].

4.1 SPIN FLIP BY ACOUSTIC PHONON EMISSION

At very low laser power and at low temperature (2 Kelvin), the rate of decay of the orthoexciton luminescence intensity becomes independent of laser power, i.e. independent of the exciton density. This rules out any two-body collisional processes for the decay of the orthoexcitons at these low densities. In this low-density regime, we find that the rate of

orthoexciton conversion rate to paraexcitons becomes slower with increasing stress, as seen in Figure 14.

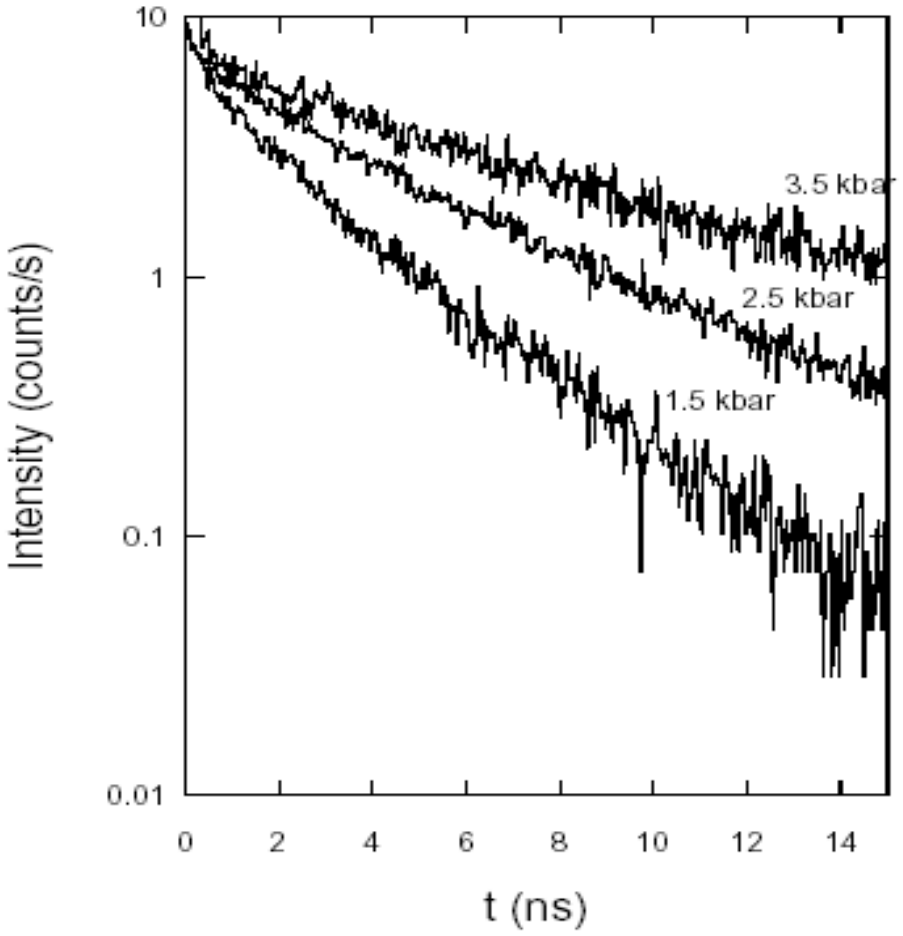

Figure 14: Decay of the orthoexciton phonon-assisted luminescence at three different stresses, under identical excitation conditions, at T = 2 K.

Fig. 15 gives a summary of the stress dependence of the orthoexciton-paraexciton conversion rate. At zero stress, the orthoexcitons convert to paraexcitons with a time constant of approximately 2 ns [4.3], while at high stress, the decay time exceeds 10 ns [4.1]. We establish that we are measuring the orthoexciton conversion rate into paraexcitons by monitoring both the orthoexciton decay rate and the rise time of the paraexciton luminescence intensity, which is consistent with the decay time of the orthoexcitons. Radiative decay of both species to photons occurs much more slowly. At T = 2 K, there is no appreciable up-conversion of paraexcitons to orthoexcitons.

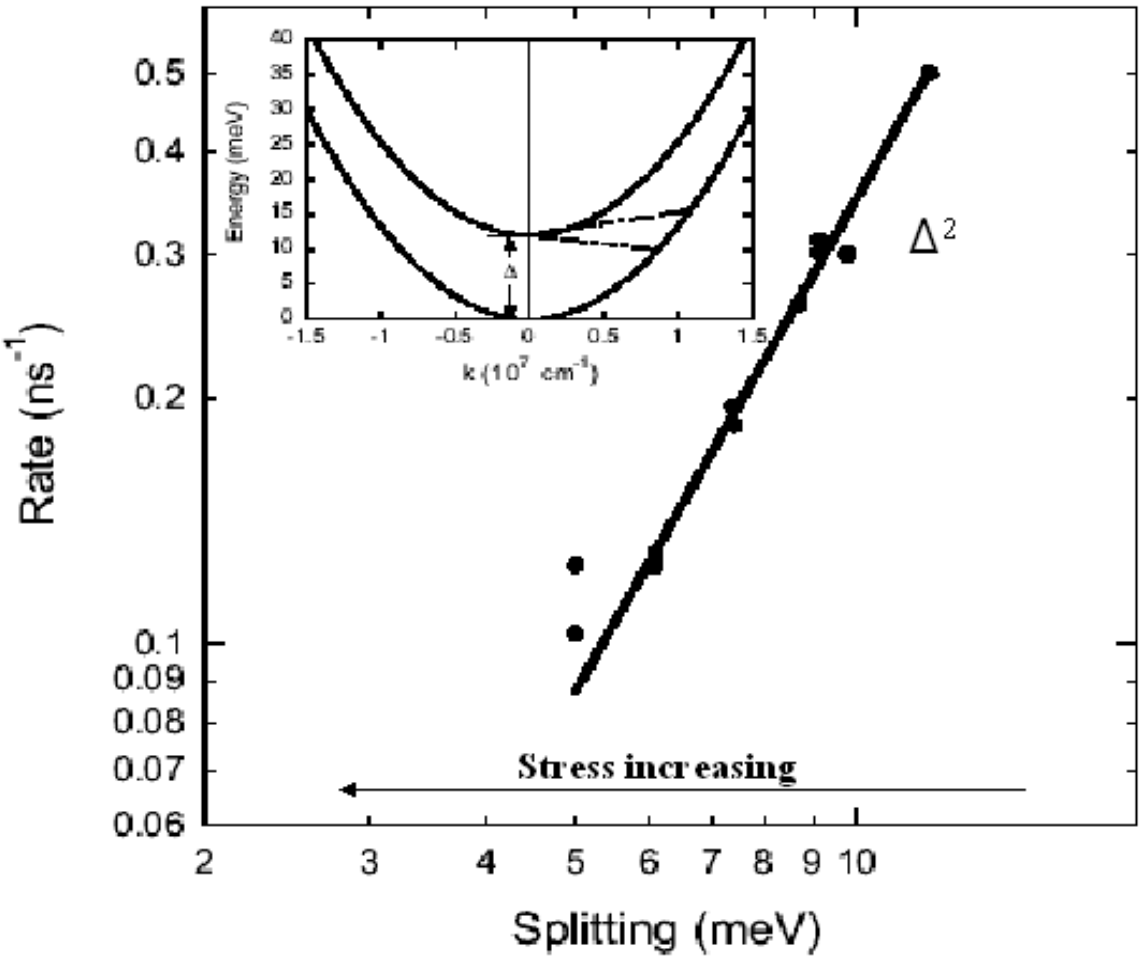

Figure 15: Solid circles: conversion rate of orthoexcitons to paraexcitons at low density as a function of the orthoexciton-paraexciton energy splitting, which is a function of the stress, from Ref. [4.14]. Solid line: best fit to a Δ^2 power law. Inset: the relative energies of the orthoexciton (upper level), paraexciton (lower level) and acoustic phonons involved in the conversion process.

The rate of exciton spin flip by phonon emission can be estimated simply based on a single-phonon emission model, in which the phonon emission is forbidden by symmetry at zone center, as in the case of Cu_2O. Both the orthoexciton and paraexciton states have positive parity, and the acoustic phonons have negative parity. The inset of Fig. 15 illustrates the acoustic phonon emission and absorption process. At low temperature, the orthoexciton momentum is negligible compared to the final paraexciton momentum. Therefore in $k \cdot p$ theory [4.4], the paraexciton Bloch periodic function can be written simply in terms of the

paraexciton momentum $\mathbf{k}$ as

$$|p(\mathbf{k})\rangle \quad = \quad |p(\mathbf{0})\rangle + \sum_i |i\rangle \frac{\hbar\mathbf{k}\cdot\langle i|\mathbf{p}|p(0)\rangle}{m_0(E_0 - E_i)} \tag{4.1}$$

where m_0 is the free electron mass, and $|i\rangle$ is an intermediate state. The nearest excitonic state with negative parity is the so called $2p$-"yellow" exciton, which lies 0.074 eV above the lowest exciton level [4.5]. Ignoring the contribution of all other intermediate states, due to their suppression by the energy denominator in Eq. (4.1), the matrix element for phonon emission from the orthoexciton ground state to a paraexciton state at finite $\mathbf{k}$ is therefore equal to

$$< o(0)|H_D|p(\mathbf{k}) > \quad = \quad \frac{< o(0)|H_D|b(0) > \hbar\mathbf{k}\cdot < b(0)|\mathbf{p}|p(0) >}{m_0(E_y - E_b)} \tag{4.2}$$

where $|b(0) >$ is a zone-center $2p$-"yellow" exciton state, H_D is the exciton-phonon deformation potential Hamiltonian, and $(E_y - E_b)$ is the difference in energy between the $1s$-"yellow" and $2p$-"yellow" exciton states. In general, the deformation Hamiltonian has the form $H_D = b\epsilon$, where b is a deformation potential and ϵ is the crystal strain, which for an acoustic phonon is proportional to the square root of k [4.6].

By Fermi's Golden Rule, the rate of this acoustic phonon emission process is proportional to the square of the matrix element in Eq. (4.2), which is proportional to k^3. The density of final paraexciton states is proportional to k, so that the total rate of spin flip by phonon emission is predicted to be proportional to k^4. As illustrated in the inset of Figure 15, the acoustic phonon emission process is nearly a horizontal process in Cu_2O, so that the k-vector of the transition is proportional to $\sqrt{\Delta}$. The single-phonon emission model therefore predicts a stress dependence of the ortho-para conversion rate proportional to Δ^2. The solid line in Fig. 15 shows a fit to this power law.

It is counterintuitive to many that a phonon can carry angular momentum and participate in a spin-flip process. The case of a transverse phonon is not fundamentally different from the case of a transverse photon, however, and it is well known that photons can flip electronic spin. Any transverse field can carry angular momentum. The agreement of theory and experiment in these measurements shows that phonon emission is indeed the dominant mechanism for spin flip converting orthoexcitons to paraexcitons.

4.2 STRESS DEPENDENCE OF THE AUGER RECOMBINATION RATE

At high densities, the evolution of the orthoexciton and paraexciton intensities begins to vary significantly with the laser power. The initial decay rate of the orthoexciton becomes shorter, and the rise time of the paraexciton luminescence becomes shorter as well. Fig. 16 shows typical data at high density.

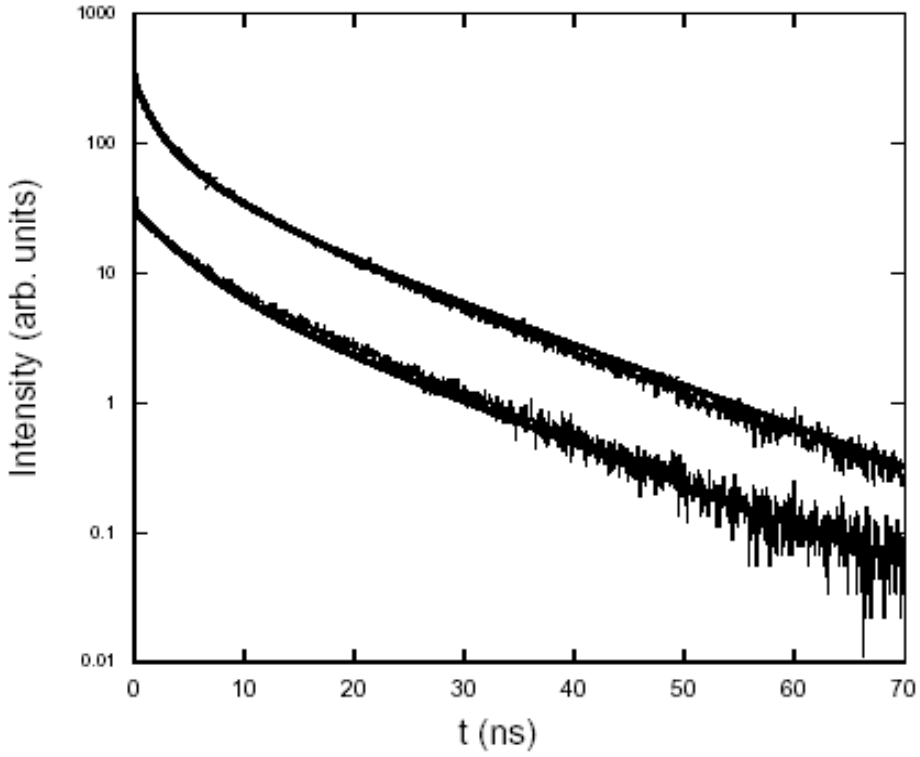

Figure 16: Comparison of the orthoexciton luminescence decay at 3.5 Kbar and T = 2 K, at two exciton densities different by a factor of 10. The heavy lines are the best fit to the rate equation theory presented in Ref. [4.14].

The Auger rate is given in terms of the Auger constant A, according to the following coupled rate equations,

$$\frac{dn_o}{dt} = -\frac{n_o}{\tau_{o-p}} - A_o n_o^2 + \frac{3}{8}(A_o n_o^2 + A_p n_p^2) - \frac{n_o}{\tau_o} \quad , \tag{4.3}$$

$$\frac{dn_p}{dt} = \frac{n_o}{\tau_{o-p}} - A_p n_p^2 + \frac{1}{8}(A_o n_o^2 + A_p n_p^2) - \frac{n_p}{\tau_p} \quad . \tag{4.4}$$

In these equations, indies o and p mean "orthoexciton" and "paraexciton" respectively, A is Auger decay constant, n is the exciton density, τ is the decay time or conversion time, and the index o-p means orthoexciton-paraexciton conversion. In each Auger process, two excitons collide and end up with one exciton recombining and the other exciton ionizing. Therefore, only the ionized exciton, half of the excitons participating in the Auger process, will be added back to exciton population. Because the orthoexciton is a triplet state and the paraexciton is a singlet state and spin is randomly selected in ionization, $\frac{3}{4}$ of the ionized excitons in the Auger process will be returned as orthoexcitons and $\frac{1}{4}$ of these excitons will be returned as paraexcitons. The paraexcitons and the orthoexcitons can have different

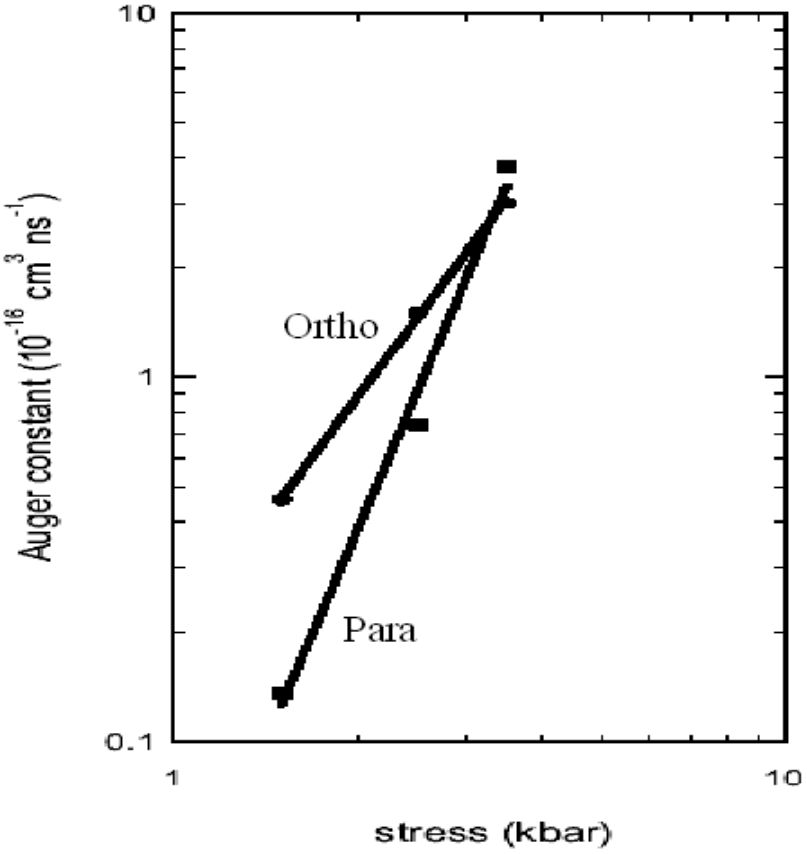

Figure 17: The Auger rates as a function of stress, deduced from fits to the orthoexciton and paraexciton time-resolved luminescence. The solid lines are best fits to a power law; for the orthoexcitons the best fit to the Auger rate is $A \propto \sigma^{2.2}$, and for the paraexcitons the best fit is $A \propto \sigma^{3.9}$.

values for A. We can estimate the absolute magnitude of A by knowing the total number

of excitons from the amount of light absorbed and the volume of the exciton cloud in the stress-induced trap, measured by spatial imaging [4.2]. We find that the Auger constant depends on stress. Fig. 17 shows a summary of the fit values of A for the paraexcitons and orthoexcitons. The solid lines in Fig. 17 are best fit to a power law; for the orthoexcitons the best fit to the Auger rate is $A \propto \sigma^{2.2}$, and for the paraexcitons the best fit is $A \propto \sigma^{3.9}$.

4.3 TEMPERATURE-DEPENDENT AUGER PROCESS

Fig. 17 implies that the Auger rate at zero stress and low temperature is very low; in our data the evolution of the luminescence intensity of both species of excitons is nearly identical at all densities at low stress. This seems to contradict earlier results by O'Hara, Gullingsrud, and Wolfe [4.7] who found a high Auger constant at zero stress. In those experiments, however, the excitons had high temperature, $T = 70K$ or higher, while in our experiments on the stress dependence, the excitons were at $T = 2$K. Ref. [4.14] also left one question in doubt, why there is apparently a very small Auger effect at stresses lower than 1.5 kbar at 2 Kelvin, while a strong Auger effect must occur with surface excitation with a negligible stress at higher temperatures, for example at room temperature. Does the surface play an important role in the Auger effect, or is the Auger effect temperature dependent? The problem became even more complicated when Jolk, Jörger, and Klingshirn [4.8] reported a Auger constant which is five orders magnitude less at zero stress at low temperature.

In this section, our theoretical and experimental results answer the above questions, by showing that the Auger recombination constant is weakly dependent on temperature when the temperature is lower than 77 Kelvin, and linearly increasing with temperature at high temperatures.

4.3.1 Experiment

Because of the short absorption length at high temperature, we cannot confine the excitons in a trap. Excitons are created at one [110] surface of a $4.9 \times 3 \times 3$ mm naturally-grown, high-quality Cu_2O crystal with single-photon near-resonant excitation under negligible ap-

plied stress in the high temperature region, 115∼325 Kelvin. An imaging lens collects exciton luminescence from the same [110] surface and focuses the light onto the entrance slit of a $\frac{1}{4}$-meter spectrometer which is connected with a CCD camera and a photomultiplier (PMT). The exciton population dynamics are examined by means of time-correlated single photon detection. This experimental approach has several advantages. First, in the high temperature region, paraexciton-to-orthoexciton conversion causes the excitons to reach thermal equilibrium quickly. Second, because of the high exciton-phonon scattering rate at high temperatures, the excitons do not diffuse out of the excitation region. Therefore the diffusion constant at high temperature is much smaller than that at low temperature which allows a constant-volume measurement, as pointed out by Warren, O'Hara and Wolfe [4.9]. We can estimate the volume of the excitons knowing the laser focus size and the absorption length of the laser light. Also, in these experiments, we use a cavity-dumped ultra-fast dye laser which has a long period, 260 ns between pulses. Therefore paraexcitons definitely reach thermal equilibrium with orthoexcitons. The bath temperature in the experiments is controlled by a homemade PID controller with an accuracy of ± 2 Kelvin.

In Cu_2O, there are two possible single-photon transitions, a direct transition by emitting a photon, and a phonon-assisted transition by emitting a photon and an optical phonon. Because the indirect transition is allowed for all exciton states, the indirect phonon-assisted luminescence spectrum shows the energy distribution of excitons [4.10]. At high temperature, the direct single-photon transitions for orthoexcitons and paraexcitons are almost forbidden, while the phonon-assisted process depends weakly on temperature [4.11]. In Section (4.3.3), we will talk about phonon-assisted orthoexciton recombination processes, assisted by all possible optical phonons and acoustic phonons, although the orthoexciton creation process via a Γ_{12}^- longitudinal optical phonon is much stronger than other phonon-assisted orthoexciton creation processes [4.11].

In the surface excitation, the absorption coefficient of Cu_2O has a strong dependence on bath temperature and laser photon energy[4.12, 4.13]. We calculate absorption lengths of Cu_2O for the input laser at 606 nm and for the orthoexciton luminescence at each temperature from Pastrnyak's report [4.12] and J. B. Grun's paper [4.13] on the absorption coefficient of Cu_2O, as shown in Fig 18. With a focused laser spot with radius of 120 μm, the orthoex-

citon has a volume of $\pi\times(120\ \mu\text{m})^2\times$(Absorption-length), which is of the order of $10^{-6}cm^{-3}$. As we did in previous works [4.14, 4.11], we assume that one absorbed photon produces an exciton, since the laser is tuned close to the exciton resonance. At the highest laser power of 2.64 nJ per pulse, with 30% absorbed in the crystal after considering all the optics involved, there are 10^9 orthoexcitons created initially, which implies an initial orthoexciton density of the order of $10^{15}cm^{-3}$.

Because the absorption length at the orthoexciton luminescence line is of the order of a millimeter at high temperatures, which is comparable to the width of Cu_2O sample, we have to add a correction factor to deduce the exciton density from the luminescence intensity at each temperature. The correction factor, CF, is equal to the ratio between $I_{detected}$, the real detected luminescence intensity, and I_0, the ideal detected luminescence intensity without taking into account of the absorption of the luminescence in Cu_2O, by a Photomultiplier.

If we assume that one absorbed photon creates one exciton, the total number of excitons at a certain position x in the sample, is proportional to the number of absorbed photons, $n_x \propto (e^{\frac{-x}{L_1}})$, where $0 \leq x \leq L$ and L, the width of Cu_2O, is 3 millimeter. L_1 and L_2 are the absorption lengths for the laser and orthoexciton luminescence respectively at each temperature. Because of the absorption of the exciton luminescence in the sample, the number of the detected exciton from the position x is proportional to $(e^{\frac{-x}{L_2}})$. In other words, the total contribution to the luminescence from the position x is proportional to $(e^{\frac{-x}{L_1}}e^{\frac{-x}{L_2}})$.

Therefore, the detected luminescence intensity is proportional to the integration of the detected excitons over the whole length of the sample, and the correction factor is calculated as the following,

$$CF = \frac{I_{detected}}{I_0} = \int_0^L e^{\frac{-x}{L_1}} e^{\frac{-x}{L_2}} dx \quad \div \quad \int_0^L e^{\frac{-x}{L_1}} dx \tag{4.5}$$

$$\Rightarrow CF = \frac{1}{L_1} \cdot \frac{1}{\frac{1}{L_1}+\frac{1}{L_2}} \cdot \frac{1-e^{-L(\frac{1}{L_1}+\frac{1}{L_2})}}{1-e^{-\frac{L}{L_1}}} \tag{4.6}$$

In principle, we should account for re-emission from the reabsorbed photons, but since the re-emission mostly goes in directions other than x (see inset of Figure 18), this will be a small correction.

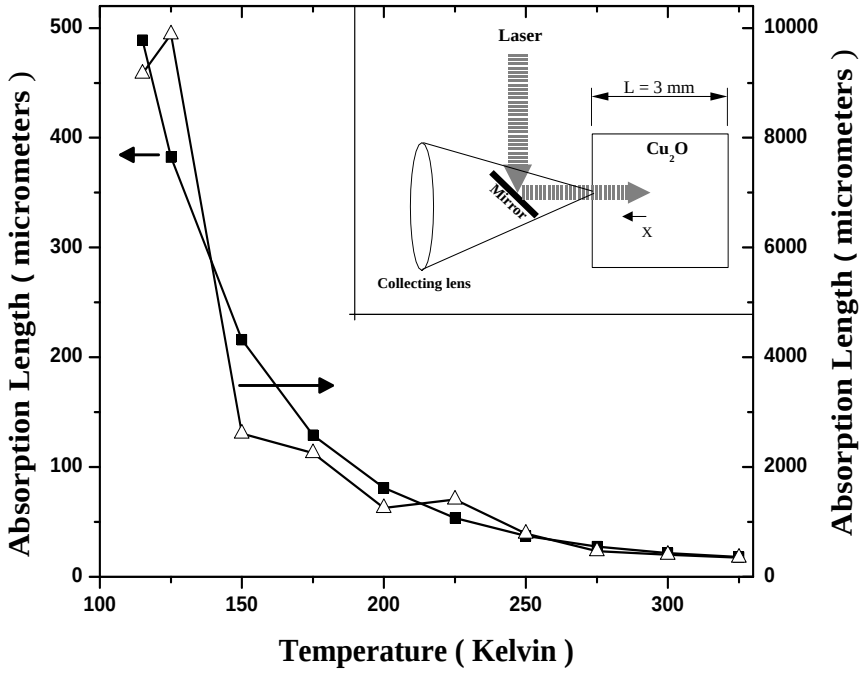

Figure 18: Absorption lengths of the input laser at 606 nm (black squares), and the exciton luminescence (open triangles) in Cu_2O versus temperature in the high temperature region. Inset: Schematics of the experimental set-up in the surface excitation.

4.3.2 Results and discussions

Fig. 19 shows the typical orthoexciton photoluminescence intensity as a function of time after a short laser pulse, at two different temperatures, 150 and 325 Kelvin, and under three different pulse energies, 2.64 nJ, 2.64/2=1.32 nJ and 2.64/6=0.44 nJ, multiplied by overall factors of 1, 2 and 6 respectively. At each temperature, the different decay times for different laser powers indicates that there is a density-dependent Auger process of excitons.

Equations (4.3) and (4.4) gave coupled rate equations including the Auger decay rate, which explained well the data at 2 Kelvin under different stresses and laser pulse energies. However, because of phonon emission and absorption, the orthoexciton and paraexciton are well coupled in the high temperature region [4.14], and therefore the coupled rate equations

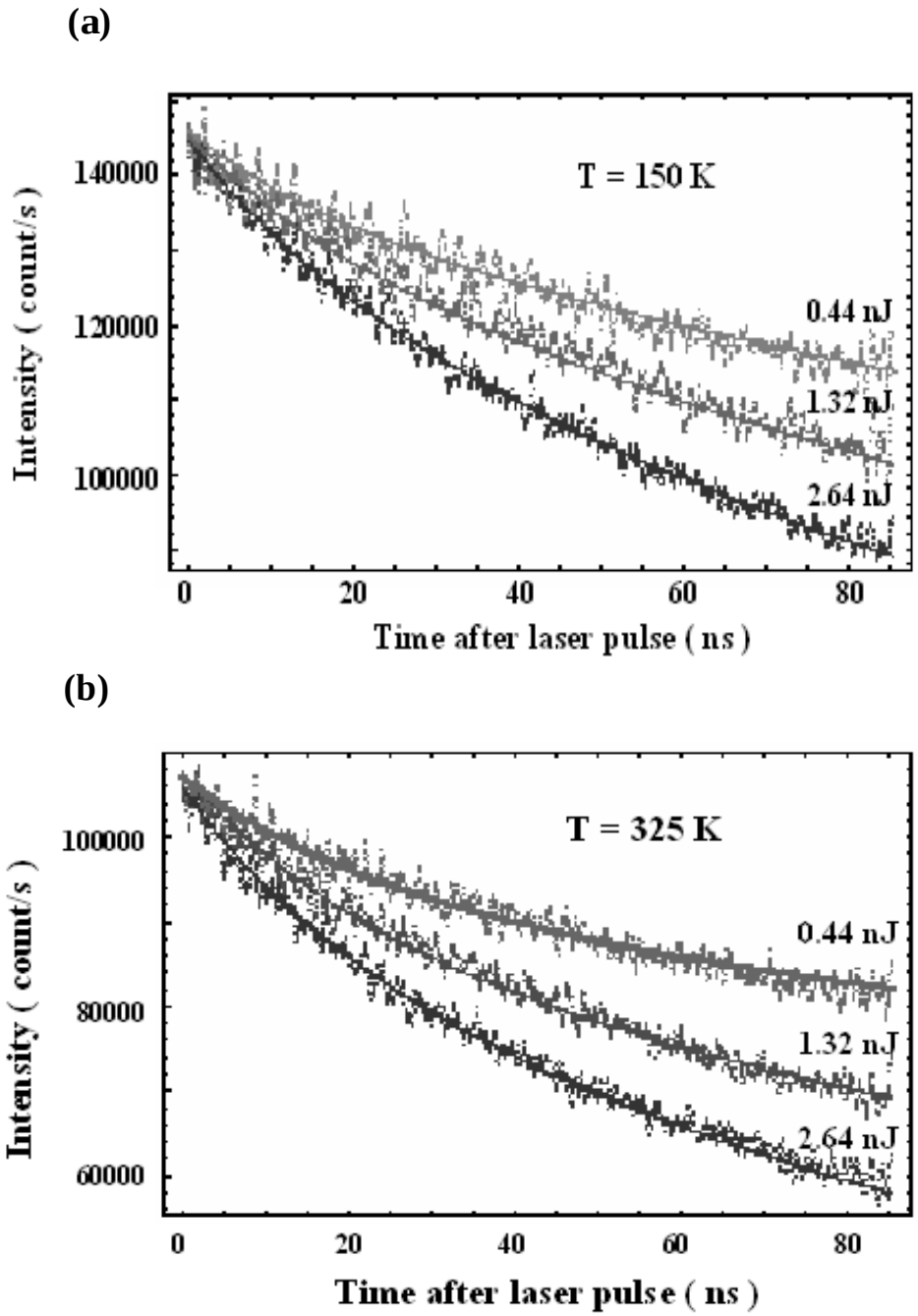

Figure 19: (a)Orthoexciton luminescence decay at T = 150 Kelvin for three different pulse energies, 2.64 nJ, 1.32 nJ and 0.44 nJ, as shown in the figure. Dots: Phonon-assisted orthoexciton luminescence intensity as a function of time after a short laser pulse. Solid lines: fit to the coupled rate equations discussed in the text. (b)Orthoexciton luminescence decay, as in (a), but at T = 325 Kelvin.

must be modified to the following:

$$\frac{dn_o}{dt} = -\frac{n_o}{\tau_{o-p}} - A_o n_o^2 + \frac{3}{8}(A_o n_o^2 + A_p n_p^2) - \frac{n_o}{\tau_o} + \frac{n_p}{\tau_{p-o}} \quad , \tag{4.7}$$

$$\frac{dn_p}{dt} = \frac{n_o}{\tau_{o-p}} - A_p n_p^2 + \frac{1}{8}(A_o n_o^2 + A_p n_p^2) - \frac{n_p}{\tau_p} - \frac{n_p}{\tau_{p-o}} \quad . \tag{4.8}$$

In these equations, n is the exciton density, indies o and p mean "orthoexciton" and "paraexciton", respectively, A is the Auger decay constant, τ is the decay time or conversion time, and the index o-p and p-o means orthoexciton-paraexciton conversion and paraexciton-orthoexciton conversion, respectively. In each Auger process, two excitons collide and end up with one exciton recombining and the other exciton ionizing. Therefore, only the ionized exciton, half of the excitons participating in the Auger process, will be added back to exciton population. Because the orthoexciton is a triplet state and the paraexciton is a singlet state and spin is randomly selected in ionization, $\frac{3}{4}$ of the ionized excitons in the Auger process will be returned as orthoexcitons and $\frac{1}{4}$ of these excitons will be returned as paraexcitons. We have to consider inter-conversions between paraexcitons and orthoexcitons in the high temperature region, although only orthoexcitons are converted to paraexcitons at 2 Kelvin [4.15]. Because energy splitting between orthoexciton and paraexciton at the zone center is 12 meV, and orthoexciton and paraexciton reach thermal equilibrium rapidly at high temperature [4.9], the conversion time in the inter-conversion mechanisms has a relationship,

$$\tau_{p-o} = \tau_{o-p} \times e^{\frac{12meV}{K_B T}} \quad . \tag{4.9}$$

All the data, under ten different temperatures and three different laser pulse energies at each temperature, are well fit with the solutions of the above coupled equations, shown by the solid lines of Fig. 19 (a) and (b). The fit results imply that the Auger constant of the orthoexciton is equal to that of the paraexciton at each temperature. The results also show that the radiative lifetimes of paraexcitons and orthoexcitons are on the order of several hundred nanoseconds, and the inter-conversion time between paraexcitons and orthoexcitons is on the order of 0.1 nanosecond, which is consistent with the report from Wolfe's group

[4.9] and our previous results [4.14]. Because paraexcitons rapidly reach thermal equilibrium with orthoexcitons, in the fitting process we can assume that at all times after t = 0.1 ns,

$$n_p(t) \quad = \quad n_o(t) \times e^{\frac{12meV}{K_B T}} \quad . \tag{4.10}$$

An interesting result from the fitting is that the Auger constant of excitons linearly increases with temperature in the region from 115 Kelvin to 325 Kelvin, as shown in Fig. 20. Several groups have studied the temperature dependence of the Auger decay process in Cu_2O, but the highest temperature they used is 77 Kelvin [4.9, 4.16]. Their works show that the Auger constant of orthoexcitons is almost independent of temperature. The above two results are not inconsistent, which is explained in detail in next section.

4.3.3 Phonon-assisted mechanism

Kavoulakis and Baym [4.16] introduced a model based on Fermi's Golden rule and **k·p** theory to understand the Auger recombination process with an optical phonon-assisted mechanism at low temperature. We follow their steps, but modify it with considerations of high temperature effects and all possible phonons in an Auger process, in which two excitons with momentum $\vec{K}$ and $\vec{P}$ collide, producing one ionized electron-hole pair with momenta $\vec{k}_e$ and $\vec{k}_h$, and absorbing or emitting a phonon.

In the phonon-assisted process, $\frac{\Gamma_{Auger}}{V}$, the Auger decay rate per unit volume is a function of $\Gamma_{K,P}$ and f_K, f_P, the decay rate and distribution functions of the two excitons, respectively:

$$\frac{\Gamma_{Auger}}{V} = \frac{1}{V}\sum_{K,P} f_K f_P \Gamma_{K,P} \sim An^2 \quad , \tag{4.11}$$

Where A is Auger constant for the exciton and n is the density of the excitons.

From Fermi's Golden Rule, the decay rate of two excitons with momenta $\vec{K}$ and $\vec{P}$ is

$$\begin{aligned} \Gamma_{K,P} \quad = \quad & \frac{2\pi}{\hbar}\sum_{k_e,k_h,Q} |M|^2 (1-n_{c,k_e})(1-n_{v,k_h}) \\ & \times[(n_{ph}+1)\delta(E_K+E_P-\hbar\omega_Q-\varepsilon_{c,k_e}-\varepsilon_{v,k_h}) \\ & +n_{ph}\delta(E_K+E_P+\hbar\omega_Q-\varepsilon_{c,k_e}-\varepsilon_{v,k_h})] \quad , \end{aligned} \tag{4.12}$$

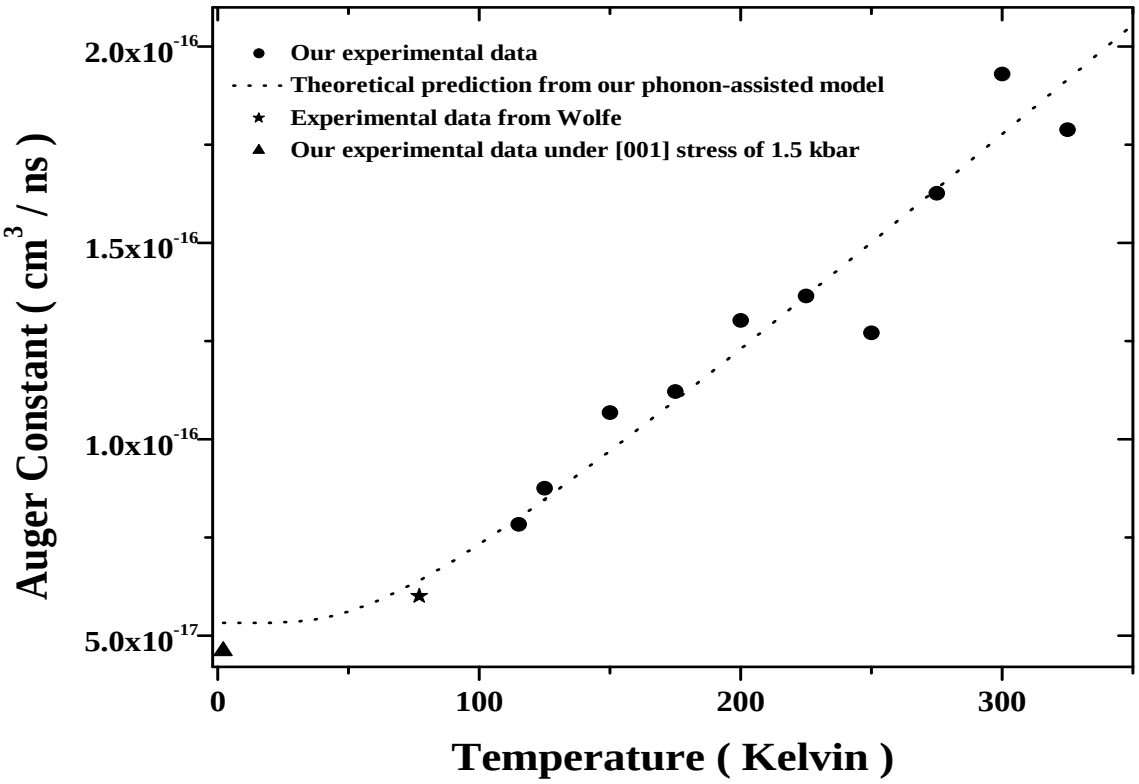

Figure 20: Auger constant of the excitons as a function of temperature in the high and low temperature region. Black dot: our experimental data in the high temperature region. Black dash dot line: result fit from the theory discussed in the text.

The first term in Eq. (4.12) is for a process emitting a phonon with momentum $\vec{Q}$, while the second term is for a phonon absorption process by absorbing a phonon with momentum $\vec{Q}$. The term $n_{ph} = 1/(e^{E_{ph}/(K_B T)} - 1)$ is the density of the phonon at temperature T, and K_B is Boltzmann's constant.

In the equations, based on **k**·**p** theory [4.16], the matrix element of an optical phonon-assisted process, $M_{optical}$, is given by the following equation,

$$M_{optical} \approx 2^2\pi\frac{e^2 a_B}{\epsilon_\infty}\frac{\hbar}{m} \times \frac{|\mathbf{P}_{v,c'}|}{(\varepsilon_{c',0} - \varepsilon_{v,0})} \times \frac{k_e a_B}{[1 + (k_e a_B)^2]^3} \times (\frac{\hbar^2 D^2_{optical}}{2V\rho E_{optical}})^{\frac{1}{2}} \frac{1}{(\varepsilon_{c,0} - \varepsilon_{c',0})} \times \delta_{\vec{k}_e + \vec{k}_h \pm \vec{Q}, \vec{K} + \vec{P}} \quad . \tag{4.13}$$

where $D_{optical}$ is the deformation potential for an optical phonon, $E_{optical}$ is the energy of the optical phonon, ε_c and $\varepsilon_{c'}$ are energies of the lowest conduction band Γ_6^+ and the only odd parity conduction band Γ_8^-, respectively, ε_v is the energy of the valence band Γ_7^+, $P_{v,c'}$ is the matrix element of the momentum operator between the conduction and valence band at zone center, ρ is the mass density of Cu_2O, ϵ_∞ is the dielectric constant, and a_B is the exciton Bohr radius.

In an acoustic phonon-assisted process, $k_{necessary}$ the necessary momentum for an acoustic phonon is to satisfy energy and momentum conservation between the lowest conduction band and the only odd parity conduction band, that is to say, $k_{necessary} = (\varepsilon_c - \varepsilon_{c'})/(\hbar\nu)$ = 1.515×10^9 cm^{-1}. In the discussion, ν is the acoustic phonon speed. However, k_{max}, the maximum momentum of an acoustic phonon, is equal to $\frac{\pi}{a_L}$ = 7.375×10^7 cm^{-1} because it is restricted to be in the first Brillouin zone, where a_L is the lattice constant of Cu_2O. Therefore there is no possible process assisted by acoustic phonons and from now on all discussions will only consider the process assisted by the optical phonons.

As mentioned by Kavoulakis [4.16], E_K, E_{k_e}, and E_{k_h}, the energy of an exciton with momentum $\vec{K}$, the energy of an electron in the conduction band, and the energy of a hole in the valence band, respectively, are given by [4.16],

$$E_K = E_{gap} + \frac{\hbar^2 K^2}{2m_{exciton}} \tag{4.14}$$

$$E_{k_e} = E_{gap} + \frac{\hbar^2 k_e^2}{2m_e} \tag{4.15}$$

$$E_{k_h} = \frac{\hbar^2 k_h^2}{2m_h} \tag{4.16}$$

Because the momenta of excitons, $\vec{K}$ and $\vec{P}$, are determined by exciton thermal motion, we can make a reasonable assumption [4.16],

$$\vec{K}, \vec{P} \ll \vec{k}_e, \vec{k}_h \quad . \tag{4.17}$$

By substituting Eq. (4.13) through (4.17) into Eq. (4.12), $\Gamma_{K,P}$ the decay rate of two excitons in the phonon-assisted process is equal to

$$\Gamma_{K,P}^{phonon-assisted} = \frac{2^7\pi^5 e^4 a_B^2 \hbar}{\epsilon_\infty^2 V m^2 E_{optical}\rho} \times \frac{D_{optical}^2}{(\varepsilon_{c,0} - \varepsilon_{c',0})^2} \times \frac{|\mathbf{P}_{c',v}|^2}{(\varepsilon_{c',0} - \varepsilon_{v,0})^2} \times \frac{(k_e a_B)^2}{[1 + (k_e a_B)^2]^6} \times [1 + \frac{2}{e^{E_{optical}/k_B T} - 1}] \quad , \tag{4.18}$$

Parameter	Value	References
ϵ_∞	6.46	4.15
ρ	6 gram/cm^3	4.19
ν	4.5×10^5 cm/second	4.18
m_e	m_e^0	4.20
m_h	$0.7m_e^0$	4.20
m_e^0	9.1×10^{28} gram	4.19
a_B	7×10^{-8} cm	4.18
a_L	4.26×10^{-8} cm	4.18
$D_{\Gamma_{12}^-}$	4.6×10^7 eV/cm	this work
$D_{\Gamma_{15}^-}$	4.8×10^7 eV/cm	this work
$\lvert\mathbf{P}_{c',v}\rvert/\hbar$	0.07 Å^{-1}	this work
$\varepsilon_{c'}-\varepsilon_c$	0.449 eV	4.15
$\varepsilon_{c'}-\varepsilon_v$	2.622 eV	4.15
Γ_{12}^-	13.8 meV	4.21
Γ_{15}^-	18.7 meV	4.21

Table 12: Values of parameters used in the Auger decay rate calculation discussed in the text.

The integration is restricted to the first Brillouin zone. All constant parameters used in the calculation are listed in Table 12. The optical deformation potentials and $|\mathbf{P}_{c,v}|^2$ are estimated from fitting of experimental data.

Therefore, by substituting Eq. (4.18) into Eq. (4.11), we get $A_{phonon-assisted}$, the phonon-assisted Auger constant,

$$A_{phonon-assisted} \simeq 2.6\times10^{-17}\times[1+\frac{2}{e^{160/T}-1}]+2.8\times10^{-17}\times[1+\frac{2}{e^{217/T}-1}]. \quad (4.19)$$

Only two optical phonons, Γ_{12}^- and Γ_{15}^-, make important contributions.

We plot Eq. (4.19), a theoretical prediction of the exciton Auger constant assisted by all possible phonons from 2 to 325 Kelvin, and our experimental Auger recombination constants in the high temperature region (115 $\sim$ 325 Kelvin) in Fig. 20, which shows

that our experimental data in the high temperature region can be well fit by the theoretical prediction of the Auger constant from the phonon-assisted mechanism.

At low temperatures, where the phonon energy is much smaller than the thermal energy k_BT, n_{ph} the density of the phonon is much less than 1. Therefore only the phonon emission process is important and phonon absorption process is negligible. We can approximate:

$$\begin{aligned}\Gamma_{K,P} &= \frac{2\pi}{\hbar}\sum_{k_e,k_h,Q}|M_{ph}^2|(1-n_{c,k_e})(1-n_{v,k_h}) \\ &\times \quad \delta(E_K+E_P-\hbar\omega_Q-\varepsilon_{c,k_e}-\varepsilon_{v,k_h}) \qquad (Low \quad T)\end{aligned} \tag{4.20}$$

After substituting Eq. (4.20) into Eq. (4.11), we find that the Auger decay constant is weakly dependent on temperature when the temperature is lower than 77 Kelvin, which is shown in Fig. 20 and also consistent with the reports from Warren *et al.* [4.9]and Kavoulakis *et al.* [4.9, 4.16].

Therefore, we can explicitly state our conclusion on the temperature dependence of the Auger recombination constant of excitons as the following: the Auger constant is weakly dependent on temperature when the temperature is below 77 Kelvin, and linearly increases with temperature in the high temperature region. To verify our model, we make two comparisons. The first comparison is between a reported Auger constant from Wolfe's group [4.9] and our theoretical prediction at 77 Kelvin, which are consistent with each other, though our theoretical prediction is about 7 percent larger, as shown in Fig. 21. The other comparison is made between the experimental data and our theoretical model at 2 Kelvin. Our theoretical result indicates that the Auger constant does not continuously decrease to zero at zero stress at 2 Kelvin, but becomes a constant, 5.318×10^{-17} cm^3/ns, which is comparable to the experimental data at 1.5 kbar at the same temperature reported in the previous work [4.14], as shown in Fig. 21 also. The comparison implies several things. First, the Auger constant has a negligible stress dependence when the stress is lower than 1.5 kbar. Second, the two results are consistent, although the theoretical prediction from our phonon-assisted mechanism is about 16 percent larger than the extrapolated data. Third, the surface doesn't play an important role in the Auger effect. Since the 7 to 16 percent discrepancy between experimental data and theoretical prediction is in the acceptable experimental error range,

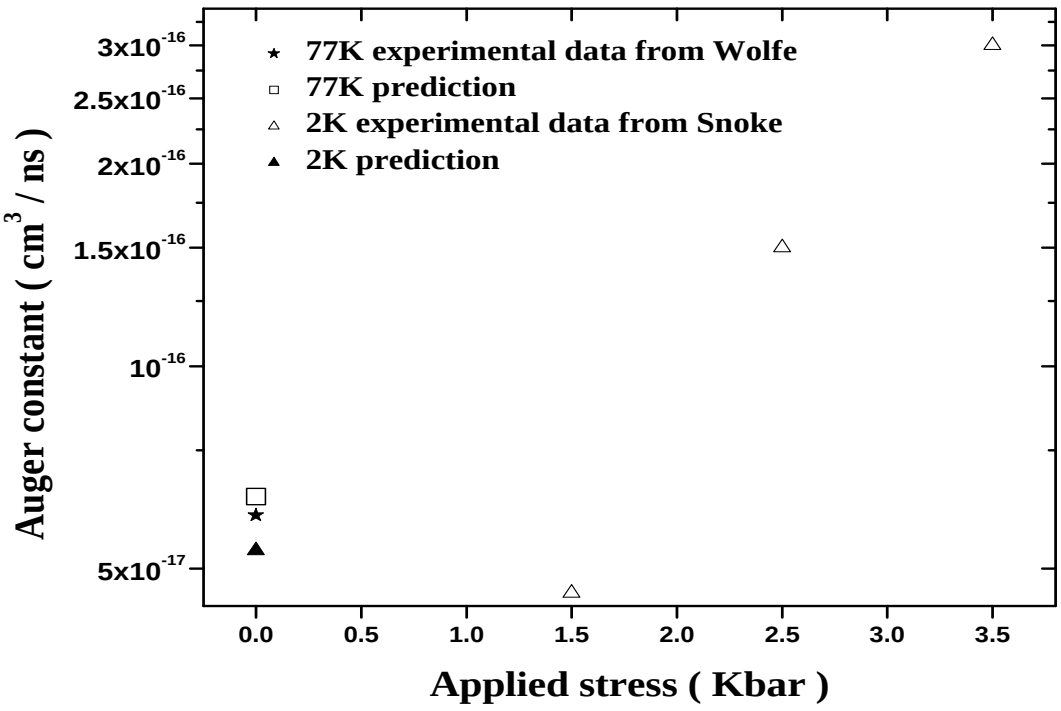

Figure 21: Stress and temperature dependence of the orthoexciton Auger constant. Open triangles: data reported by Snoke *et al.* [4.14] at 2 Kelvin for three different stresses, 1.5, 2.5 and 3.5 kbar. Black stars: data reported by Wolfe *et al.* [4.9] with negligible stress at 77 Kelvin. Black triangle and open square are predictions from our theoretical model with negligible stress at 2 Kelvin and 77 Kelvin, respectively.

our modified phonon-assisted mechanism may be a good model for the Auger recombination rate of excitons in both low and high temperature regions.

4.4 CONCLUSIONS

We have seen that spin flip by phonon emission is the dominant mechanism for conversion of orthoexcitons to paraexcitons in Cu_2O. Spin flip by phonon emission may also occur in many other materials, but it has not been well studied. With the growing interest in "spintronics", this mechanism deserves further attention.

We found that the Auger recombination process strongly depends on the applied stress when the stress is larger than 1.5 Kbar, and has a temperature dependence which can be understood by our modified phonon-assisted mechanism. The Auger recombination constant is weakly dependent on temperature in the low temperature region and linearly increases with temperature at high temperatures. The stress and temperature dependence of the rate of Auger recombination of excitons in Cu_2O helps to explain some apparent discrepancies in the literature. However, the results of Jolk *et. al* [4.8] are in disagreement with our theoretically predicted result at zero stress and also with the experimental measurements of Wolfe *et al.* [4.7, 4.9].

5.0 SEARCH FOR BEC OF PARAEXCITONS IN CUPROUS OXIDE WITH RESONANT TWO-PHOTON EXCITATION

Most studies [5.1, 5.2, 5.3] on BEC of excitons in Cu_2O have concentrated on the higher-lying orthoexciton state since it can be easily created by a single-photon phonon-assisted absorption. In the single-photon phonon-assisted excitation process, however, a hot optical phonon is created which can heat the exciton gas, thereby deterring BEC. In the past few years, several groups [5.4, 5.5, 5.6, 5.7, 5.8, 5.9] have tried resonant two-photon excitation of the orthoexciton state. A major advantage is that the scattered two-photon laser light will not damage imaging systems because it is far away from the exciton luminescence lines, which allows a measurement during the laser pulse. It is also expected that two colliding pulses in opposite directions will create excitons directly in the $\mathbf{k} = 0$ state, where a condensate should appear, instead of in a state with finite momentum.

Resonant excitation of orthoexcitons still has the problem that the orthoexcitons will convert down into paraexcitons by a phonon emission [5.10], and the emitted phonon will cause a local heating, which may prevent BEC. Our present work aims to solve the above problem with a resonant two-photon excitation of the yellow paraexciton state, because it is the lowest exciton state and primarily only decays by direct single-photon emission. We create excitons in a harmonic potential trap made with an external stressor [5.1, 5.3, 5.11], which confines excitons in a defined volume and changes the local symmetry of Cu_2O from O_h to D_{4h}. One problem which becomes more important in the potential trap is the Auger recombination process, which happens when two excitons collide and one exciton ionizes, taking the energy of the other exciton that recombined. Therefore the Auger process not only gives a severe limit in exciton density but also heats up the exciton gas, which will tend to prevent BEC. The Auger recombination rate increases roughly as the square of the stress,

with smaller Auger recombination at the stress lower than 1.5 kbar [5.1, 5.12], as discussed in the previous chapter. However, because the phonon-assisted orthoexciton and direct paraexciton luminescence lines are separated at high stress but substantially overlapped at low stress [5.11], we have to use high stress to separate the luminescence lines. In this chapter, the inhomogeneous applied stress is kept at 1.9 kbar, a trade-off point which is good enough to spectrally separate the paraexciton line and provides a relatively small Auger process.

In this chapter, we present experimental results for two experimental configurations, with one IR laser beam and with two colliding IR laser pulses. We demonstrate the resonant creation of paraexcitons under two-photon excitations with several strong evidences. Then we propose a model of the excitation mechanism for the paraexciton and orthoexciton in the two-photon excitations, based on our study on selection rules and polarization dependence of the 1s-"yellow" excitons from group theory, which are shown in Chapter 3.

5.1 EXPERIMENTAL SET-UP

As shown in Fig. 22, in one-beam experiments the Cu_2O sample, a $4.9 \times 3 \times 3$ mm bulk crystal, is oriented as follows: one [110] surface is illuminated by an IR laser beam and the exciton luminescence is collected from the perpendicular $[\bar{1}10]$ surface by an imaging lens. We can also create excitons by splitting the IR laser beam into two counter-propagating parts which meet in the Cu_2O sample at the same time from opposite [110] directions, with a controlled time delay. The repetition rate, the duration and the spectral width of the IR laser are 250 KHz, 200 fs and 20 nm, respectively. In order to compare, we also do experiments under single-photon excitation with a cavity-dumped 3.8 MHz and 50 ps red dye-laser tuned to the exciton resonance under the same crystal orientation.

Moreover, we also created excitons by a resonant two-photon excitation with a home-built infrared OPA-OPG laser which is specified in Section (2.3). However, because the PMT detects at most one photon per laser pulse and the repetition rate of the home-built OPG-OPA is too low, 50Hz, the necessary time to get a reasonable signal-to-noise ratio will be too long. Therefore most of the experiments of two-photon excitations are done with the high repetition rate OPA laser system.

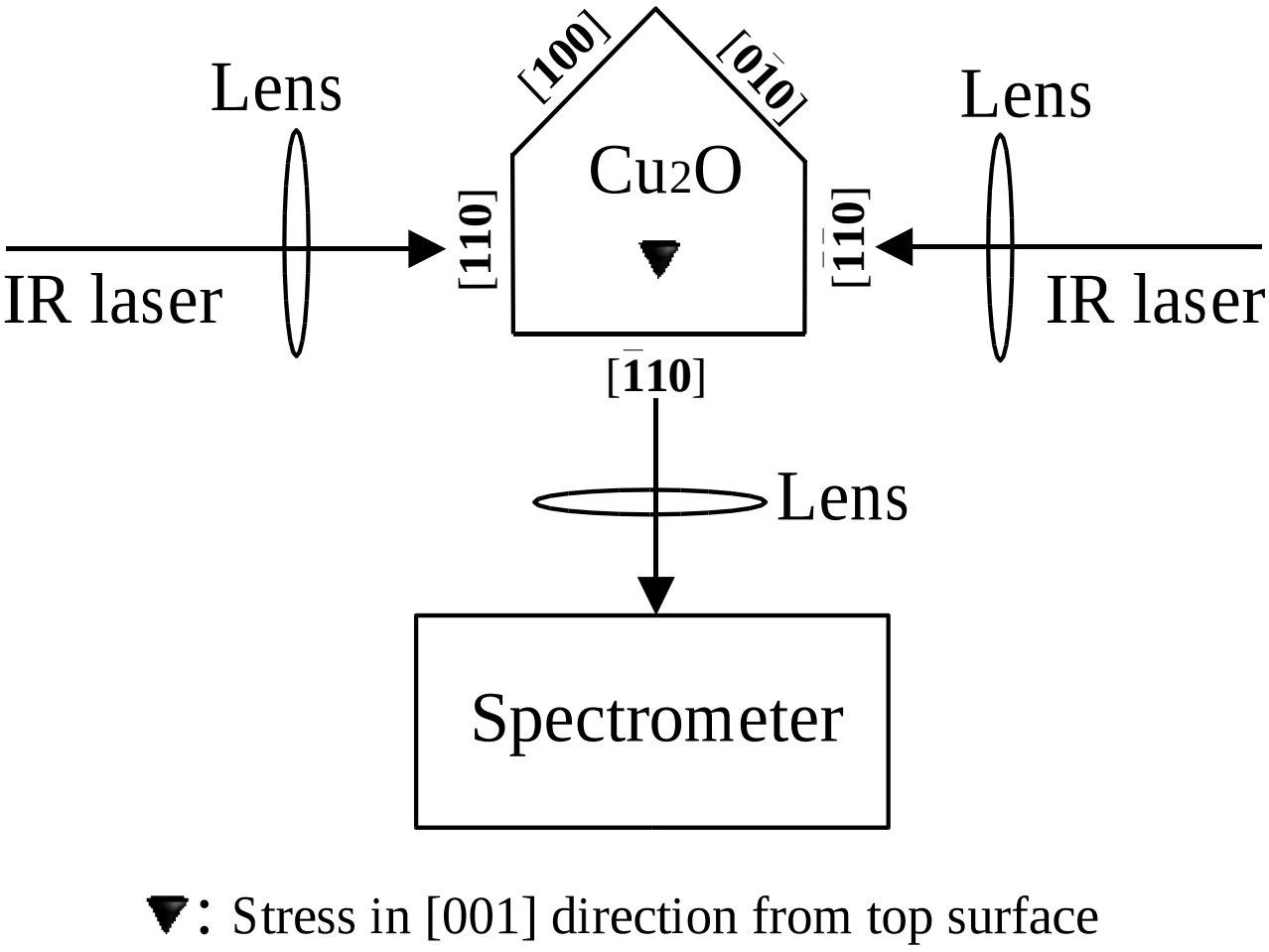

Figure 22: Schematic of the experimental set-up in this work.

Excitons are confined by a harmonic potential trap made with a 6 mm radius curved glass stressor applied along the [001] axis from the top surface of the Cu_2O crystal. Under the [001] stress, we find strong paraexciton signal, although Naka and Nagasawa [5.4] reported that paraexcitons were too weak to be detected. The main reason is that our femto-second laser system has much greater instantaneous intensity than their nano-second laser. Moreover, the exciton luminescence is collected from a direction perpendicular to the incident laser beam in this work, which has several advantages over their forward scattering geometry [5.4]. For example, the second harmonic scattering of the incident infrared laser light does not mix with the exciton luminescence.

5.2 ONE-BEAM, TWO-PHOTON EXCITATION

5.2.1 Two-photon or three-photon process?

When we create excitons with an IR laser, the first question which arises is how we can say it is not a three-photon or four-photon excitation, but a two-photon excitation. One way to answer this question is from the dependence of the exciton luminescence intensity on the IR laser power, that is to say, the excitation is a n-photon process if the intensity of exciton luminescence is proportional to (laser-power)^n. We performed a series of experiments for a broad wavelength range of IR lasers, with an inhomogeneous stress of 1.9 kbar along the [001] axis and the paraexciton line position at 614.1 nm [5.1]. As shown in Fig. 23, our experimental results indicate that the excitation is a two-photon process when the IR laser is at the paraexciton resonant position, and it is a three-photon process under off-resonant IR laser, for example at 1240 nm. All experiments in the following discussions are under resonant two-photon excitation of the paraexciton state. We note that even at this wavelength, the three-photon process will be responsible for about 25% of the total exciton creation at the highest laser powers we use, and it will dominate at high excitation power, which may also create another barrier to BEC.

5.2.2 Strong evidence for resonant paraexciton excitations

With an IR laser tuned to one half the paraexciton ground-state energy, several experimental results convince us that we directly create paraexcitons, and orthoexcitons primarily come from the excitonic Auger process. The first strong evidence is shown in Fig. 24, the time-integrated luminescence intensity as a function of IR laser power from 55 mW to 3 mW. Under 1.9 kbar stress along the [001] direction, the direct paraexciton line is at 614.1 nm. Although paraexcitons primarily only decay by single-photon emission, there are two emission lines for orthoexcitons, as shown in Fig. 24, the direct orthoexciton luminescence line at 611.7 nm, which corresponds to emission of a single photon, and phonon-assisted orthoexciton luminescence line at 615.7 nm, which corresponds to emission of a single photon and a 13.8 meV Γ_{12}^{-} optical phonon. There is only paraexciton luminescence when the laser power is very

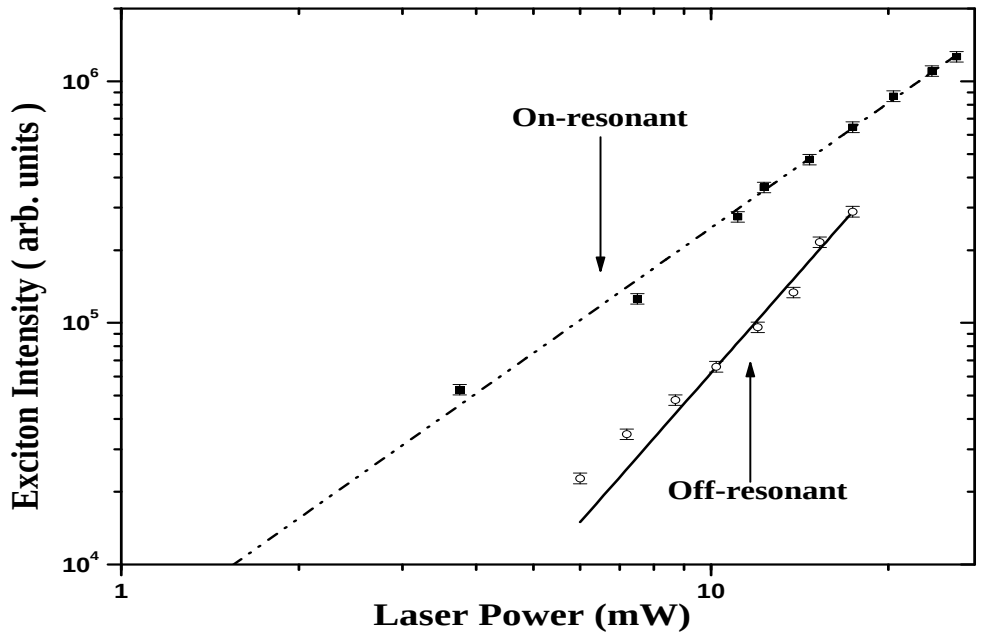

Figure 23: When the IR laser is at 1228 nm, resonant with the paraexciton state, integrated exciton luminescence intensity (black squares in the figure) can be best fit to $P^{1.7\pm0.1}$ (black dashed line), where P is the input laser power. This is consistent with a two-photon process within the experimental error. If the laser is off-resonant, at 1240 nm, the integrated exciton luminescence intensity (black open circles) can be best fit to $P^{2.8\pm0.2}$ (black solid line in the figure), consistent with a three-photon process.

low, indicating that the resonant IR laser creates the paraexciton directly. Orthoexcitons start to appear at higher laser power, around 5 mW as seen in Fig. 24, and become stronger and stronger relative to the paraexcitons with increasing the laser power, which implies that orthoexcitons are created not directly by the laser, but by a density-dependent process from paraexcitons.

A second evidence is found in time-resolved paraexciton luminescence data. Fig. 25 shows paraexciton luminescence intensity as a function of time after laser pulses in two different pulse-laser excitations. In one case, two-photon excitation resonant with the paraexciton state is used, and in the second case, single-photon excitation tuned to the bottom of the orthoexciton phonon-assisted absorption is used. The average powers of the IR laser and

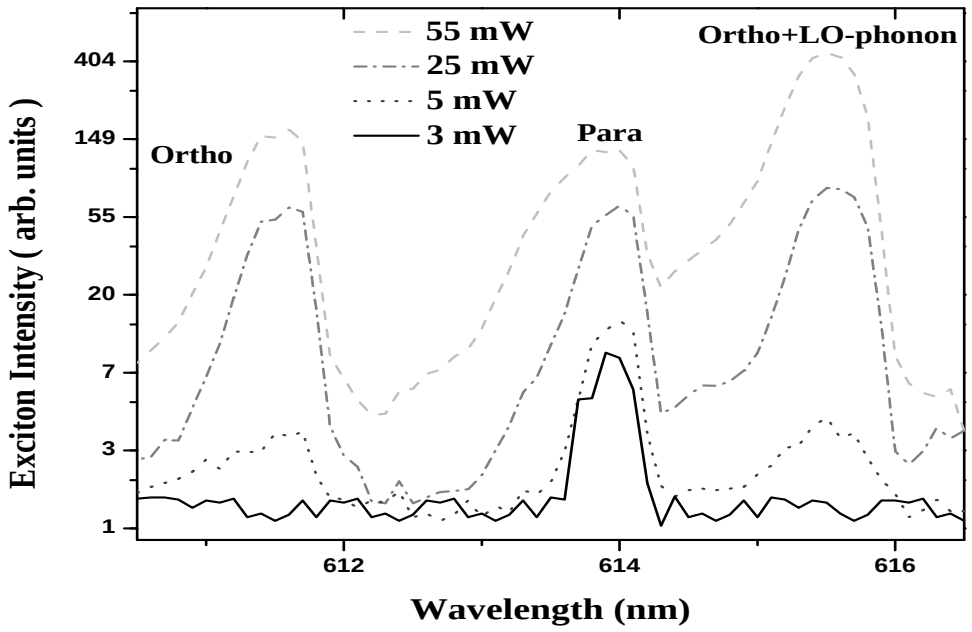

Figure 24: Time-integrated exciton luminescence intensity in the Cu_2O sample for several different laser powers, at 1.6 Kelvin and under 1.9 kbar stress along the [001] axis, with two-photon one-beam excitation resonant with the paraexciton state.

the red laser used in the excitations were adjusted to get the same total integrated exciton luminescence intensity. These average powers were 70 mW and 0.9 mW, respectively. There are several similarities between the two cases. The paraexciton luminescence intensity in both cases reaches a steady-state value long after the laser pulses which indicates lifetimes of paraexcitons longer than the 260 ns period between the laser pulses, and the paraexciton luminescence intensities at time just before the laser pulses are comparable, equal to the steady-state value left from the previous laser pulse. However, in the case of resonant two-photon excitation, the paraexcitons reach maximum intensity immediately after the laser pulse, consistent with the paraexcitons being created directly by the laser. In the case of single-photon excitation of orthoexcitons, paraexcitons do not appear right after the laser pulse, but are slowly created in a time interval of more than 10 ns from a process which is known to be phonon-assisted orthoexciton down-conversion [5.1]. The rise time of 10 ns

is longer than the reported orthoexciton-paraexciton conversion time of 4 ns, [5.1] presumably because the paraexcitons must also cool down before they appear in the single-photon luminescence, which involves only states near the band bottom.

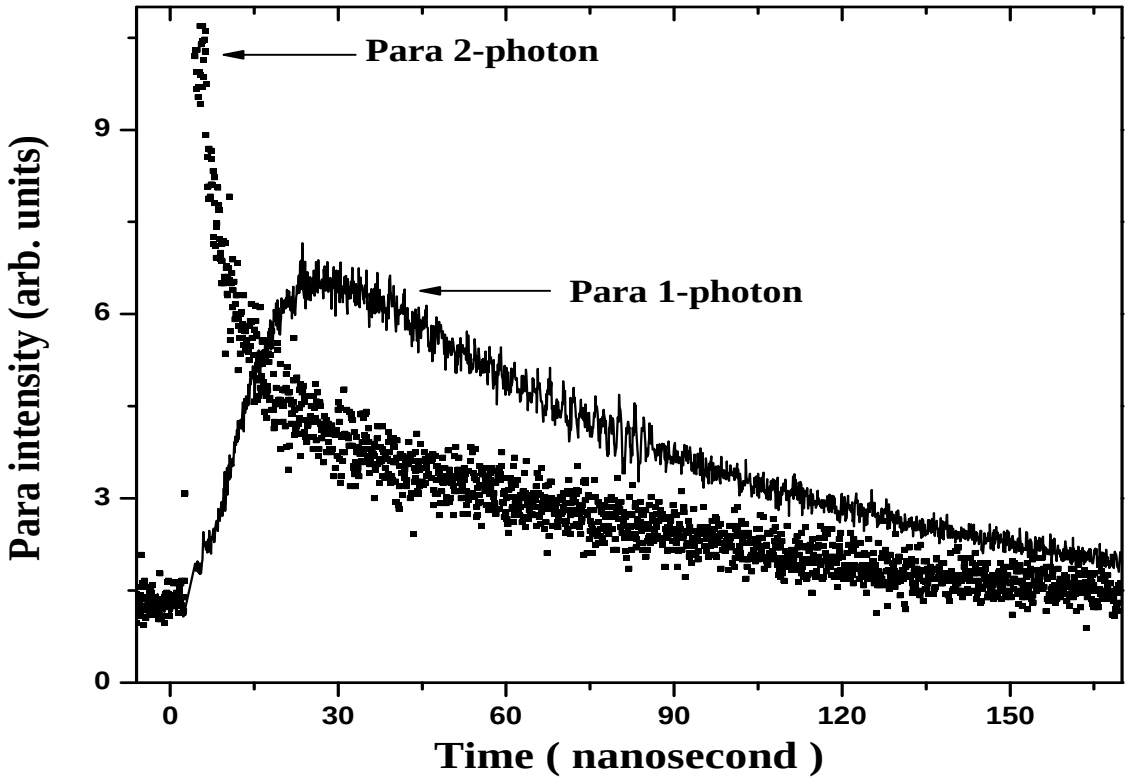

Figure 25: Paraexciton luminescence as a function of the time after the laser pulse, for a Cu_2O sample at 1.6 Kelvin and under 1.9 kbar stress along the [001] axis. Black dots: two-photon excitation resonant with the paraexciton state. Black solid line: single-photon excitation tuned to the bottom of the orthoexciton phonon-assisted absorption. The power of the red and the IR laser were adjusted to give the same total integrated exciton luminescence intensity.

Another strong evidence is the power dependence of time-resolved data for both paraexcitons and orthoexcitons under the two-photon excitation resonant with the paraexciton state. Fig. 26 shows two important things. First, paraexcitons appear right after the laser pulse, but orthoexcitons are created slowly after a few nanoseconds. Second, orthoexcitons are created more slowly at lower IR laser power, which again indicates a density-dependent

process for the creation of orthoexcitons.

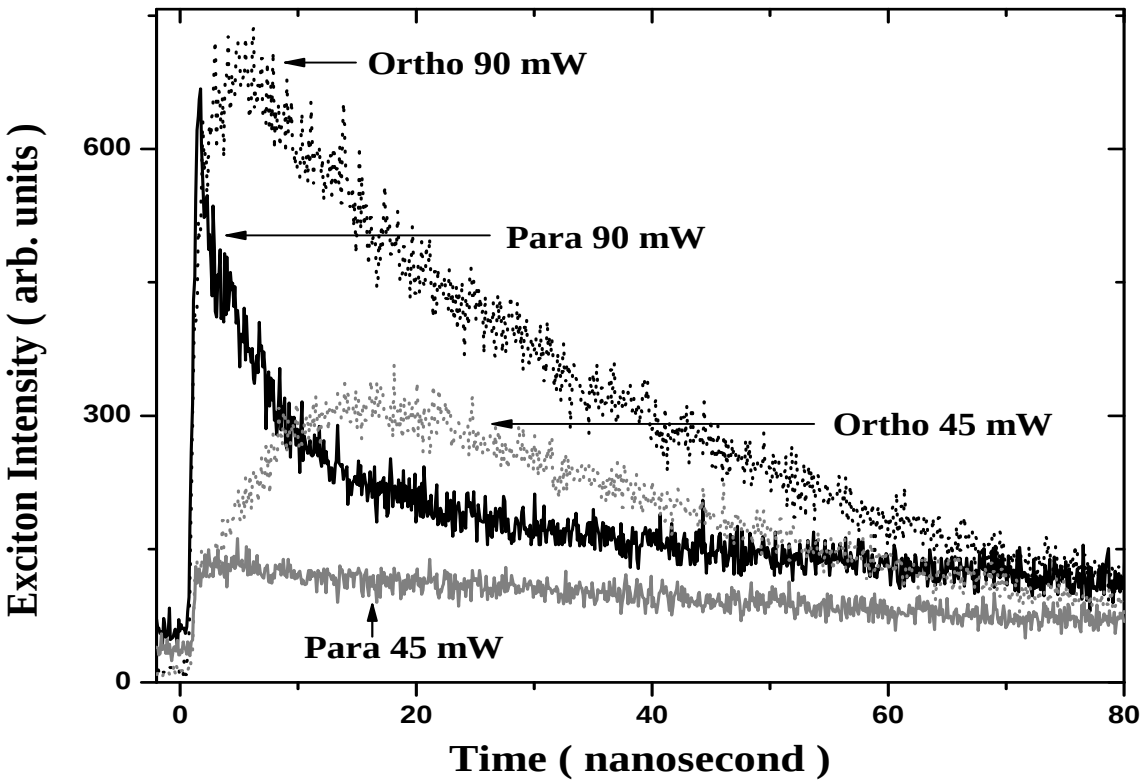

Figure 26: Time-resolved paraexciton and orthoexciton luminescence in the Cu_2O sample for two different laser powers, at 1.6 Kelvin and under 1.9 kbar stress along the [001] axis, with two-photon excitation resonant with the paraexciton state. The black dots and black solid line are the orthoexciton and paraexciton luminescence intensity at laser power of 90 mW, respectively, and the gray dots and gray solid line are the orthoexciton and paraexciton luminescence intensity at laser power of 45 mW, respectively.

All the above results lead us to a model in which paraexcitons are created directly by IR laser pulses resonant with the paraexciton state, then paraexcitons convert to orthoexcitons through a density-dependent process which is the well-known excitonic Auger process [5.1, 5.3, 5.12]. In each Auger process, two excitons collide and end up with one exciton recombining and the other exciton ionizing. Because the orthoexciton is a triplet state and the paraexciton is a singlet state, and spin is randomly selected in ionization, 75 percent

of the ionized excitons in the Auger process will be returned as orthoexcitons and 25 percent of these excitons will be returned as paraexcitons. This implies that at high excitation power, the density of orthoexcitons will exceed that of paraexcitons after a few nanoseconds, consistent with the results in Fig. 26. The observation that the creation of orthoexcitons becomes slower at lower exciton density is consistent with the fact that the density-dependent Auger process is slower at lower exciton density. Moreover, because the radiative efficiency of orthoexcitons is much larger than that of paraexcitons, orthoexcitons seems a lot brighter than paraexcitons in Figure 26 although the number of the orthoexciton is smaller.

5.2.3 Selection rules and polarization dependence in two-photon excitations

As mentioned above, the laser pulses we used for the two-photon excitation have spectral width of around 20 nm. One would therefore expect that if the ortho and para cross sections for two-photon absorption are comparable, that we should then see a significant direct creation of orthoexcitons in addition to paraexcitons, even when the laser is tuned to the paraexciton resonance. The results discussed above indicate that primarily only paraexcitons are being created, however. Is this consistent with the selection rules? Here we take a close look at selection rules of paraexcitons and orthoexcitons in two-photon excitation.

As proven in Chapter 3 with group theory, in the Cu_2O sample under a stress along the [001] axis, both two-photon electric dipole and quadrupole transitions are allowed for paraexcitons and orthoexcitons. The comprehensive selection rules and polarization dependence for the paraexcitons and orthoexcitons under different external stresses and different exciton generation processes are listed in Tables 4 and 11. According to Table 11, when there is no external stress, the two-photon transition is only allowed for orthoexcitons with polarization dependence of $\sin^2 2\theta + \cos^4 \theta$ in the dipole transition, which is confirmed by experimental reports from Kono *et al.* [5.5] and Kubouchi *et al.* [5.13]

From the same table, for our [110] laser incident direction, if the stressed crystal is in the D_{4h} group, paraexcitons should be forbidden in both dipole and quadrupole two-photon transitions, which is consistent with the prediction of Inoue-Toyozawa [5.14], Bader-Gold [5.15] and Ablova-Bobrysheva [5.16]. θ is the angle between the polarization of the input laser

beam and the horizontal polarization. However, our experimental results in Figure 27 show that there is strong paraexciton luminescence, and the luminescence from both paraexcitons and orthoexcitons has the same intensity for the vertical and horizontal polarizations. This can be explained due to the reduction of the symmetry. That is to say, the crystal is in the D_{2h} group for most of the harmonic potential well, although the crystal is in the D_{4h} symmetry group along the axis of the stress. In the D_{2h} group, the polarization dependence of excitons in the direct dipole transition calculated from Equation (3.2) is listed in Table 11. For our [110] laser incident direction in the D_{2h} group, the paraexciton follows a polarization dependence of $(a\cos^2\theta + b\sin^2\theta)^2$, where a and b are constant factors. Therefore, if $a = b$, there is no detectable difference between the vertical and horizontal polarization. Because the circular polarization is just a combination of both the vertical and horizontal polarization, we don't expect to see any difference in the exciton photoluminescence intensity when the input laser is changed to the circular polarization from either vertical or horizontal polarization, which is well confirmed by the experimental results in Figure 27.

The orthoexcitons following the exact polarization dependence of the paraexcitons is another good evidence for our proposed model in the resonant two-photon excitation: paraexcitons are created directly by the IR laser and orthoexcitons are created indirectly through a up-conversion of the paraexcitons.

Moreover, we also note that the birefringence changes the polarization of the incident infrared laser beam and the changes are different at different positions in the harmonic potential well. In general, there is substantial polarization mixing for the whole harmonic trap.

At this point, one may ask why the paraexciton dipole and quadrupole matrix elements should dominate the creation of excitons in our two-photon excitation, since the orthoexciton transitions are allowed. One reason is that the IR laser is tuned to the resonant wavelength of the paraexciton state in this work, which gives an on-resonant two-photon excitation for paraexcitons and an off-resonant three-photon excitation for orthoexcitons. Moreover, all our experiments except Figure 27 are done with a vertically polarized IR laser, that is to say, $\theta = 90^0$ in Table 11, which means that the orthoexciton polarization dependence for our [110] laser incident direction in the D_{2h} group is $\cos^4\theta + \sin^2 2\theta = \cos^4(90^0) + \sin^2(180^0) = 0$.

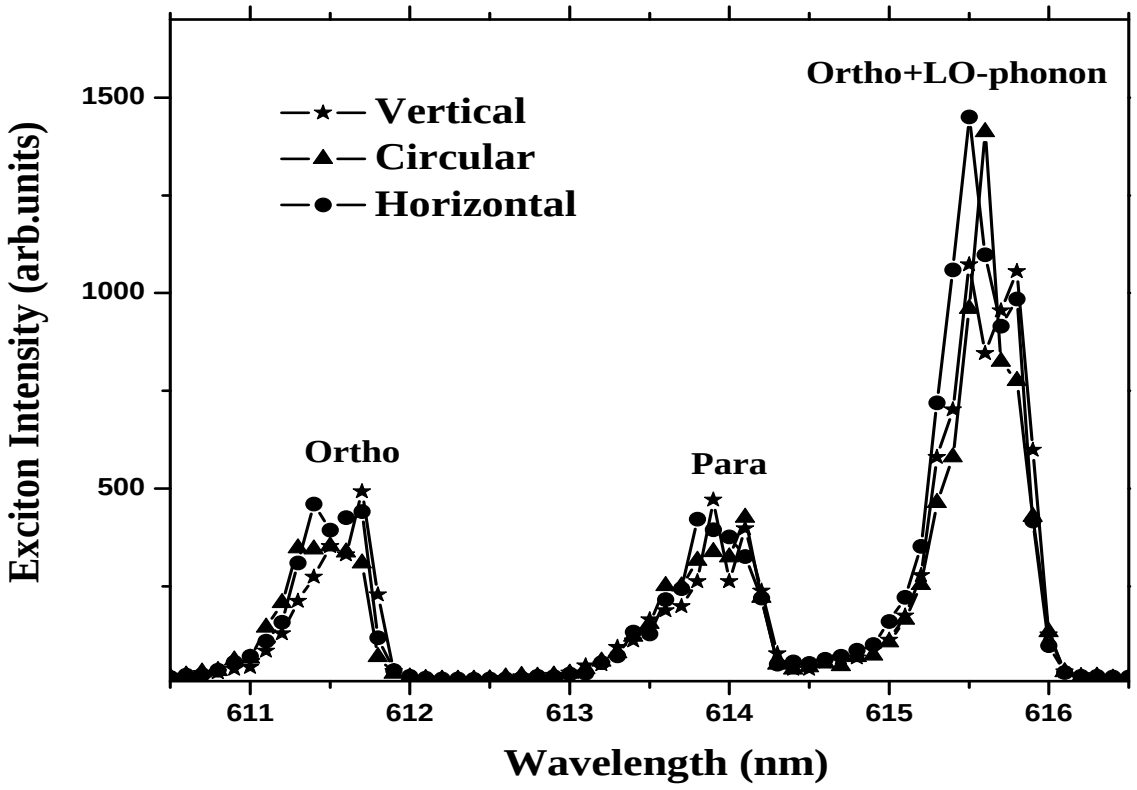

Figure 27: Polarization dependence for the total integrated paraexciton and orthoexciton luminescence intensities for a Cu_2O sample at 1.6 Kelvin under 1.9 kbar stress along the [001] axis, with two-photon excitation resonant with the paraexciton state.

Therefore, the orthoexciton dipole matrix element is forbidden for most of this work. At $\theta = 0^0$, the horizontal polarization, we would expect some orthoexcitons created directly by the IR laser, but the matrix element may be smaller.

Therefore, we can explicitly express our results as the following: confined by a harmonic potential trap created with an external stress, when an IR laser pulse tuned to one half the paraexciton ground-state energy is shining along the [110] crystalline direction of the Cu_2O sample, paraexcitons are directly created by the IR laser pulse through both the dipole and quadrupole transitions, and orthoexcitons are created primarily from the paraexciton Auger process at the early time after the laser pulse.

5.3 IS THERE BEC OF PARAEXCITONS?

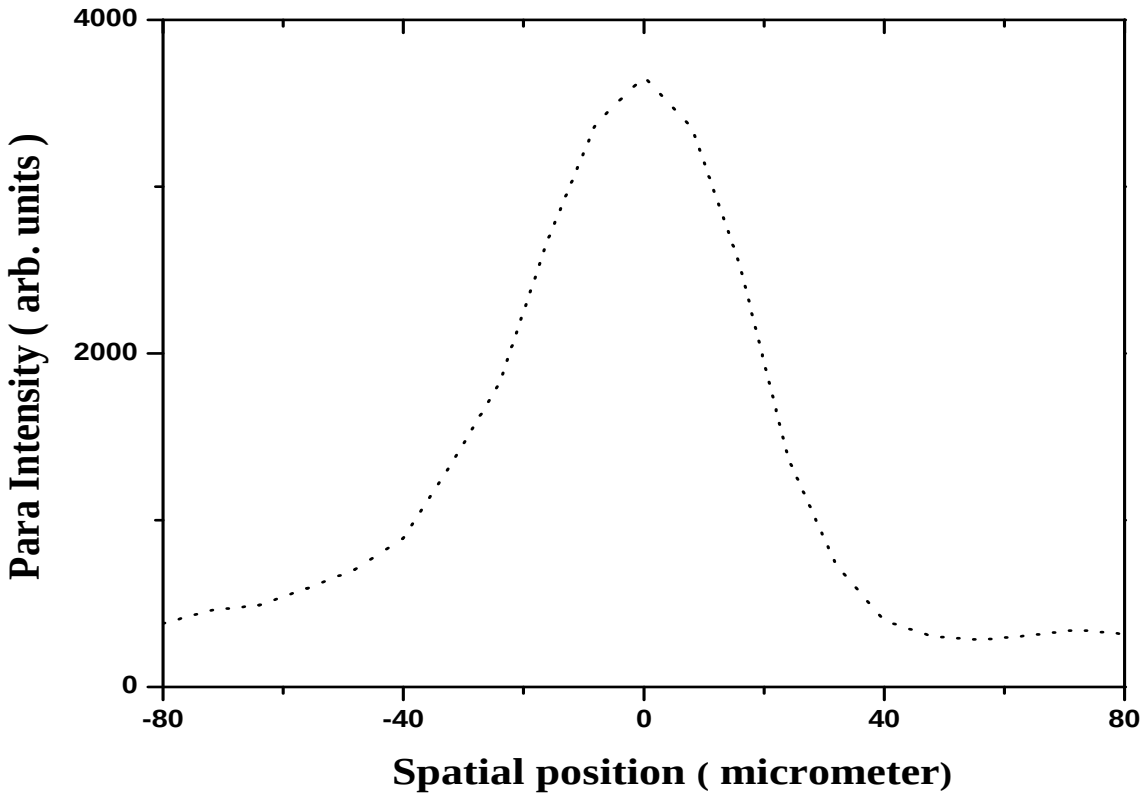

Figure 28: Spatial profile of the paraexciton luminescence in the stress-induced harmonic potential trap for the excitons, for the Cu_2O sample at 1.6 Kelvin under 1.9 kbar stress along the [001] axis, with two-photon excitations resonant with the paraexciton state.

Since we can resonantly create the paraexciton via two-photon excitation resonant with the paraexciton state, should we see BEC of the paraexcitons? Our estimate of the density of paraexcitons indicates that we should not expect to see this. Fig. 28 shows an integrated spatial profile of the paraexciton in the Cu_2O crystal at 1.6 Kelvin, which gives the paraexciton excitation volume V = $\frac{4}{3}\pi(20\mu m)^3$. As mentioned in Section 3.2, when detected by PMT, the 250 KHz resonant IR laser with average power of 70 mW creates the same exciton luminescence intensity via two-photon excitation as the 3.8 MHz dye-laser at 607.5 nm with

0.9 mW average power does via single-photon excitation. If we assume that 5% of the 0.9 mW average power is absorbed in the single-photon excitation [5.17], that one absorbed photon creates one exciton in the single-photon excitation, and that comparable luminescence intensity implies comparable exciton density, then we find the density of excitons in the two-photon excitation is

$$n = \frac{3.8MHz}{250KHz} * \frac{0.9mW * 5\%}{3.8MHz * \frac{2\pi\hbar c}{\lambda} * V} = 1.6 * 10^{16} cm^{-3}. \tag{5.1}$$

where c is the speed of light, $\frac{2\pi\hbar c}{\lambda}$ is a single photon energy in the single-photon excitation with a laser at 607.5 nm, and the ratio $\frac{3.8MHz}{250KHz}$ is the calibration of the photon-counting efficiencies in the time-correlated single photon detection for the two laser systems with different repetition rates. This corresponds to 0.06% absorption of the infrared laser light.

To calculate the critical exciton density for BEC, we have to know the exciton temperature, which can be calculated in two ways. One way is to fit high temperature tail of the paraexciton luminescence with a Bose distribution function, $\varepsilon^{1/2}/(e^{\varepsilon/(k_B T)} - 1)$, where ε is paraexciton energy. The other way is to find the full width at half maximum of the phonon-assisted luminescence line, which is equal to $3.4k_B T$ in a three-dimensional harmonic potential trap [5.1]. Our calculations from the above two ways indicate that the exciton has a minimum temperature of 7 Kelvin, which means the critical exciton density should be $5 * 10^{17} cm^{-3}$ [5.10]. Since the created paraexciton density is about thirty times less than the required density for BEC, we do not expect to establish BEC of paraexcitons even with the maximum laser power from our laser system. With higher laser power or lower temperature, however, the paraexciton critical density can be approached with resonant two-photon excitation which creates paraexcitons directly.

5.4 CREATING EXCITONS WITH TWO COLLIDING PULSES

Besides doing experiments with one-beam, two-photon excitation resonant with the paraexciton state, we can excite excitons with two colliding pulses, that is to say, split the IR laser beam into two parts and shine them into the Cu_2O sample, such that both pulses reach the exciton stress trap at the same time. In this case, the $\mathbf{k} = 0$ state is directly excited if the two

parts travel in opposite directions. Therefore, the created excitons have zero momentum, $\vec{k} = 0$, which means the ground state is directly excited, where the condensate should appear, if one photon is from each pulse.

The experimental set-up is shown in Fig. 22. In order to make the two beams meet at the same time in the Cu_2O sample, we added a two-mirror delay system controlled by a precise translation stage. Fig. 29 shows the dependence of the exciton luminescence intensity on the time delay between the two colliding pulses. A comparison between one-beam and two-beam resonant excitations with the same total laser power, 90 mW, is shown in Fig. 30. The exciton luminescence in the one-beam excitation is brighter than that of the two-beam excitation, and creation of orthoexcitons in the one-beam excitation is faster than with the two-beam excitation, which indicates more excitons are created in the one-beam excitation.

To explain this phenomenon, one must consider the dependence of the density of states on the momentum $\vec{k}$. In the case of two photons travelling in the same direction, the excitons are created in the region of the (weak) polariton mixing. Two photons travelling in opposite directions will create an exciton at $\vec{k} = 0$, where the density of states is much lower. In the case of two-beam excitation, there will also be one-beam excitation with half of the total power of the two-beam excitation. Since the exciton density in the two-photon process is proportional to the square of laser power, the one-beam excitation with half of the total power will have one fourth the efficiency. The sum of all processes in the two-beam excitation ends up being less than the total in the one-beam case.

5.5 CONCLUSION

We resonantly create paraexcitons with an IR laser beam tuned to one half the paraexciton ground-state energy. This is surprising, since it is generally assumed that the cross section for paraexciton creation is always much less than that for orthoexcitons. Our experimental results are all consistent with this result, however, including the polarization dependence and time-dependent data. The exciton creation efficiency in resonant two-photon excitation is greater for one-beam excitation than for two colliding pulses, but the colliding pulse

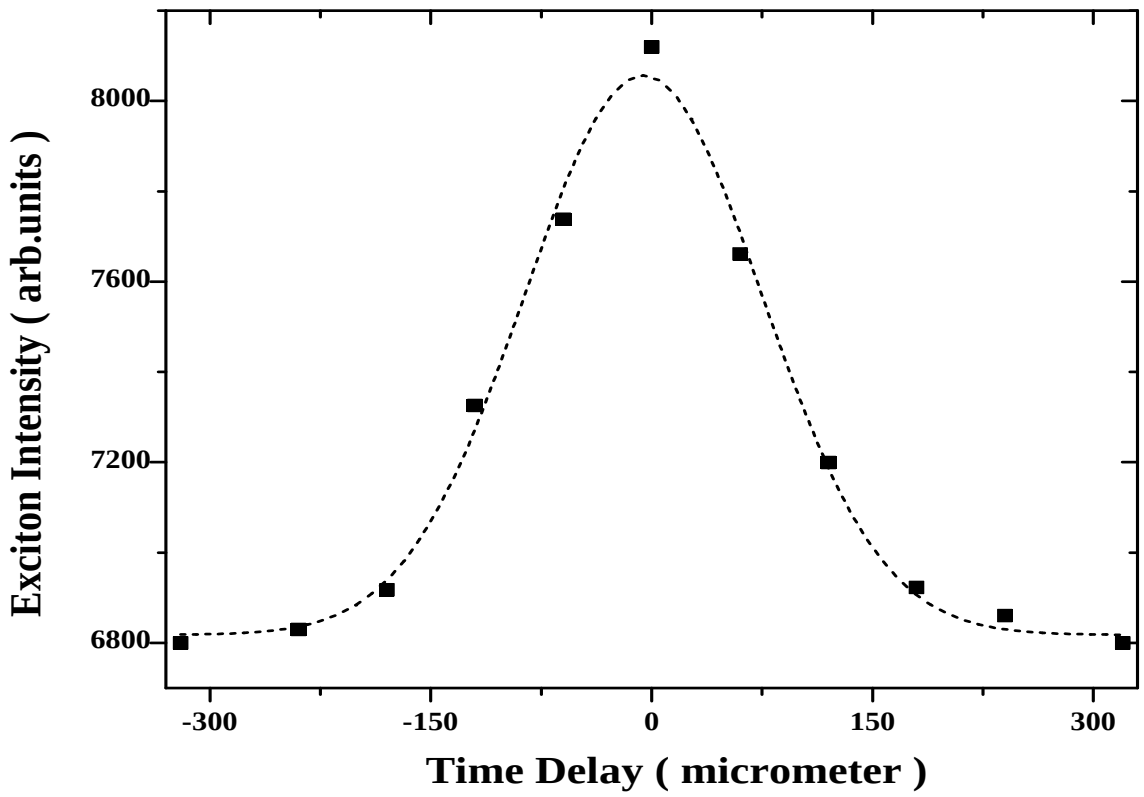

Figure 29: Total integrated exciton luminescence intensity as a function of the time delay between two laser pulses for two-beam, two-photon excitation resonant with the paraexciton state, for the Cu_2O sample at 1.6 Kelvin under 1.9 kbar stress along the [001] axis. Black squares: experimental data. Dashed line: Gaussian fit.

method may be useful for direct creation of a condensate in the ground state. At present, the paraexciton density in this work is about thirty times less than the required density for BEC of paraexcitons, but with higher laser power from stronger IR laser sources or lower temperature, the critical density can be approached with one-beam two-photon excitation resonant with the paraexciton state.

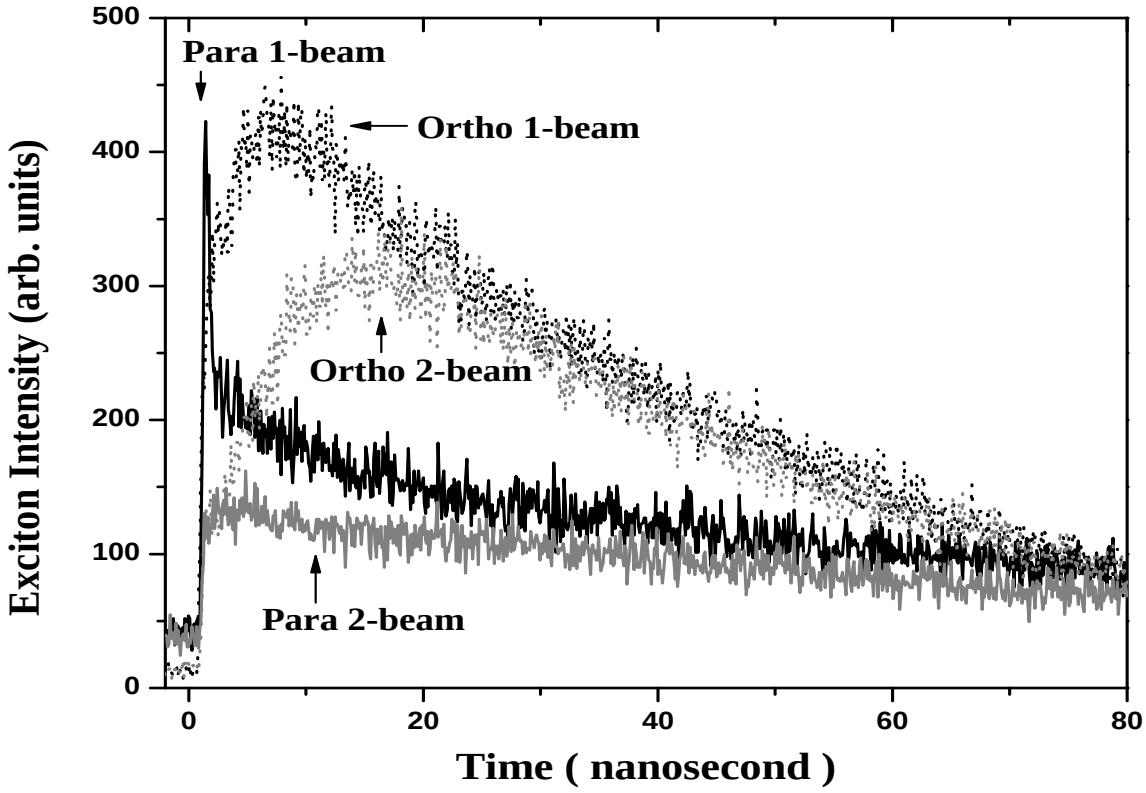

Figure 30: Exciton luminescence intensity as a function of the time after the laser pulses for one-beam and two-beam two-photon excitation resonant with the paraexciton state, with the same total laser power, for the Cu_2O sample at 1.6 Kelvin under 1.9 kbar stress along the [001] axis. The black dots and the black solid line are orthoexciton and paraexciton luminescence intensity, respectively, for one-beam excitation, and the gray dots and gray solid line are the orthoexciton and paraexciton luminescence intensity, respectively, for two-beam excitation.

6.0 BEC OF EXCITONS IN A TWO-DIMENSIONAL HARMONIC POTENTIAL TRAP

As mentioned in chapter 1, the system of indirect excitons in coupled quantum wells is an optimal system for the search of BEC of excitons. This chapter presents some promising evidence that we have observed this phase transition in the coupled quantum wells structure in a two-dimensional harmonic potential trap produced by the way mentioned in chapter 2.

6.1 TWO BIG PROBLEMS-DISORDER AND TUNNELLING

There are two big problems needed to be solved in the search for BEC of excitons in the coupled quantum well structure, disorder and the tunnelling of free charge carriers through barriers.

In the early 1990's typical GaAs quantum well structures had inhomogeneous luminescence line broadening of around 5 meV, which is a good measure of the disorder energy. If the excitons have kinetic energy less than the disorder energy, the excitons will mostly be localized in random energy minima; in other words, for disorder energy of 5 meV, at temperature less than around 50 K most of the excitons will be unable to move. If the excitons are localized, one cannot treat them as a gas to which one can apply equilibrium thermodynamics of phase transitions. If the temperature is raised, the excitons can become ionized. Since the binding energy of excitons in GaAs quantum wells ranges from 5-10 meV, depending on the exact structure [6.1], a substantial fraction of the excitons will be ionized if k_BT is large compared to a disorder energy of 5 meV. Also, the density which is needed for BEC increases with increasing T, so that raising the temperature of the excitons may

mean that the density needed for BEC reaches the range at which the excitons dissociate due to collisions [6.2].

The quality of GaAs quantum well structures, however, has been steadily improving. One approach which substantially decreases the effect of disorder, and therefore increases the mobility, is to use wide quantum wells. Many previous studies have used narrow quantum wells of 50-60 ÅGaAs, because the binding energy of the excitons is increased for narrower wells. The mobility in quantum wells is approximately proportional to the well width to the sixth power [6.3], however, which strongly favors wider wells. Another factor which favors wider quantum wells is the effect of well width on the interactions between the excitons. As shown by Lozovik and Berman [6.4], the interactions between excitons become completely repulsive for total electron-hole separation of three times the two-dimensional excitonic Bohr radius, which in GaAs is approximately 65 Å. For these reasons, for this study we have used a structure with two 100 ÅGaAs quantum wells, separated by a thin 40 Å$Al_{0.3}Ga_{0.7}As$ barrier.

A second hurdle to overcome is the effect of a current of free charge carriers passing through the quantum wells. Because we apply voltage normal to the wells, there is always a current due to drift of carriers from the surrounding, doped substrate, which tunnel through the outer barriers confining the electrons and holes in the quantum wells. These carriers will tend to screen out the electron-hole Coulomb interaction, thus reducing the binding energy, and they will decrease the mobility of the excitons by random scattering with free carriers. In previous work [6.5, 6.6], the current of free carriers played a major role in the explanation [6.7, 6.8] of the mysterious effect of luminescence rings. To reduce the current through our structure, we employ four strategies, as shown in Fig. 31. First, we use the highest possible barriers, $Al_{0.45}Ga_{0.55}As$. Second, we introduce into the barriers a super-lattice of 20 GaAs wells with the well width of 60 Å, which act to trap free carriers moving across the barriers, following the approach of Dremin et al. [6.9]. Third, we use a coupled quantum well sample with p-i-n structure, because we know that only the coupled quantum wells which has a n-i-n structure with metallic heavily-doped n-type GaAs in the substrate and capping layers, gives a permanent conduction electron density in the wells of a few times $10^{10} cm^{-2}$ by tunnelling of electrons from the n-doped layers through the barriers [6.7]. Last, the excitons are created using a laser with wavelength nearly resonant with the single-well exciton energy. All of

these approaches lead to a strong reduction in the current; for these samples the typical dark current is less than 1 $\mu A/cm^2$.

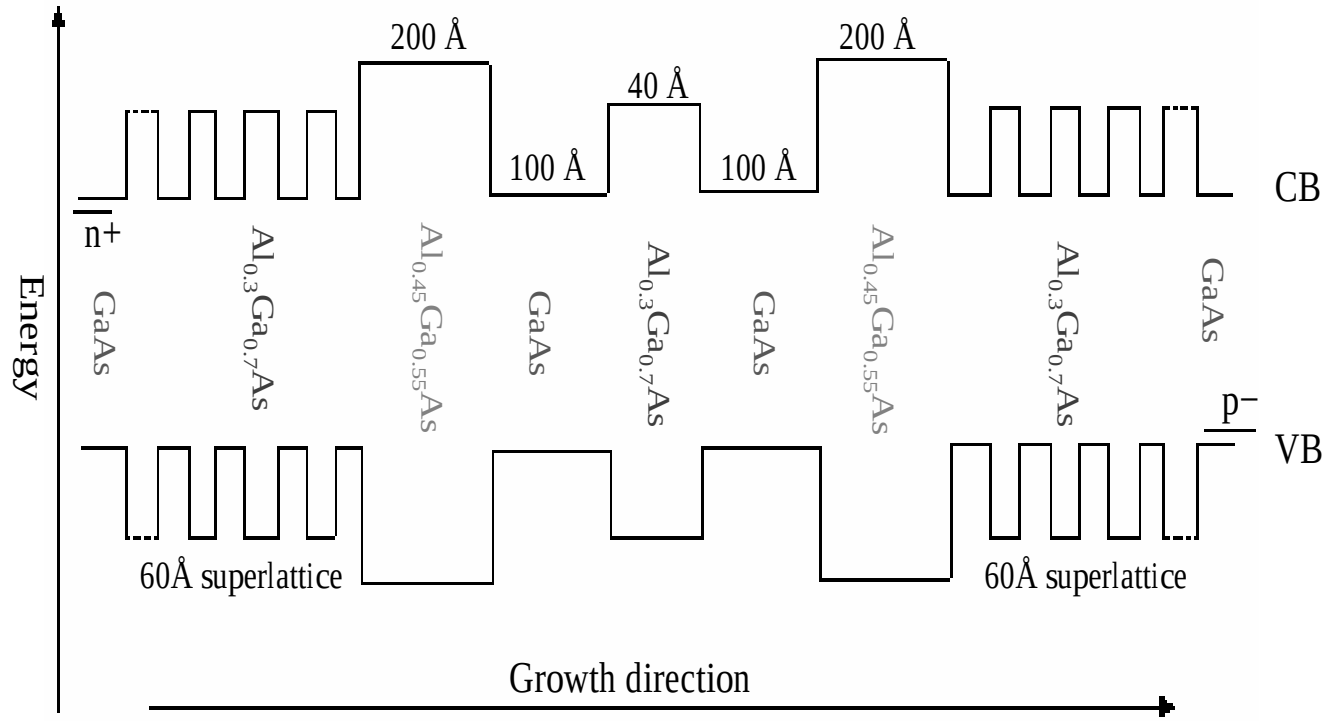

Figure 31: Schematics of the coupled quantum wells structure used in this experiment.

All of the above design features lead to a structure in which the indirect excitons have low disorder and high mobility. The inhomogeneous broadening of the luminescence in this structure, i.e. the energy scale of the disorder, is approximately 1 meV, compared to the indirect exciton binding energy at high electric field of 3.5 meV [6.10]. For this disorder energy, recent calculations [6.11] for indirect excitons in the presence of short-range disorder imply that the excitons will become delocalized in our experiments. These calculations found that above a critical density, which depends on the disorder energy and the electron-hole separation, indirect excitons in the presence of short-range disorder act essentially as free, two-dimensional excitons. For the disorder energy and exciton binding energy of our samples, this critical density for delocalization is approximately $5 \times 10^{10} cm^{-2}$ [6.11]. This density is easily obtainable with our laser pulse energies of several tens of pJ, when the laser is focused

to a spot with a radius of 30 μm, even taking into account the possibility of low efficiency in the exciton creation process.

6.2 THE INDIRECT EXCITON LONG-DISTANCE TRAVEL

Fig. 32 shows a time-integrated image of the indirect exciton luminescence, following a short (200 fs) laser pulse resonant with the single-well exciton energy, for the coupled quantum well system described above, immersed in liquid helium at T = 2 K. As mentioned in Chapter 2, this image was taken by projecting an image of the sample onto the entrance slit of an imaging spectrometer with a CCD camera on the back focal plane, so that the horizontal axis corresponds to the position of the sample while the vertical axis corresponds to the luminescence photon energy. Although the laser is focused to a tight spot of 30 μm, the exciton luminescence is spread over hundreds of microns, due to the motion of the excitons. The bright, spectrally broad but spatially narrow line is luminescence from the doped GaAs substrate and capping layer, which are necessarily also excited by the laser. The substrate luminescence has short lifetime and therefore does not spread out spatially. The exact energy of the indirect excitons depends on the applied electric field, according to the quantum confined Stark effect [6.12]. In these experiments, the indirect exciton line is shifted by high electric field to an energy below the bulk GaAs band gap.

As seen in Figure 32, the indirect exciton energy is shifted upward in the center, where the density is highest, and is lower for locations away from the center, falling back to the unrenormalized value as the density of the excitons drops. This is consistent with the expected mean-field blue shift of bosons with repulsive interaction potential. The size of the exciton cloud becomes larger at higher densities, approximately proportional to the square root of the laser power, which also indicates that there is a pressure in the exciton gas due to the repulsive interactions between the excitons.

Figure 33 shows time-resolved luminescence for various distances from the excitation spot. The rise time of the luminescence is longer for spots further away from the excitation spot, consistent with the picture that the excitons move out from the excitation spot without becoming localized. The lifetime of the excitons is 6.5 μs, in agreement with the calculated

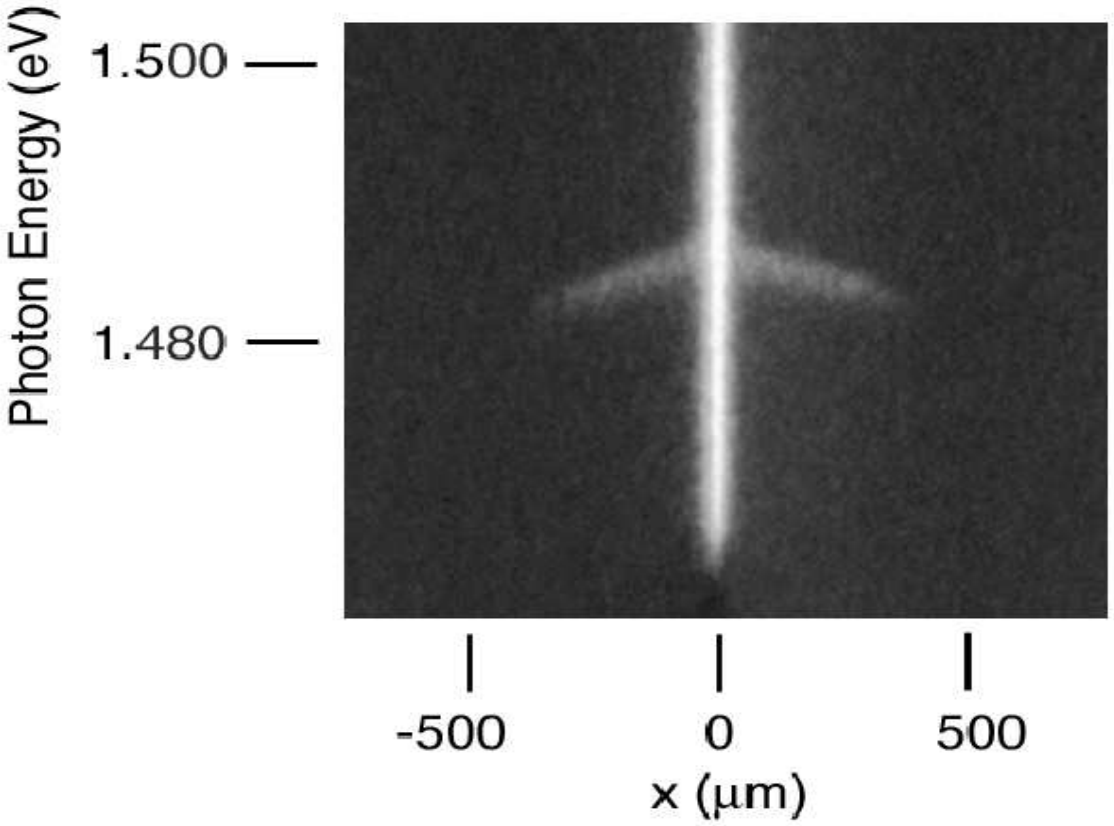

Figure 32: Time-integrated image of the luminescence from the indirect excitons, taken using an imaging spectrometer so that the vertical axis corresponds to the energy of the emitted photons, while the horizontal axis corresponds to the position in the plane of the quantum wells. The central, spatially narrow but spectrally broad line corresponds to light emission from the doped GaAs substrate and capping layers, while the spatially broad but spectrally narrow line corresponds to the emission from the indirect excitons, of interest in this study.

enhancement of the oscillator strength of the indirect excitons [6.10]. In all cases the period between laser pulses was 4 μs, which means that some of the excitons created by each laser pulse will remain at the time of the succeeding pulse. The diffusion constant implied by these data is 180 cm^2/s, which corresponds to an effective mobility of 1,000,000 $cm^2/(V \cdot s)$. Unlike previous experiments [6.5, 6.6], there are no intermediate dark states, the exciton cloud moves continuously from the laser spot outward.

We conclude that the excitons act as a free gas, travelling distances of hundreds of microns. This is an essential point, because the free motion of the excitons over long distances must be established if we are to believe that we observe a thermodynamic phase transition

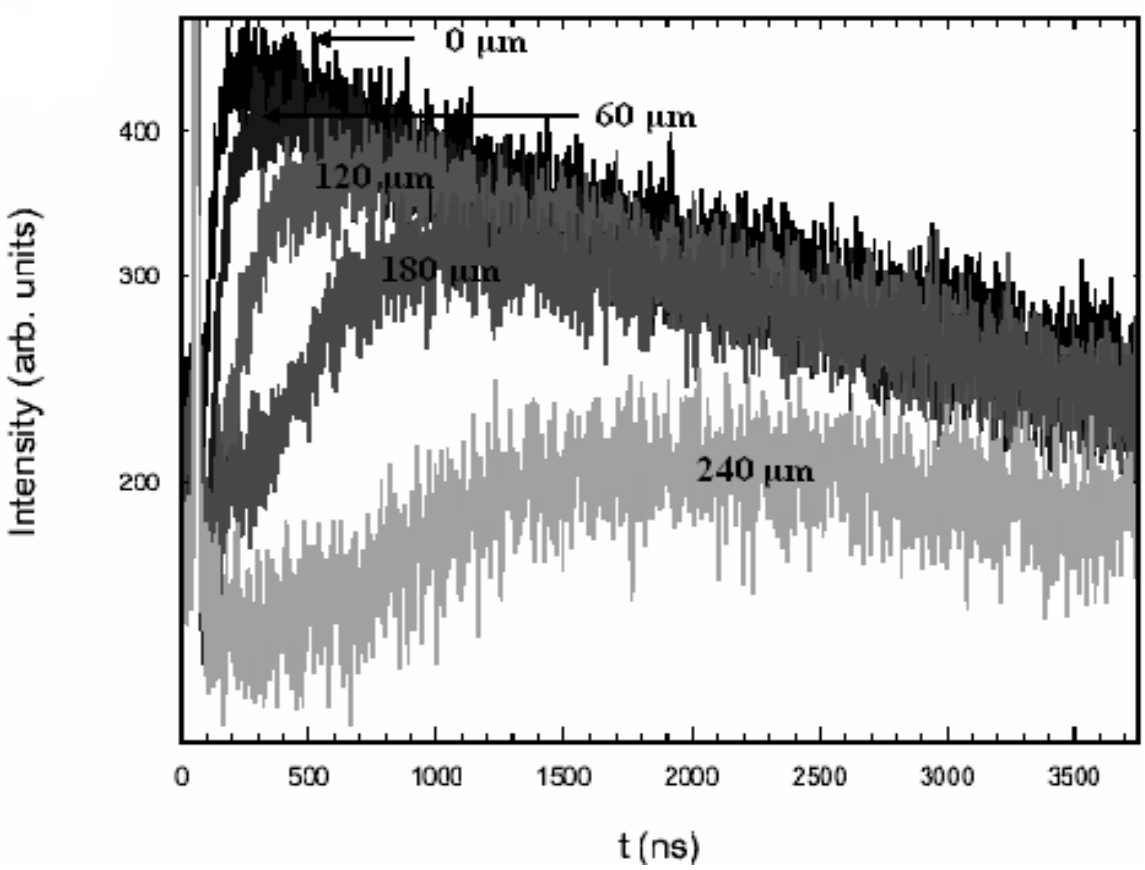

Figure 33: Luminescence intensity as a function of time, for various distance x from the excitation spot, as specified in the figure in the units of μm, under the same conditions as Figure 32. The position in the plane is offset by the same value of y = $50\mu m$ for all the curves, to reduce the contribution of the light emission from the substrate and capping layer.

and not localized excitons.

6.3 PROMISING EVIDENCE FOR BEC OF THE INDIRECT EXCITONS IN A 2D HARMONIC POTENTIAL TRAP

Because BEC is not possible in two dimensions unless there is a confining potential, we create a harmonic potential minimum in the plane of the excitons using the stress method described in Chapter 2.

Previous experiments [6.13, 6.14] have attempted to observe a Kosterlitz-Thouless superfluid transition in a translationally invariant system, but the hydrodynamics of a freely

expanding superfluid are poorly understood. Alternatively, some previous work [6.9] has centered around accumulation of excitons in local minima created by disorder in the wells, but these minima are very small and their exact spatial profile is poorly mapped.

In order for the excitons to act as a gas confined in a potential minimum, the diffusion length of the excitons must be comparable to the equilibrium size of the exciton cloud in the trap. This is the case in our experiments for these high-mobility excitons. Figure 34(a) shows the exciton luminescence energy vs. position in the two-dimensional plane for a harmonic potential created by stress. The excitons were created on one side of the potential minimum, and they then flowed from the excitation spot in all directions toward the energy minimum. Although the potential energy is not strictly a harmonic potential, we can approximate the potential energy at the minimum as a harmonic potential $U(x) = \frac{1}{2}kx^2$, with an effective spring constant of $k = 31 \pm 3 eV/cm^2$. As seen in this figure, the excitons move a long distance from the creation spot, flowing distances comparable to the size of the harmonic potential trap. Again, this shows that the excitons are delocalized and flow freely in response to the drift force created by the stress gradient. If we move the laser spot to the center of the trap, the exciton cloud contracts into a small cloud at the bottom of the trap. Figure 34(b) shows an image made in the same way, but with the laser moved to the center of the trap. Figure 34(c) shows the profile of the exciton luminescence intensity in the trap for various times after the laser pulse. At early times the profile is a sum of the distribution left over from the previous laser pulse and the newly deposited excitons with spatial width approximately 30 μm. At late times, the exciton gas maintains a nearly constant size, which shows that the trap acts to confine the exciton gas. The gas does not have a truly equilibrium distribution at any time, however, since the excitons recombine and diffuse through the trap with the scales comparable to the time between the laser pulses.

As discussed in Section (1.2.3), in principle, BEC in a harmonic potential minimum implies a spatial condensation in the lowest eigen-state of the potential, however, the interactions between the excitons will cause the condensate to broaden spatially [6.15]. And for strong interactions at high enough exciton density, the size can become comparable to the classical equilibrium distribution, which indicates that there will not be a spatial condensate.

On the other hand, the momentum distribution of the excitons can be calculated by

taking a Fourier transform of the spatial distribution, which means that a broad spatial distribution gives a narrow momentum distribution. For the non-interacting boson gas, the ground state spatial Gaussian distribution with a narrow width A^c gives a very broad momentum Gaussian distribution having a width proportional to $\frac{1}{A^c}$. However, at high exciton density, the momentum distribution becomes much narrower, because the condensate is spatially broadened by the strong interactions. This can also be deduced from $\Delta k \cdot \Delta x \geq \frac{\hbar}{2}$ [6.16], an uncertainty relation between spatial coherence size (Δx) and momentum space coherence size (Δk). Therefore, as concluded by Keeling *et al.* [6.17], the in-plane momentum distribution of the condensate at high exciton density has a strongly peaked angular distribution of the emitted light, which differs strongly from that of particles in excited states. Essentially, if the condensate is in the lowest momentum state, then the in-plane momentum is zero, and since the light emission process conserves the in-plane k-vector, the light emission should correspond to a diffraction-limited beam emitted normal to the plane in which the excitons are confined. The experimental set-up for the measurement of the angular profile of the indirect exciton luminescence is shown in Figure 35.

Figure 36 shows the angular distribution of the luminescence light emission from the quantum well structure for several different powers. Typically, one thinks of keeping the density constant and dropping the temperature to approach the BEC phase transition, but as mentioned above, the temperature of the excitons is not a control parameter, instead being determined by the rate of phonon emission. Instead, one can approach the BEC phase transition by keeping all conditions the same and increasing the particle density, e.g. in our case by simply turning up the laser power. The effective temperature of the excitons should remain constant. As seen in Fig. 36, at low excitation power, the angular distribution is broad, corresponding to the maximum angular acceptance of our light collection system, while at high exciton density, a central peak appears. In other words, the light emission is in the form of a beam, which has angular width of 0.014 radians. This implies a source size of 70 μm, assuming diffraction-limited emission, i.e. $\Delta\theta = 1.22\lambda/d$. This is smaller than the equilibrium distribution size of 150 μm, but a reasonable estimate of the size of the high-density cloud created by the laser pulse. Our time-resolved measurements indicates that the beam-like emission occurs primarily only at very short time delays after the laser

pulse, consistent with the prediction [6.18] that the emission from the excitonic condensate should be superradiant, with very short lifetime.

This behavior is strikingly different from that of a non-degenerate exciton gas. Luminescence emission from excitons in quantum wells at T = 2 K is emitted in all directions. This appearance of a narrow, beamlike emission is a dramatic confirmation of a theoretical prediction for an excitonic condensate. There is no stimulated emission of photons in these experiments, because the emission rate of photons is extremely slow, due to the long lifetime of the indirect exciton states. However, one open question is that Keeling *et al.* [6.17] and Roland Zimmermann [6.19] predict that the angular peak in the exciton photoluminescence only appears at much lower temperature, around 0.2 Kelvin, which deserves further investigations.

As a check, we can compare the expected number of excitons in the trap to the theoretical prediction for the critical density for BEC. For a non-interacting gas, the critical number of particles needed for condensation in a harmonic potential in two dimensions is equal to

$$N_c = \frac{1.6g(k_B T)^2}{(\hbar\omega_0)^2}, \tag{6.1}$$

where g is the spin degeneracy (equal to 4 for excitons in GaAs), k_B is Boltzmann's constant, and $\omega_0 = \sqrt{k/m}$ is the natural frequency of the harmonic potential. For the effective spring constant of 31 eV/cm^2, and the effective mass of the excitons in the plane of the quantum wells of 0.14 m_0, where m_0 is the vacuum electron mass, this implies a critical number of excitons at T = 2 K of $N = 10^6$. The critical threshold of 10 mW average power, seen in Fig. 31, corresponds to $1.6 * 10^{11}$ photons per pulse. Approximately 30% of the light will be reflected from the surface of the GaAs, and the absorption length in GaAs for the laser wavelength of 797 nm is approximately 100 μm, while the total quantum well thickness is $240\mathring{A} = 0.024\mu m$, which means that the fraction of phonons absorbed in the quantum well structure is approximately $(0.024)/100 = 2.4 * 10^{-4}$. This implies approximately $2.5 * 10^7$ absorbed photons. This is well above the needed number for BEC in the trap.

A complete theory, of course, should take into account the interactions of the excitons, since as discussed above, we know that the exciton interactions give a blue shift of up to 2 meV in the regions of highest exciton density, which effectively flattens out the harmonic

potential. We also note that the average density, found by dividing the total number of excitons by the occupied area $(150\mu m)^2$, is equal to $8 * 10^{10} cm^{-2}$, well above the critical threshold for delocalization in the presence of disorder, discussed above.

6.4 CONCLUSIONS

We therefore conclude that we have observed promising evidence for BEC of excitons in two dimensions, in a way quite similar to the first observations of BEC in alkali atoms in a harmonic potential [6.20]. An unambiguous claim of the Bose condensation of the indirect excitons needs a lot of further work to be done, for example, to detect other signatures of BEC which are discussed in Chapter 1. However, this opens the door to a whole range of investigations, including attempts to observe coherence of the emitted light, proof of superfluidity of the excitons, and other fascinating effects.

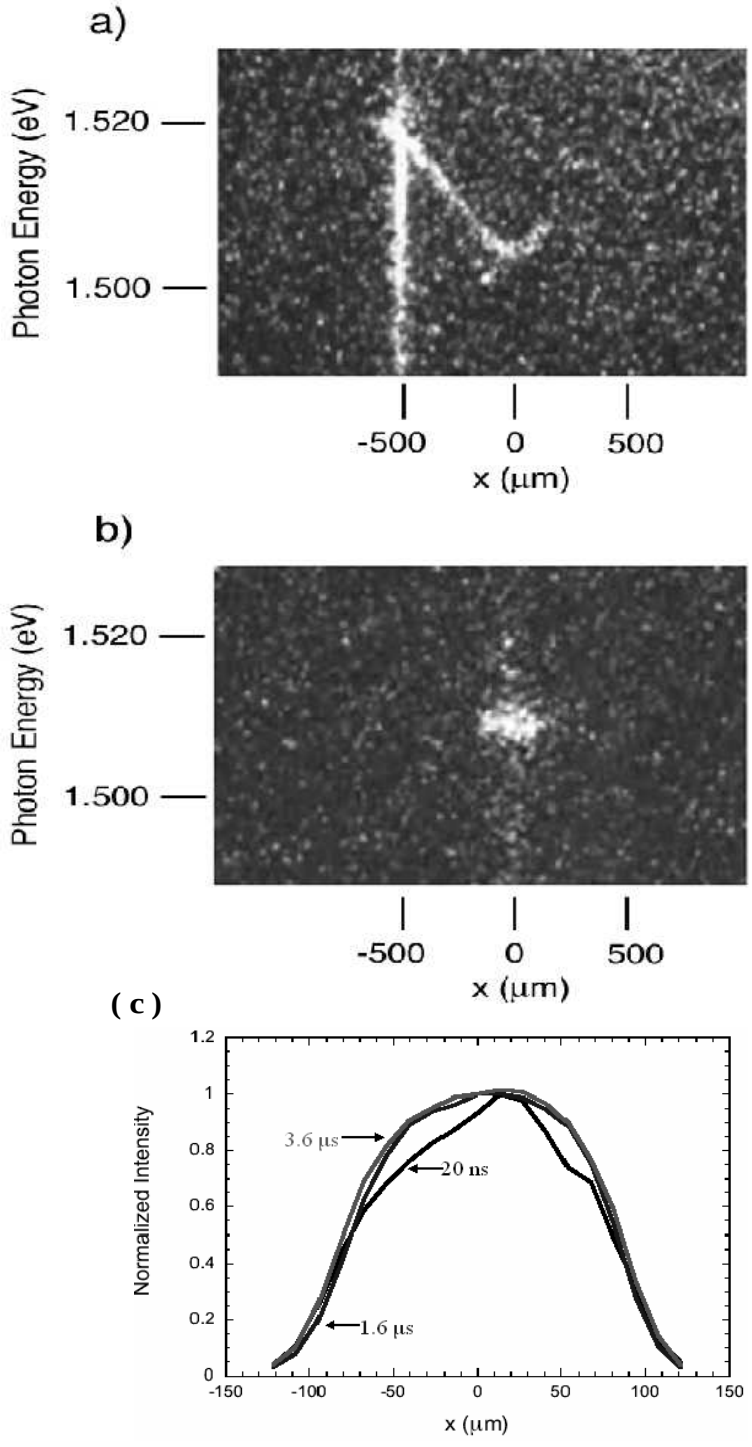

Figure 34: (a) Exciton luminescence energy as function of position, when the laser excitation spot is located near to a potential minimum created by externally applied stress. The image is recorded in the same way as Figures 32 and 33. (b) The same conditions, but the laser spot moved to the center of the potential minimum. The laser excitation spot has been translated 50 μm in the perpendicular direction in the plane of the excitons, to reduce the light from the substrate and capping layer. (c) The intensity of the luminescence as a function of position, for various time delays after the laser pulse, under the same conditions as (b).

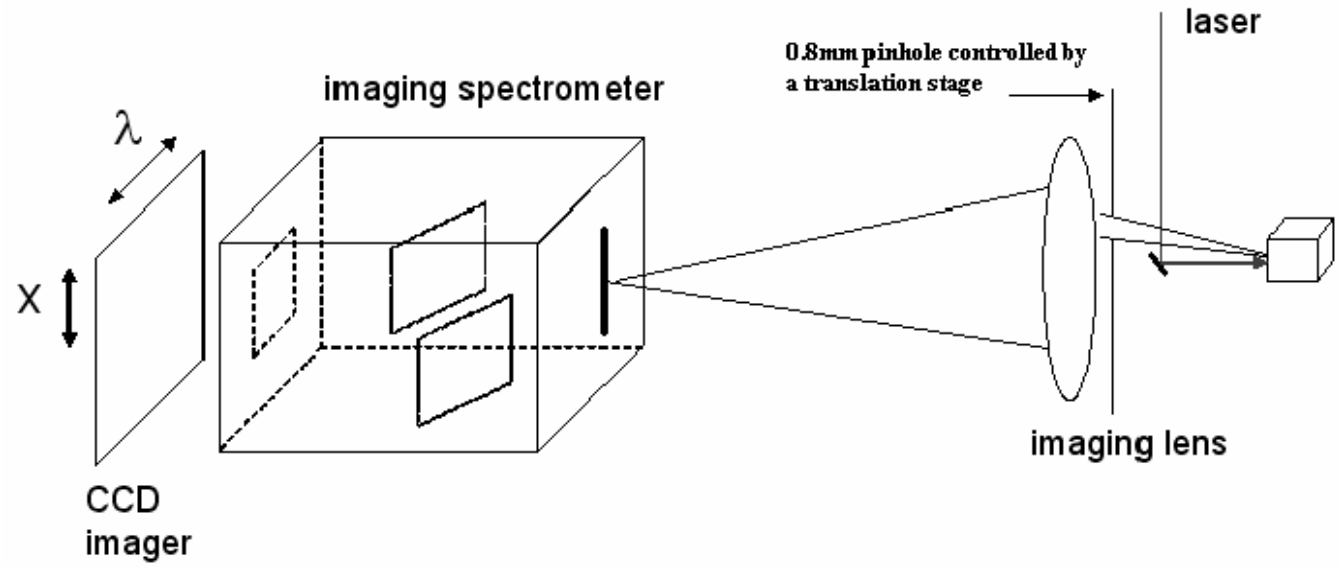

Figure 35: Schematic of the experimental set-up for the measurement of the angular profile of the indirect exciton luminescence.

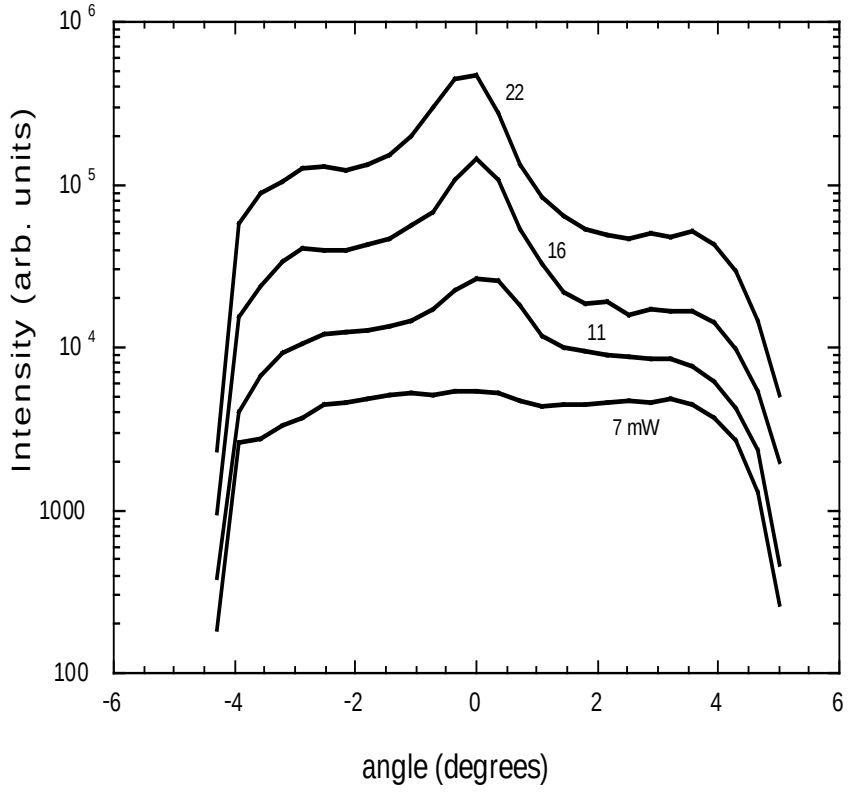

Figure 36: Angular distribution of the light emission from the indirect excitons, for various laser powers. The angular width of the low-power emission corresponds to the response of our light collection system to a uniform source; i.e., our system has 9 degree total angular acceptance from the imaging lens. The angular resolution of our system is 0.5 degree.

7.0 CONCLUSIONS AND OUTLOOK

The most exciting conclusion from this work is that BEC of excitons is possible in both two-dimensional and three-dimensional systems.

In three dimensions, Cu_2O is a promising system. We established a good experimental set-up for the condensation of the excitons in Cu_2O. After investigating the selection rules of the creation and detection of excitons, and the two possible big barriers for the condensation under debate, the Auger non-radiative recombination process and the conversion mechanism between orthoexcitons and paraexcitons, we have the following conclusions:

1. The BEC of excitons in Cu_2O should be done at the lowest exciton state, the paraexciton state in the 1s-"yellow" exciton series.

2. In order to create and detect the paraexciton, an external perturbation is necessary, for example with a uniaxial inhomogeneous stress. For most of our experiments, we apply the external stress along the [001] axis, because it is easy to be established experimentally. For detecting the paraexciton, the detector has to face a surface along either [110] or [111] axis of the Cu_2O sample. Although there are a lot of choices for the direction of the wave vector and polarization of an input laser beam, it should obey the strict selection rules listed in Tables 8 and 11.

3. An uniaxial stress, which is as small as possible to spectrally separate the paraexciton, should be used, because the Auger recombination process may be a barrier for the condensation and the Auger rate increases with the applied stress. The Auger recombination constant is weakly dependent on temperature in the low temperature region and linearly increases with temperature at high temperatures.

4. The resonant two-photon excitation has a lot of advantages over the single-photon excitation, for example, the two-photon excitation directly creates paraexcitons, as shown in

Chapter 5.

Therefore, we resonantly create highly-forbidden paraexcitons in Cu_2O with an IR laser beam tuned to one half the paraexciton ground-state energy in a harmonic potential trap with the Auger recombination process as small as possible (at low temperature and low stress); and found that the exciton creation efficiency in resonant two-photon excitation is greater for one-beam excitation than for two colliding pulses, but the colliding pulse method may be useful for direct creation of a condensate in the ground state. However, at present, the paraexciton density in this work is about thirty times less than the required density for BEC of paraexcitons. Therefore, one promising direction for the observation of BEC of excitons in Cu_2O is that with higher laser power from stronger IR laser sources or lower temperature, the critical density can be approached under one-beam two-photon excitation resonant with the paraexciton state.

Moreover, we have seen that spin flip by phonon emission is the dominant mechanism for conversion of orthoexcitons to paraexcitons in Cu_2O. Spin flip by phonon emission may also occur in many other materials, but it has not been well studied. With the growing interest in "spintroincs", this mechanism deserves further attention.

In two dimensions, a good system for the condensation of excitons is the indirect excitons in our GaAs-based coupled quantum well structure which has been modified with four design strategies—highest possible barriers, introducing into the barriers a superlattice of 60 ÅGaAs wells, the p-i-n structure, and wider quantum wells. All of the design features lead to a structure in which the indirect excitons have low disorder and high mobility. With a cold resonant excitation, we conclude that the excitons act as a free gas, travelling distances of hundreds of microns. This is an essential point, because the free motion of the excitons over long distances must be established if we are to believe that we observe a thermodynamic phase transition and not localized excitons.

Confining the indirect excitons in harmonic potential traps is necessary, because Bose-condensation can't occur in two dimensions without the traps.

We also present evidence that we have observed BEC of indirect excitons in two dimensions in the coupled quantum well structure, in a way quite similar to the first observations of BEC in alkali atoms in a harmonic potential. An ambiguous claim of the Bose condensation

of the indirect excitons needs a lot of further work to be done, for example, detect other signatures of BEC which are discussed in Chapter 1. Nevertheless, this opens the door to a whole range of investigations, including attempts to observe coherence of the emitted light, proof of superfluidity of the excitons, and other fascinating effects.

APPENDIX

ELECTRIC QUADRUPOLE OPERATOR

The electromagnetic interaction, E, is given by Jackiw in Page 225 of the book "Intermediate Quantum Mechanics",

$$E = \frac{e}{mc}\vec{p}\cdot\vec{A}, \tag{.1}$$

$$\text{where,} \quad \vec{A} = \vec{\lambda}e^{i(\vec{k}\cdot\vec{r})}\frac{\varepsilon}{i\omega}, \tag{.2}$$

and e, m are change and mass of an electron respectively, and c is the speed of light. $\vec{p}$ is the momentum operator, $\vec{p} = \vec{k}\cdot\vec{r}$, where $\vec{k}$ is the wave vector of the input laser beam with energy of $\hbar\omega$, and $\vec{r}$ is the space vector. By substituting equation (2) into equation (1), the interaction E is,

$$E = (\frac{e}{mc}\frac{\varepsilon}{i\omega})\vec{p}\cdot\vec{A}e^{i(\vec{k}\cdot\vec{r})} \tag{.3}$$

With Taylor-expansion,

$$\begin{aligned} E &= \frac{e\varepsilon}{imc\omega}\vec{p}\cdot\vec{A}(1 + i\vec{k}\cdot\vec{r} + ...) \\ &= \frac{e\varepsilon}{imc\omega}(\vec{p}\cdot\vec{A} + \frac{1}{2}[(\vec{p}\cdot\vec{\lambda})(\vec{k}\cdot\vec{r}) + (\vec{k}\cdot\vec{r})(\vec{p}\cdot\vec{\lambda})] + \\ &\qquad + \frac{1}{2}[(\vec{p}\cdot\vec{\lambda})(\vec{k}\cdot\vec{r}) - (\vec{k}\cdot\vec{r})(\vec{p}\cdot\vec{\lambda})] + ...) \end{aligned} \tag{.4}$$

The first term in equation (4) is the electro-dipole operator, and the second term is the electro-quadrupole operator, Q, and the third term is the magneto-dipole operator. Therefore,

$$Q = \frac{e\varepsilon}{imc\omega}\frac{1}{2}[(\vec{p}\cdot\vec{\lambda})(\vec{k}\cdot\vec{r}) + (\vec{k}\cdot\vec{r})(\vec{p}\cdot\vec{\lambda})] \tag{.5}$$

Because,

$$[(\vec{p}\cdot\vec{\lambda})(\vec{k}\cdot\vec{r})+(\vec{k}\cdot\vec{r})(\vec{p}\cdot\vec{\lambda})] = (\sum_i p_i\lambda_i)(\sum_j k_j r_j)+(\sum_i p_i\lambda_i)(\sum_j k_j r_j)$$
$$= \sum_{i,j}\lambda_i k_j(p_i r_j + r_j p_i), \tag{.6}$$

by substituting equation (6) into equation (5), the quadrupole operator is,

$$Q = \frac{e\varepsilon}{imc\omega}\frac{1}{2}\sum_{i,j}\lambda_i k_j(p_i r_j + r_j p_i) \tag{.7}$$

And from Quantum Mechanics,

$$p_i r_j + r_j p_i = \frac{i\hbar}{2}(\nabla^2 r_i r_j - r_i r_j\nabla^2) - i\hbar\delta_{ij} \tag{.8}$$

the quadrupole operator can be expressed as,

$$Q = \frac{e\varepsilon}{imc\omega}\frac{1}{2}\frac{i\hbar}{2}[\sum_{i,j}\lambda_i k_j(\nabla^2 r_i r_j - r_i r_j\nabla^2) - 2\delta_{ij}] \tag{.9}$$

If the final and initial states are $|i\rangle$ and $|f\rangle$, we can have the following relationship,

$$\langle f|Q|i\rangle = \frac{\hbar e\varepsilon}{4mc\omega}[\langle f|\sum_{ij}\lambda_i k_j(\nabla^2 r_i r_j - r_i r_j\nabla^2)|i\rangle - 2\langle f|\delta_{ij}|i\rangle]. \tag{.10}$$

Because,

$$\begin{aligned}
\nabla^2|i\rangle &= \frac{2m}{\hbar^2}\hbar\omega_i|i\rangle,\\
\langle f|\nabla^2 &= \langle f|\frac{2m}{\hbar^2}\hbar\omega_f,\\
&\Rightarrow\\
\langle f|Q|i\rangle &= \frac{\hbar e\varepsilon}{4mc\omega}\frac{2m}{\hbar^2}\hbar(\omega_f-\omega_i)\langle f|\sum_{ij}\lambda_i k_j r_i r_j|i\rangle
\end{aligned} \tag{.11}$$

The electro-quadrupole operator Q is simplified as,

$$Q = \frac{e\varepsilon}{2}\sum_{ij}\lambda_i k_j r_i r_j, \tag{.12}$$

which is used in Chapters 3 and 4.

BIBLIOGRAPHY

[1] Bibliography for Chapter 1

[1.1] S. A. Moskalenko and D. W. Snoke, Bose-Einstein Condensation of Excitons and Biexcitons, Cambridge University Press (2000).

[1.2] F. Reif, Fundamentals of Statistical and Thermal Physics (McGraw-Hill, New York, 1965).

[1.3] F. Dalfovo, S. Giorgini, L. P. Pitaevskii and S. Stringari, Rev. Modern Phys. 71, 463 (1999).

[1.4] K. Huang, Statistical Mechanics (Wiley, New York, 1963).

[1.5] Ladislaus Banyai, "BEC in a 2d oscillator potential", to appear, (2004).

[1.6] D. P. Trauernight, J. P. Wolfe and A. Mysyrowicz, Phys. Rev. B 34, 2561 (1986).

[1.7] V. V. Goldman, I. Silvera and A. J. Leggett, Phys. Rev. B 24, 2870 (1981).

[1.8] J. Keeling, L. S. Levitov and P. B. Littlewood, Angular distribution of photoluminescence as a probe of Bose condensation of trapped excitons. Phys. Rev. Lett. 92, 176402/1-4 (2004).

[1.9] M. H. Anderson, J. R. Ensher, M. R. Matthews, C. E. Weiman, and E. A. Cornell, Science 269, 198 (1995).

[1.10] C. C. Bradley, C. A. Sacket, J. J. Tollet, and R. Hulet, Phys. Rev. Lett 75, 1687 (1995).

[1.11] K. B. Davis, M. O. Mewes, M. R. Andrews, N. J. van Druten, D. S. Durfee, D. M. Kurn, and W. Ketterle, Phys. Rev. Lett 75, 3969 (1995).

[1.12] S. Denev and D. W. Snoke, Phys. Rev. B 65, 085211 (2001).

[1.13] V. T. Agekyan, Review article, Phys. Stat. Sol. (a) 43. 11 (1977)

[1.14] H. Matsumoto, K. Saito, M. Hasuo, S. Kono and N. Nagasawa, Solid State Comm., Vol. 97, No. 2, 125-129 (1996).

[1.15] V. C. Negoita, Ph. D. thesis (2001).

[1.16] J. L. Lin and J. P. Wolfe, Phys. Rev. Lett. 71, 1223 (1993)

[1.17] T. Goto, M. Y. Shen, S. Koyama, and T. Yokouchi, Phys. Rev. B 55, 7609 (1997)

[1.18] M. Y. Shen, T. Yokouchi, S. Koyama, and T. Goto, Phys. Rev. B 56, 13066 (1997)

[1.19] D. W. Snoke, Phys. Stat. Sol. (b) 238, No. 3, 389 (2003)

[1.20] D. W. Snoke, J. P. Wolfe and A. Mysyrowicz, Phys. Rev. lett. 59, 827 (1987)

[1.21] K. E. O'Hara, L. O. Suilleabhain and J. P. Wolfe, Phys. Rev. B 60, 10565 (1999)

[1.22] D. W. Snoke, J. P. Wolfe and A. Mysyrowicz, Phys. Rev. Lett. 41, 11171 (1990)

[1.23] E. Fortin, S. Farard and A. Mysyrowicz, Phys. Rev. Lett. 70, 3951 (1993)

[1.24] A. Mysyrowicz, E. Fortin, E. Benson, S. Farad, and E. Hanamura, Solid State Commun. 92, 957 (1994)

[1.25] E. Benson, E. Fortin, and A. Mysyrowicz, in Bose-einstein condensation, A. Griffin, D. W. Snoke, and S. Stringari, eds. (Cambridge U. Press, Cambridge, 1995)

[1.26] A. E. Bulatov and S. G. Tikhodeev, Phys. Rev. B 46, 15058 (1992)

[1.27] H. Haug and H. H. Kranz, Z. Phys. B 53, 151 (1983)

[1.28] H. Shi, G. Verechaka and A. Griffin, Phys. Rev. B 50, 1119 (1994)

[1.29] J. T Warren, K. E O'Hara, and J. P. Wolfe, Phys. Rev. B 61, 8215 (2000).

[1.30] K. E O'Hara, J. R. Gullingsrud, and J. P. Wolfe, Phys. Rev. B 60, 10872 (1999).

[1.31] G. M. Kavoulakis, Gordon Baym, and J. P. Wolfe, Phys. Rev. B 53,7227 (1996).

[1.32] A. Jolk, M. Jorger, and C. Klingshirn, Phys. Rev. B 65, 245209 (2002).

[1.33] D. W. Snoke, A. Shields, and M. Cardona, Phys. Rev. B 45, 11693 (1992).

[1.34] G. M. Kavoulakis and G. Baym, Phys. Rev. B 54, 16625 (1996).

[1.35] K. E. O'Hara, J. R. Gullingsrud, and J. P. Wolfe, Phys. Rev. B 60, 10872 (1999).

[1.36] D. W. Snoke and V. Negoita, Phys. Rev. B 61, 2904 (2000).

[1.37] G. M. Kavoulakis and A. Mysyrowicz, Phys. Rev. B 61, 16619 (2000).

[1.38] J. Shumway and D. M. Ceperley, Phys. Rev. B 63, 165209 (2001).

[1.39] N. Caswell and P. Y. Yu, Phys. Rev. B 25, 5519 (1982).

[1.40] D. W. Snoke, J. P. Wolfe, and D. P. Trauernicht, Phys. Rev. B 41, 5266 (1990).

[1.41] D. W. Snoke, V. Negoita, Phys. Rev. B 61, 2904 (2000).

[1.42] T. Fukuzawa, E. E. Mendez, and J. M. Hong, Phys. Rev. Lett. A 64, R3066 (1990).

[1.43] J. A. Kash, M. Zachau, E. E. Mendez, J. M. Hong, and T. Fukuzawa, Phys. Rev. Lett. 66, 2247 (1991).

[1.44] L. V. Butov, A. Zrenner, G. Abstreiter, G. Bohm, and G. Weimann, Phys. Rev. Lett. 73, 304 (1994).

[1.45] L. V. Butov, A. C. Gossard, and D. S. Chemla, Nature 418, 751-754 (2002).

[1.46] A. V. Larionov, V. B. Timofeev, J. Hvam, and K. Soerensen, JETP 90, 1093 (2000).

[1.47] D. W. Snoke, Y. Liu, S. Denev, K. West and L. Pfieffer, Solid State commun. 127, 187 (2003).

[1.48] Private communications with Gang Chen, the first international ICSCE meeting, May 2004.

[2] Bibliography for Chapter 2

[2.1] S. A. Moskalenko and D. W. Snoke, Bose-Einstein Condensation of Excitons and Biexcitons, Cambridge University Press (2000).

[2.2] V. C. Negoita, Ph. D. thesis (2001).

[2.3] D. W. Snoke and V. Negoita, Phys. Rev. B 61, 2904 (2000).

[2.4] S. Denev and D. W. Snoke, Phys. Rev. B 65, 085211 (2001).

[2.5] A. Mysyrowicz, D. P. Trauernicht, J. P. Wolfe, and H. R. Trebin, Phys. Rev. B 27, 2562 (1983).

[2.6] J. Y. Zhang, J. Y. Huang, Y. R. Shen and C. Chen, J. Opt. Soc. Am. B 10 (1993).

[2.7] Amnon Yariv, Optical Electronics in Modern Communication, Oxford University Press (1996).

[2.8] Richard L. Sutherland, Handbook of Nonlinear Optics, Marcel Dekker Inc. (1996).

[3] Bibliography for Chapter 3

[3.1] G. F. Koster, J. O. Dimmock, R. G. Wheeler, and H. Statz, "Properties of the Thirty-two Point Groups", (MIT Press, Cambridge, Mass, 1963)

[3.2] S. A. Moskalenko and D. W. Snoke, Bose-Einstein Condensation of Excitons and Biexcitons, Cambridge University Press (2000).

[3.3] Todd R. Bader and Albert Gold, Phys. Rev. 171, 997, (1968).

[3.4] Y. Sun, G. K. L. Wong and J. B. Ketterson, Phys. Rev. B **63**, 125323-1 (2001).

[3.5] M. Y. Shen et al., Phys. Rev. B **53**, 13477 (1996).

[3.6] S. Kono, M. Hasuo and N. Nagasawa, Journal of Luminescence 66&67, 433-437, (1996).

[3.7] M. Kubouchi, K. Yoshiot, R. Shimano, A. Mysyrovwicz and M. Kuwata-Gonokami, APS/123-QED, in press (2004).

[3.8] N. Naka and N. Nagasawa, Phys. Rev. B **65**, 245203 (2002).

[3.9] Yingmei Liu and David Snoke, cond-mat/0408188 (2004).

[4] Bibliography for Chapter 4

[4.1] S. Denev and D. W. Snoke, Phys. Rev. B 65, 082511 (2002).

[4.2] D. W. Snoke and V. Negoita, Phys. Rev. B 61, 2904 (2000).

[4.3] J. S. Weiner, N. Caswell, P. Y. Yu, and A. Mysyrowicz, Solid State Comm. 46, 105 (1983).

[4.4] See, e.g., B. K. Ridley, "Quantum Processes in Semiconductors", 2nd ed. (Oxford University Press, Oxford, 1988), chapter 1.

[4.5] A. Daunois, J. L. Desis, and B. Meyer, J. Phys. (Paris) 27, 142 (1966).

[4.6] See, e.g., M. Cardona, "Light Scattering in Solids I", First Edition, (Springer, 1983), page 11.

[4.7] K. E. O'Hara, J. R. Gullingsrud, and J. P. Wolfe, Phys. Rev. B 60, 10872 (1999).

[4.8] A. Jolk, M. Jörger, and C. Klingshirn, Phys. Rev. B 65, 245209 (2002).

[4.9] J. T Warren, K. E O'Hara, and J. P. Wolfe, Phys. Rev. B 61, 8215 (2000).

[4.10] V. C. Negoita, Ph.D. thesis, University of Pittsburgh (2001).

[4.11] D. W. Snoke and V. Negoita, Phys. Rev. B **61**, 2904 (2000).

[4.12] I. Pasternyak, Phy. Status Solidi 1, 888 (1959).

[4.13] J. B. Grun, M. Sieskind and S. Nikitine, J. Phys. Chem. Solids, Vol. 19, 189 (1961).

[4.14] S. Denev and D. W. Snoke, Phys. Rev. B **65**, 085211 (2001).

[4.15] G. M. Kavoulakis, Gordon Baym, and J. P. Wolfe, Phys. Rev. B 53, 7227 (1996).

[4.16] G. M. Kavoulakis and Gordon Baym, Phys. Rev. B 54, 16625 (1996).

[4.17] W. C. Tait and R. L. Weiher, Phys. Rev 178, 1404 (1969).

[4.18] D. W. Snoke, D. Braun, and M. Cardona, Phys. Rev. B 44, 2991 (1991).

[4.19] David R. Lide, " Handbook of Chemistry and Physics ", 77th edition (1996-1997)

[4.20] B. K. Ridley, " Quantum Processes in Semiconductors ", 2nd edition (1988)

[4.21] M. Moskalenko and D. Snoke, " Bose-Einstein Condensation of Excitons and Biexcitons ", Cambridge University Press (2000)

[5] Bibliography for Chapter 5

[5.1] S. Denev and D. W. Snoke, Phys. Rev. B **65**, 085211 (2001).

[5.2] V. C. Negoita, Ph.D. thesis, University of Pittsburgh, (2001).

[5.3] D. W. Snoke and V. Negoita, Phys. Rev. B **61**, 2904 (2000).

[5.4] N. Naka and N. Nagasawa, Phys. Rev. B **65**, 075209 (2002).

[5.5] S. Kono, M. Hasuo, and N. Nagasawa, J. Lumin. **66/67**, 433 (1996).

[5.6] A. Jolk, M. Jorger, and C. Klingshirn, Phys. Rev. B **65**, 245209 (2002).

[5.7] Y. Sun, G. K. L. Wong and J. B. Ketterson, Phys. Rev. B **63**, 125323-1 (2001).

[5.8] M. Y. Shen et al., Phys. Rev. B **53**, 13477 (1996).

[5.9] N. Naka and N. Nagasawa, Solid State Comm. **110**, 153 (1999).

[5.10] S. A. Moskalenko and D. W. Snoke, *Bose-Einstein Condensation of Excitons and Biexcitons*, (Cambridge University Press, 2000).

[5.11] D. P. Trauernicht, J. P. Wolfe, and A. Mysyrowicz, Phys. Rev. B **34**, 2561 (1986).

[5.12] Yingmei Liu and David Snoke, "Temperature dependence of exciton Auger decay process in Cu_2O", cond-mat/0408184 (2004).

[5.13] M. Kubouchi, K. Yoshiot, R. Shimano, A. Mysyrovwicz and M. Kuwata-Gonokami, APS/123-QED, in press (2004).

[5.14] M. Inoue and Y. Toyozawa, J. Phys. Soc. Japan **20**, 363 (1965).

[5.15] Todd R. Bader and Albert Gold, Phys. Rev. **171**, 997 (1968).

[5.16] L. A. Ablova and A. I. Bobrysheva, Sov. Phys. Semicond., Vol. 7, No. 6, 712 (1973).

[5.17] D. W. Snoke and V. Negoita, Phys. Rev. B **61**, 2904 (2000).

[6] Bibliography for Chapter 6

[6.1] Bastard, G. Wave Mechanics Applied to Semiconductor Heterostructures. (Halsted, New York, 1988).

[6.2] Snoke D. W. and Crawford, J.D., Hysteresis in the Mott transition between plasma and insulating gas Phys. Rev. E 52, 5796-5799 (1995).

[6.3] Sakaki H., Noda, T., Hirakawa, K., Tanaka, M., and Matsusue T. Interface roughness scattering in GaAs/AlAs quantum wells. Applied Phys. Lett. 51, 1934-1936 (1987).

[6.4] Lozovik, Yu. E. and Berman, O. L. Phase transitions in a system of spatially separated electrons and holes, JETP 84, 1027-1035 (1997).

[6.5] Butov, L. V., Gossard, A. C. and Chemla, D. S. Macroscopically ordered state in an exciton system. Nature 418, 751-754 (2002).

[6.6] Snoke, D., Denev, S., Liu, Y., Pfeiffer, L., and West, K. Long-range transport in excitonic dark states in coupled quantum wells. Nature 418, 754 (2002).

[6.7] Snoke, D., Liu, Y., Denev, S., Pfeiffer, L., and West, K. Luminescence rings and charge separation in quantum well structures. Solid State Comm. 127, 187-196 (2003).

[6.8] R. Rapaport, Gang Chen, D. Snoke, S. H. Simon, L. Pfeiffer, K. West, Y. Liu, and S. Denev. Charge separation of dense two-dimensional electron-hole gases: mechanism for exciton ring pattern formation. Phys. Rev. Lett. 92, 117405/1-4 (2004).

[6.9] Dremin, A. A., Timofeev, V. B., Larionov, A. V., Hvam, J. and Soerensen, K. Phase Diagram of the Bose Condensation of Interwell Excitons in GaAs/AlGaAs Double Quantum Wells, JETP Lett. 76, 450-455 (2002).

[6.10] M. H. Szymanska, private communication. The method of calculation is the same as Szymanska, M. H. and Littlewood, P. B. Excitonic binding in coupled quantum wells Phys. Rev. B 67 193305/1-4 (2003).

[6.11] O. L. Berman, Yu.E. Lozovik, D. W. Snoke and R. D. Coalson, Superfluidity of 'Dirty' indirect excitons in coupled quantum wells. To appear.

[6.12] Andrews, S. R., Murray, C. M., Davies, R. A., and Kerr, T. M. Stark effect in strongly coupled quantum wells. Phys. Rev. B 37, 8198-8204 (1988).

[6.13] Butov L. V., Ivanov, A. L., Imamoglu, A., Littlewood, P. B., Shashkin, A. A., Dolgopolov, V. T., Campman, K. L., and Gossard, A. C. Stimulated Scattering of Indirect Excitons in Coupled Quantum Wells: Signature of a Degenerate Bose-Gas of Excitons. Phys. Rev. Lett. 86, 5608 (2001).

[6.14] Kash, J. A., Zachau, M., Mendez, E.E., Hong, J.M., and Fukuzawa, T. Fermi-Dirac distribution of excitons in coupled quantum wells. Phys. Rev. Lett. 66, 2247-2250 (1991).

[6.15] V. V. Goldman, I.F. Silvera and A.J. Leggett, Atomic hydrogen in an inhomgeneous magnetic field: Density profile and Bose-Einstein condsensation. Phys. Rev. B 24, 2870-2873 (1981).

[6.16] Amnon Yariv, "Quantum Electronic", Third Edition, John Wiley & Sons (1988).

[6.17] J. Keeling, L. S. Levitov and P. B. Littlewood, Angular distribution of photoluminescence as a probe of Bose condensation of trapped excitons. Phys. Rev. Lett. 92, 176402/1-4 (2004).

[6.18] L. S. Levitov and P. B. Littlewood, private communication.

[6.19] Roland Zimmermann, "Theory of dense excitons in a 2D trap", to appear (2004).

[6.20] M. H. Anderson, J. R. Ensher, M. R. Matthews, C. E. Weimann and E. A. Cornell, Observation of Bose-Einstein condensation in a dilute atomic vapor, Science 269, 198-201 (1995).

[6.21] Negoita, V., Snoke, D. W., and Eberl, K. Harmonic potential traps for indirect excitons in coupled quantum wells. Phys. Rev. B 60, 2661-2669 (1999).

[6.22] V. Negoita, D. W. Snoke and K. Eberl, Stretching quantum wells: a method for trapping free carriers in GaAs heterostructures. Applied Phys. Lett. 75, 2059-2061 (1999).